UNIVERSIDADE DE LISBOA
FACULDADE DE CIÊNCIAS
DEPARTAMENTO DE QUÍMICA E BIOQUÍMICA

Probing the Stability of Biological Molecules in Deep Eutectic Solvents

Inês Filipe Gomes

Mestrado em Bioquímica e Biomedicina

Dissertação orientada por:
Doutor Nuno Galamba (FCUL)
Doutor Alexandre Paiva (FCT-NOVA)

2023

to Farrusca, Bunny & Lara

ACKNOWLEDGEMENTS

I am immensely grateful to my advisors, colleagues, friends & family for their support, patience, and encouragement.

Thank you.

ABSTRACT

Deep eutectic solvents (DESs) have gained prominence as promising alternative solvent media in biocatalysis and biomolecular (cryo)preservation for fragile biomolecules, such as DNA, RNA, cells (including stem cells), and even organs intended for transplantation. The stabilization of proteins by osmolytes, common components of natural DESs (NADESs) is often attributed to a preferential-exclusion/preferential-hydration mechanism, wherein osmolytes are excluded from the protein's surface. However, our understanding of the intricate relationship between biomolecular protection mechanisms in NADES and the role of water remains incomplete.

We enhanced the accuracy of the General Amber Force Field (GAFF) for predicting properties such as density and viscosity for a betaine-glycerol DES, resulting in significant improvements with a minor 0.58% overestimation of density and a 7% underestimation of viscosity compared to experimental data.

We delved into the structural behavior of ubiquitin, a small protein, within aqueous and Betaine-Glycerol-Water (Bet:Gly:Wat) (1:2:ζ; ζ = 0, 1, 2, 5, 10) DESs, exploring a temperature range from 298 K to 450 K. Our results reveal that (Bet:Gly) traps water molecules stopping them from forming a hydration layer around ubiquitin. This unique mechanism enhances protein stability in the DES compared to conventional theories used to explain osmolyte-mediated stabilization. Protein dynamics are closely tied (slaved) to solvent fluctuations. (Bet:Gly) slows down protein dynamics compared to water, preserving protein structures. These findings highlight the importance of protein-solvent interactions and offer insights into non-monotonic protein folding in DESs with varying water levels, showing that protein unfolding in DESs only occurs at high temperatures.

Finally, we explored how different DESs affect mammalian cells. Betaine-Glycerol-Sucrose-Water (2:3:1:5) shows unique cell volume behavior similar to glycerol and sucrose, hinting at a hybrid cryoprotective mechanism. Another DES, Trehalose-Glycerol (1:30) behaves like DMSO in terms of cell volume recovery but has a late-stage decrease.

Keywords: Deep Eutectic Solvents; Molecular Dynamics; Solvation; Ubiquitin; Cryopreservation

RESUMO

Os solventes eutéticos profundos (DESs) ganharam destaque como possíveis solventes alternativos em múltiplas aplicações incluindo aplicações biológicas como a biocatálise e a (crio)preservação de biomoléculas frágeis, como proteínas, DNA, RNA, células, incluindo células-estaminais, e até mesmo de órgãos vivos, destinados a serem transplantados. DESs são misturas, normalmente binárias ou ternárias, que numa razão molecular específica formam misturas eutéticas caracterizadas por uma depressão profunda do ponto de fusão em relação aos seus componentes puros. Estes solventes compartilham diversas propriedades com os líquidos iónicos à temperatura ambiente, incluindo pressões de vapor baixas, não inflamabilidade e estabilidade térmica. No entanto alguns DESs oferecem benefícios adicionais, como biodegradabilidade, baixo custo, facilidade de produção e baixa toxicidade.

Uma preocupação fundamental no uso de DESs para preservação biomolecular é a quantidade necessária de água para proteger eficazmente as estruturas e funções biomoleculares. Organismos vivos desenvolveram mecanismos de proteção para combater a desidratação, o congelamento e a hipóxia, que incluem a síntese de osmólitos protetores como trealose, N-óxido de trimetilamina, betaína ou glicerol. Curiosamente, alguns osmólitos, como a ureia, podem desnaturar proteínas. Contudo, nos DES, o efeito desestabilizador da ureia pode ser mitigado. Dado que muitos componentes dos DES naturais, conhecidos como NADESs, são osmólitos, especula-se que os NADESs possam representar uma "terceira fase líquida" dentro dos organismos, potencialmente facilitando processos biossintéticos específicos. A estabilização de proteínas por osmólitos em condições de desidratação é frequentemente atribuída a um mecanismo de exclusão preferencial/hidratação preferencial, em que os osmólitos são excluídos da superfície da proteína, (des)favorecendo o estado (un)*folded* do equilíbrio *folding-unfolding* da proteína. O estado *unfolded* é desfavorecido devido a um aumento da área superficial acessível das proteínas ao solvente (água) após hidratação preferencial.

No entanto, a compreensão da relação entre os mecanismos de proteção biomolecular nos NADESs, os mecanismos de proteção baseados em osmólitos, os efeitos de aglomeração intracelular (*crowding effects*) e o papel da água permanece incompleta. Nesta tese, integramos abordagens computacionais e experimentais para estudar a estabilidade biomolecular em DESs. Na primeira parte, a tese explora os mecanismos subjacentes à estabilidade proteica num DES através do recurso a simulações de dinâmica molecular. Para proceder a essas simulações, um campo de forças para o NADES Betaína:Glycerol (Bet:Gly) (1:2) foi otimizado. A estabilidade estrutural e térmica da ubiquitina em (Bet:Gly:Wat) é depois estudada em função da quantidade de água no DES. Na segunda parte o trabalho foca-se na análise do potencial dos DESs como agentes crioprotetores para células HaCaT. Estudos experimentais de *swelling* são conduzidos para avaliar a eficácia da criopreservação baseada em DES em comparação com crioprotetores convencionais como DMSO e glicerol.

O primeiro objetivo deste trabalho foi assim o de desenvolver um campo de forças (general AMBER force field (GAFF) que descrevese com exactidão propriedades como densidade e a viscosidade do DES (Bet:Gly). Os resultados aqui apresentados revelaram a inadequação dos parâmetros padrão do GAFF na reprodução dos valores experimentais de densidade e viscosidade. A abordagem convencional de manipulação de cargas atómicas através de fatores de escalamento provou ser insuficiente, pois um único fator de escalamento não conseguiu reproduzir simultaneamente os valores de densidade e viscosidade. O nosso estudo mostrou que a redução das cargas atómicas resultou principalmente numa diminuição substancial na viscosidade, enquanto que o efeito na densidade foi relativamente modesto. Para superar essas limitações, introduzimos um segundo fator de escalamento no parâmetro σ do potencial de Lennard-Jones (diâmetro de van der Waals). Através de ajustes iterativos desses fatores de escalamento, foi possível otimizar o campo de forças. Este envolveu uma

redução de 8% nas cargas atômicas e um aumento de 3% no sigma atômico. É importante ressaltar que o GAFF otimizado demonstrou melhorias significativas, sobrestimando a densidade apenas em 0,58% e subestimando a viscosidade em aproximadamente 7%.

Estudou-se depois a estrutura e dinâmica da ubiquitina, uma pequena proteína, em água e num DES de Betaína:Glicerol:Água (Bet:Gly:Wat) (1:2:ζ; ζ = 0, 1, 2, 5, 10). Uma gama de temperaturas de 298 K a 450 K foram também exploradas para proteína no DES anidro. Os resultados contrastam com o modelo de exclusão preferencial/hidratação preferencial usado para explicar a estabilidade proteica na presença de osmólitos como a betaína e o glicerol. Em vez disso, os resultados revelaram que o DES aqui estudado parece reter moléculas de água na sua estrutura, impedindo assim a formação de uma camada de hidratação em torno da proteína. Este mecanismo contribui significativamente para a estabilidade da ubiquitina em soluções aquosas de (Bet:Gly:Wat). Mesmo em frações molares com alto teor de água, a betaína e o glicerol persistem na interface da proteína, em oposição à hipótese de hidratação preferencial. Os resultados obtidos podem ser explicados através de um modelo de *solvent slaving*, onde os movimentos dinâmicos da proteína estão intrinsecamente ligados com a viscosidade e as flutuações locais das moléculas do solvente. Assumindo que para sofrer mudanças conformacionais significativas, a ubiquitina deve navegar através de uma sequência de movimentos torcionais influenciados pela configuração instantânea das moléculas do solvente, a ausência de uma camada de hidratação parece limitar significativamente esses movimentos. Os resultados revelam assim um impacto significativo na dinâmica de torção da proteína, representando etapas cinéticas elementares subjacentes ao *folding*/*unfolding* de proteínas. O DES induz uma dinâmica conformacional excecionalmente lenta em comparação com a água, preservando a estrutura secundária da proteína. Os resultados aqui apresentados sublinham a importância das flutuações relacionadas com o sistema proteína-solvente (flutuações β). Estes resultados oferecem uma perspetiva mais fundamental sobre estudos recentes de *folding* não-monotónico de proteínas em DESs com proporções molares de água variadas. Os resultados revelam ainda que a desnaturação (*unfolding*) da ubiquitina ocorre a temperaturas muito mais elevadas doe que em água.

Nos estudos de swelling procurou-se determinar as respostas do volume de células de mamíferos na presença de vários DESs. Os resultados mostraram que um DES composto por Betaína:Glicerol:Sucrose:Água (Bet:Gly:Suc:Wat) (2:3:1:5) exibe uma resposta de volume celular contrastante em comparação com a betaína sozinha, sugerindo mecanismos únicos que necessitam de exploração adicional. Notavelmente, (Bet:Gly:Suc:Wat) exibe semelhanças tanto com o glicerol (um crioprotetor permeante) como com a sacarose (um crioprotetor não-permeável), sugerindo um potencial mecanismo crioprotetor híbrido abrangendo elementos permeáveis e não-permeáveis. A dinâmica de recuperação do volume celular em (Bet:Gly:Suc:Wat) assemelha-se muito à observada com o crioprotetor DMSO, relativamente à recuperação celular inicial e perda de volume. Este estudo mostrou ainda que a Trealose-Glicerol, (Tre:Gly) (1:30) exibe uma dinâmica de recuperação de volume celular semelhante ao DMSO, embora se observe uma subsequente diminuição do volume celular aos 40 minutos, um fenómeno não observado com o DMSO. Este estudo compara ainda os (Bet:Gly:Suc:Wat), (Tre:Gly) e Trehalose-Glucose-Sorbitol-Água, (Tre:Glu:Sorb:Wat) (1:1:1:30), com as suas respetivas misturas físicas (PM_BGSW, PM_TG e PM_TGSW, respectivamente), revelando características e comportamentos distintos. A mistura (Bet:Gly:Suc:Wat) demonstra a capacidade de mitigar a redução do volume celular, facilitar a recuperação e ultrapassar o volume celular inicial. Da mesma forma, a (Tre:Gly) provoca um rápido encolhimento celular, com a sua mistura física (PM_TG) a exibir um choque inicial semelhante, mas uma recuperação mais lenta. Em contraste, a (Tre:Glu:Sor:Wat) não consegue iniciar a recuperação celular, possivelmente devido a ligações de hidrogénio mais fortes que dificultam a penetração celular. A sua mistura física, (PM_TGSW), supera a mistura (Tre:Glu:Sor:Wat), destacando o melhor desempenho de DESs ricos em componentes permeantes em relação a DES constituídos por componentes não permeantes. Embora este estudo forneça evidências de viabilidade

celular devido à penetração do DES, os seus efeitos a longo prazo e toxicidade nas células HaCaT requerem investigação adicional.

Para complementar a componente experimental, futuras simulações de dinâmica molecular devem concentrar-se em decifrar as interações DES-membrana que influenciam os efeitos do volume celular. Esta sinergia entre abordagens computacionais e experimentais deverá ajudar a compreender melhor o potencial dos DESs como crioprotetores e abrir caminho para outras aplicações práticas em várias áreas científicas.

Palavras-chave:
Solventes Eutéticos Profundos; Dinâmica Molecular; Solvatação; Ubiquitina; Criopreservação

TABLE OF CONTENTS

LIST OF FIGURES AND TABLES

LIST OF ABBREVIATIONS

A. salina – *Artemia salina*
Bet – Betaine
BSA – Bovine Serum Albumin
CALB – Candida antarctica lipase B
ChCl – Choline Chloride
CN – Coordination Number
DSSP – Dictionary of Protein Secondary Structure
DES(s) – Deep Eutectic Solvent(s)
DMEM – Dulbecco's Modified Eagle Medium
DMSO – Dimethyl Sulfoxide
EPSR – Empirical Potential Structure Refinement
ER – Endoplasmic Reticulum
FTIR – Fourier Transform Infrared Spectroscopy
GAFF – General Amber Force Field
Glu – Glucose
Gly – Glycerol
HBA(s) – Hydrogen Bond Acceptor(s)
HBD(s) – Hydrogen Bond Donor(s)
HRP – Horseradish Peroxidase
HF – Hartree-Fock
LJ – Lennard-Jones
MA – Malonic Acid
MD – Molecular Dynamics
MIC – Minimum-image convention
MM – Molecular Mechanics
mRNA – Messenger RNA
NADES(s) – Natural Deep Eutectic Solvent(s)
ND – Neutron Diffraction
NMR – Nuclear Magnetic Resonance
NPT – Isothermal-isobaric ensemble
NVT – Canonical ensemble
PBC – Periodic Boundary Conditions
PBS – Phosphate-Buffered Saline
PDB – Protein Data Bank
PES – Potential energy surface
PM_BGSW – Physical Mixture of Betaine-Glycerol-Sucrose-Water
PM_TG – Physical Mixture of Trehalose-Glycerol
PM_TGSW – Physical Mixture of Trehalose-Glucose-Sorbitol-Water
PME – Particle Mesh Ewald
Pro – Proline
RDF – Radial Distribution Function
Rg – Radius of Gyration
RESP – Restrained ElectroStatic Potential
RMSD – Root Mean Square Deviation

RNase A – Ribonuclease A
RTIL(s) – Room Temperature Ionic Liquid(s)
TIPnP – Transferable intermolecular potential with "n" interaction points
Sor – Sorbitol
Suc – Sucrose
Tre – Trehalose
U – Urea
vdW – Van der Waals
Wat – Water
Xyl – Xylitol

LIST OF SYMBOLS

D – Self Diffusion Coefficient
F – Force
mol % – Molar percentage
N – Number of particles
$\mathbf{N_A}$ – Avogadro's number
$\boldsymbol{q_i}$ **&** $\boldsymbol{q_j}$ – Partial charges of interacting atoms i and j
$\boldsymbol{r_i}$ – Position vector of the ith atom
$\boldsymbol{r_{ij}}$ – Distance between atom i and atom j
$\mathbf{T_m}$ – Melting Point
U(r) – Total potential energy of the system
$\mathbf{u}(\mathbf{r_{ij}})$ – Two-body potential function
ΔU(r) – Change in potential energy
v/v – Volume per volume
W – Work
wt % – Weight percentage

ζ – Fraction of Water
η – Shear Viscosity
λ_Q – Charge scaling factor
λ_σ – Van der Waals radius scaling factor
ρ – Density
ϕ – Phi
ψ – Psi

CHAPTER 1

Deep Eutectic Solvents – A Comprehensive Prelude

Deep Eutectic Solvents (DESs) represent a promising new class of green solvents with unique properties and a wide range of applications[1]. They have attracted much attention recently due to their unique properties not found in their individual components, such as low melting points, negligible vapor pressures, nonflammability, or good thermal stability. Furthermore, due to a cheap production, resulting from an easy and inexpensive preparation protocol and low cost of components, biodegradability, and low toxicity, many DESs can offset the drawbacks of some room temperature ionic liquids (RTILs) and traditional organic solvents, known for their negative environmental impact, high toxicity, or complex synthesis[2–4]. DESs can be prepared by heating and stirring, and their molecular structure can be analyzed using techniques such as neutron diffraction (ND), nuclear magnetic resonance (NMR), or Fourier transform infrared spectroscopy (FTIR). ND has been used to study the structure of DESs[5,6], NMR has been used to assess both the structure and diffusion of the solvents' components[7], while FTIR has been commonly used to study their chemical properties[8]. Most DESs reported in the literature are completely miscible with water. Thus, usually, viscosity, as well as other properties, can be customized by adding fractions of water to meet a desired property for a particular application[9].

The concept of DESs was first introduced in 2003 by Abbott *et al*. in their paper "Novel solvent properties of choline chloride/urea mixtures"[10]. In this paper, the term "Deep Eutectic Solvents" was introduced for the first time to describe the formation of a complex solvent by combining two simple compounds: choline chloride (ChCl) and urea (U), solids at room temperature, and the resulting mixture was liquid at room temperature (285 K) and its melting point was much lower than the melting point of its constituents. Relative to urea (T_m = 406 K), the melting point of (ChCl:U) (T_m = 285 K), in the ratio (1:2) is approximately 1.4 times lower, and compared to ChCl (T_m = 575 K), it is approximately 2 times lower – hence the deep in "deep eutectic solvents" (see **Fig. 1.1**)[10]. This discovery marked an important milestone in the development of organic solvents sparking a wave of research on the properties of DESs as well as their potential applications in various industries. To this day DESs continue to generate significant interest which is made evident by a surge in the number of publications that continues to increase almost exponentially[11]. Nowadays DESs are established as one of the most promising classes of green solvents (especially type III DESs which are free from metals[9]) with an indisputable potential to replace traditional solvents whose use has a negative impact on the environment.

The sharp depression of the melting temperature is believed to be caused by the establishment of a network of hydrogen bonds between the hydrogen bond acceptors (HBAs) and hydrogen bond donors (HBDs) that form each DES, resulting in a weakening of the intermolecular interactions between the pure compounds[2,12,13]. Amides, amines, amino acids, sugars, alcohols, and carboxylic acids are some of the substances that belong to the group of HBDs. Quaternary ammonium compounds make up some of the HBAs used in DESs. DESs obtained from natural sources are called natural deep eutectic solvents (NADESs)[4]. Some HBAs and HBDs can be found in **Fig. 1.2**.

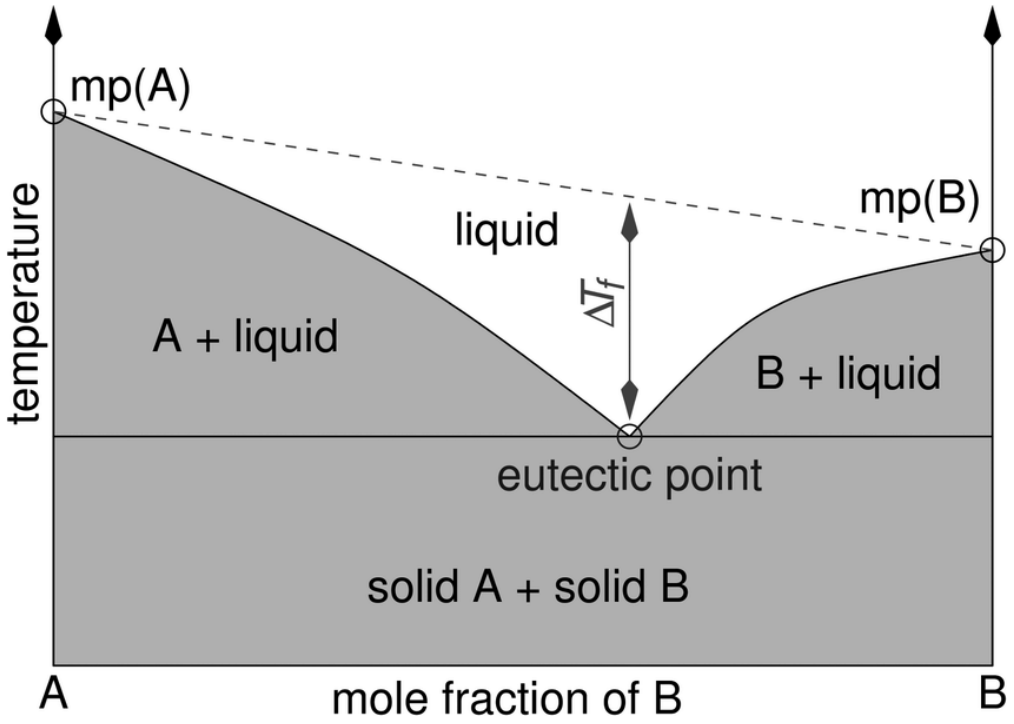

Figure 1.1. Schematic representation of an eutectic point on a two-component phase diagram (from Smith *et al.*[13]). *Unlike the idealized eutectic system, DESs involve complex interactions that lead to a greater depression of the melting point lower than what the simple eutectic system predicts. This heightened intermolecular bonding leads to a reduction in the overall energy required to transition from a solid to a liquid state, thereby resulting in a lower melting (mp) or freezing point (ΔTf).*

Despite being known for their low toxicity and biocompatibility, experimental findings showed that ChCl-based DESs exhibited higher cytotoxicity compared to their individual components[14]. In particular, the cytotoxicity tests using *Artemia salina* leaches indicate that they are susceptible to DES toxicity, while being resistant to the toxicity of individual DES components in aqueous solutions. The authors suggested that the hydrogen bonding between the HBD and the salt's anionic component, responsible for the DES formation, exerts more than just physical influence on the individual components. It appears to also induce alterations in the chemical structure of the mixture. Several factors could contribute to the cytotoxicity of *A. salina*, such as oxygen depletion or restricted movement due to the high viscosity of the DES. The chemical composition of the DES components directly influences its viscosity, with factors such as the type of salt and HBD, molar ratio, water content, and temperature playing roles. However, further comprehensive investigations are necessary to better comprehend the intricate relationship between the DESs compositions and their physicochemical properties. Toxicity assay studies conducted on 550+ DESs further confirmed that DESs have a toxic behavior that cannot be ignored and their green credentials may not be entirely accurate[4]. According to the latter study, organic and inorganic acids are generally associated with relatively higher toxicity compared to other HBD components. With the exception of lactic acid, most other acids (oxalic acid, phenylacetic acid, zinc chloride, benzoic acid, citric acid, tartaric acid, malic acid, malonic acid, p-toluenesulfonic acid, glycolic acid, levulinic acid, and acetic acid) are anticipated to have toxic contributions. In contrast, many alcohols, such as xylitol, sorbitol, 1,2-propanediol, and ethylene glycol, are expected to possess relatively non-toxic attributes. Among other HBD components, acetamide, ethylene glycol, urea, diethylene glycol, lactic acid, glycine, and 1,4-butanediol demonstrate a lesser tendency to induce toxicity. Additionally, natural sugars like sucrose, glucose, maltose, and fructose are ranked as less toxic. The mechanisms underlying DESs' toxicity, nevertheless, lack a definitive consensus. One hypothesis proposes that DES-associated toxicity may arise from charge delocalization phenomena stemming from hydrogen bonding interactions between anionic species and HBDs. These charge

delocalization events might be a key factor in how DESs interact with cellular components and potentially induce toxic responses.

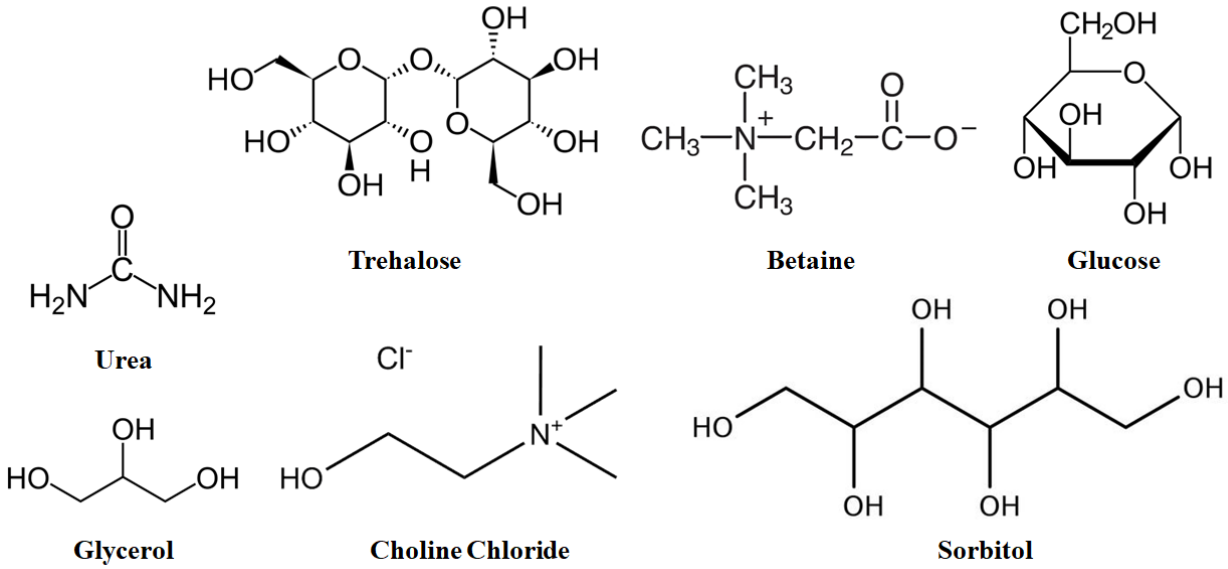

Figure 1.2. Molecular structures of some DESs components. *This figure illustrates the molecular structures of the components comprising the DESs employed in this thesis.*

Hayyan and coworkers[14], interestingly, suggested that DESs could act selectively, potentially demonstrating destructive effects on certain cell types (*e.g.*, tumor cells) while remaining non-destructive to others. Considering the adverse effects of conventional treatments like chemotherapy and radiotherapy, a thought-provoking question was raised: could DESs step forward as promising candidates for alternative therapeutic approaches? Might they be harnessed either as substitute drugs, carriers for therapeutic agents, or even perform a dual role encompassing both functions? By posing this question, the focus shifts towards the potential of DESs to revolutionize medical treatments. Considering the limitations and side effects associated with existing therapies, the exploration of DESs as a versatile and innovative solution opens doors to novel avenues for therapeutic interventions. Should DESs prove successful in fulfilling these roles, the implications would be far-reaching: it would signify a significant departure from traditional approaches, potentially minimizing the negative impacts suffered by patients during treatments. This paradigm shift could alleviate the burden of severe side effects and offer patients a more tolerable healthcare experience.

While there has been significant progress in recent years, there are still many open questions concerning their properties and their real potential in a number of applications. In this thesis, we integrated computational and experimental approaches to study biomolecular stability in DESs. At the outset, we assessed the underlying mechanisms governing protein stability in the presence of a NADESs, betaine-glycerol (Bet:Gly) (1:2), delving into both thermodynamic and kinetic facets using molecular dynamics (MD) simulations.

To conduct MD simulations of (Bet:Gly) (1:2) we developed a General Amber Force Field (GAFF)-based force field for the DES. We highlight the limitations of using unchanged restrained electrostatic potential (RESP) atomic charges as well as scaled atomic charges alone, to accurately describe the structure and dynamics of the solvent. We present an optimized force field that demonstrated improved predictive accuracy, with a slight overestimation of the experimental density and underestimation of the viscosity. The methodology proposed in this study (**Chapter 3**) presents a simple and intuitive approach that can be applied to refine GAFF for other DESs as well. **Chapter 4**

discusses the stability of a prototypical small protein (ubiquitin) in a (Bet:Gly) DES, including the role of water, through MD, using the latter force field.

Subsequently, we shifted our focus towards a practical application in the realm of cryopreservation (**Chapter 5**). Through experimental swelling studies, we evaluated the efficacy of DESs as cryoprotective agents using HaCaT cells. We juxtaposed the outcomes of DES-based cryopreservation with the outcomes observed using the two most prevalent cryoprotective agents, namely DMSO and glycerol. Through this integrated approach, we not only expanded the theoretical foundation of biomolecular stability in the presence of DESs but also translated these findings into cellular cryopreservation.

CHAPTER 2

The Molecular Dynamics Method

Computational chemistry is an interdisciplinary field that involves the use of chemistry, physics, computer programming, and mathematical models to study and predict chemical and biochemical phenomena. The field emerged during the 1960's along with the development of modern computers and is based upon the application of quantum mechanics and classical and statistical mechanics to the study of chemical (and biological) systems. The field encompasses electronic structure calculations (quantum chemistry) which entails solving, through some approximate method, the Schrödinger equation, and molecular mechanics and molecular simulation methods (*e.g.*, molecular dynamics, Monte Carlo) which use classical mechanics and can be applied to larger systems at the expense of the loss of a quantum description.

Molecular mechanics (MM) involves the use of fundamental principles of classical mechanics or Newtonian mechanics to model molecular systems. The behavior of a molecule is described by the potential energy surface (PES) of the system which is modelled by a function that describes the interactions between the atoms in terms of the potential energy associated with each atom's position. In MM the potential energy of the system is described by a set of mathematical equations known as intermolecular potential or force field.

The method of molecular dynamics (MD) consists in solving a set of equations of motion for a system of N particles, given some initial positions and velocities, and some prescription to calculate the interactions between the particles. The trajectory of the system in combination with statistical mechanics principles and relationships provide a way of calculating the same properties that can be measured in the laboratory while assessing molecular information not directly available through experiments. Whereas interactions between particles can be calculated through quantum chemistry methods, this method, called *ab initio* MD, is still limited to relatively small systems, and will not be discussed herein. Thus, instead, molecular simulations in this study were performed through classical MD where the calculation of molecular interactions relies on empirical force fields.

The MD method is comprised of three stages: initialization, equilibration, and production. Initialization encompasses the definition of the initial positions and velocities of the model system, the force field, as well as other parameters (*e.g.*, time-step, number of simulation steps) and variables such as the temperature, pressure, or density. The energy of the system is also commonly minimized during this stage. This is followed by equilibration where a trajectory is generated aiming at driving the system into some thermodynamic state of equilibrium of interest (*e.g.*, a specific temperature and pressure). The last stage is the production stage where the trajectory is propagated starting from a set of equilibrated positions and linear momenta. This trajectory is then analyzed to assess the properties of interest, including structural, thermodynamic and/or dynamic properties.

All MD simulations reported in this thesis were performed with the GROMACS software package[15].

2.1 HISTORICAL BACKGROUND

Despite the limited computational resources, the 1950s marked a pivotal era in the development of MD simulations. In 1955, Enrico Fermi, John Pasta, Stanislaw Ulam and Mary Tsingou published their work "Studies of Nonlinear Problems"[16] which describes the use of the MANIAC I computer at Los Alamos National Laboratory to study the time evolution of many-body systems (64 interacting particles). The particles in the system were connected by forces that exhibited nonlinearity, characterized by quadratic, cubic, and broken linear terms. Contrary to expectations, the system did not reach a state of thermal equilibrium where energy is evenly distributed among its components (ergodicity); instead, it showed a cyclic repetition of energy patterns over time. This unexpected phenomenon became known as the Fermi–Pasta–Ulam–Tsingou problem. In 1959, "Studies in

Molecular Dynamics. I. General Method"[17] was published by Alder and Wainwright. One specific aspect highlighted in the paper is the utilization of an IBM 704 computer to simulate elastic collisions between hard spheres meaning that the particles were represented as solid, impenetrable spheres that undergo collisions without any loss of kinetic energy. Alder and Wainwright were able to numerically solve the equations of motion for the system of hard spheres, calculating the trajectories and velocities of the particles as they interacted and collided with each other. In 1964[18], Rahman conducted simulations of liquid argon using the Lennard-Jones potential. Rahman's simulations of liquid argon were particularly significant because Rahman was able to calculate various properties (*e.g.*, the velocity autocorrelation function and the self-diffusion coefficient which was only 15% lower than the experimental value) of the system in good agreement with experimental data which validated the use of MD simulations as a reliable tool for studying and predicting the behavior of complex molecular systems. Additionally, his use of the Lennard-Jones potential proved to be successful in providing meaningful insights into the behavior of liquid argon and establishing a foundation for more sophisticated force field models in the future. In "Computer "Experiments" on Classical Fluids. I. Thermodynamical Properties of Lennard-Jones Molecules"[19], Verlet conducted simulations to study the thermodynamic properties of 864 particles assumed to interact with each other through the Lennard-Jones potential by integrating the equations of motion using what is now known as the Verlet algorithm. The Verlet algorithm enabled the numerical integration of equations of motion for many-particle systems.The first simulation of liquid water[20] was published in 1971 by Stillinger and Rahman and only six years later the first molecular simulation of a folded globular protein (bovine pancreatic trypsin inhibitor) was reported[21].

Over the years, MD simulations have become a powerful, viable and routine method to study biomolecules[22], both qualitatively and quantitatively. Combined with experimental data, valuable insight into molecular mechanisms involved in chemical and biological processes have been obtained, which could not be assessed through experimental methods alone.

2.2 PAIRWISE ADDITIVE POTENTIALS: THE LENNARD-JONES MODEL

The total potential energy of the system is commonly calculated as a sum of pairwise contributions between pairs of particles. The pairwise additive potential assumes that the overall interaction energy of the system can be approximated by considering only the interactions between pairs of particles, neglecting higher-order interactions involving three or more particles simultaneously. This simplification of complex interactions among multiple particles, by considering them as a sum of two-body contributions, significantly reduces computational complexity. For a system containing *N* atoms, the pairwise additive potential states that the total interaction energy among the *N* atoms can be obtained by summing up the interaction energies between all possible pairs of atoms. The pairwise additive potential function, $U(r)$, is then the interaction energy for a given configuration of atoms that depends on the positions of the atoms, which are represented by the set of position vectors $r^N = (r_1, r_2, r_3, \dots, r_N)$, where r_i represents the position vector of the ith atom. The interaction energy between two atoms is described by a two-body potential function denoted $u(r_{ij})$, where r_{ij} is the distance between atom i and atom j in the system ($r_{ij} = |r_i - r_j|$). The potential energy function $U(r_{ij})$ is obtained by summing up all the pairwise contributions $u(r_{ij})$ between all pairs of particles (i, j) with $i < j$. Thus, $U(r) = \sum_{i<j} \sum u(r_{ij})$.

In 1924, John Lennard-Jones introduced a model still widely used to this date, known as the Lennard-Jones potential[23], for the pair potential energy between two interacting particles in a system that provides a simple, yet effective description, of the attractive and repulsive forces between particles (**fig. 2.1**). The Lennard-Jones potential is given by the equation:

$$u(r_{ij}) = k\epsilon\left[\left(\frac{\sigma}{r_{ij}}\right)^{n} - \left(\frac{\sigma}{r_{ij}}\right)^{m}\right] \quad \textbf{(2.1)}$$

where $u(r_{ij})$ represents the pair potential energy between particles *i* and *j*, as a function of their separation distance, r_{ij}. k and ε are constants that control the strength and depth and of the potential energy well. ε is the depth of the potential well, while k scales the strength of the attractive and repulsive forces. σ represents the distance at which the interparticle potential energy is zero. *n* and *m* are positive integers, with $n > m$. The first term in the Lennard-Jones potential, $(\sigma/r_{ij})^{n}$, represents the repulsive forces between the particles *i* and *j* at a distance r_{ij}. As the particles get closer (r_{ij} decreases), the repulsive force increases rapidly, preventing the particles from overlapping and maintaining a minimum separation distance. Larger values of *n* lead to a steeper curve. This short-range repulsion effectively prevents unrealistic overlaps and is also known as Pauli's repulsion, deriving from Pauli's exclusion principle of quantum mechanics which states that no two electrons can occupy the same spin orbital.

The second term in the Lennard-Jones potential, $(\sigma/r_{ij})^{m}$, describes the attractive forces between the particles. When the particles are not too close to each other, the attractive forces dominate. These forces are known as London dispersion forces (or van der Waals forces) and are responsible for the attraction between molecules, even in non-polar substances. The longer-range attraction helps deter the disintegration of the substance.

Thus, a higher value of m will make the attractive forces stronger while a higher value of n will make the repulsive forces stronger[24].

The concept of London dispersion forces was first proposed by Fritz London in 1930. London dispersion forces are temporary attractive forces that arise when the electrons of atoms in polar and nonpolar molecules experience momentary fluctuations in their charge distribution, leading to the formation of temporary (aka instantaneous) dipole moments. These temporary dipoles induce dipole moments in nearby molecules, resulting in an attractive interaction between them. The energy of the London dispersion forces decreases rapidly with increasing distance between molecules, following an inverse sixth-power relationship $1/r^6$ meaning that the attractive energy falls off relatively quickly (as opposed to electrostatic interactions) as the separation distance increases. By setting $m = 6$ in the Lennard-Jones potential, the attractive forces are modeled with a $1/r^6$ term. This specific choice of m makes the Lennard-Jones potential consistent with London's theory of dispersion forces and ensures that the potential accurately captures attractive interactions between particles. On the other hand, $n = 2m = 12$, although commonly used, does not have a specific physical justification related to the underlying (quantum) molecular interactions (*i.e.*, Pauli repulsion forces).

In the general Lennard-Jones formula, k equals $k = (n/n-m)(n/m)^{m/n-m}$. For $m = 6$ and $n = 12$, we have that: $k = (2)(2)^1 = 4$. Therefore, the Lennard-Jones (12-6) potential is given by,

$$u(r_{ij}) = 4\epsilon\left[\left(\frac{\sigma}{r_{ij}}\right)^{12} - \left(\frac{\sigma}{r_{ij}}\right)^{6}\right] \quad \textbf{(2.2)}$$

As mentioned earlier, σ represents the distance at which the potential energy is zero, while ϵ represents the energy at the minimum of the potential energy well (**fig. 2.1**).

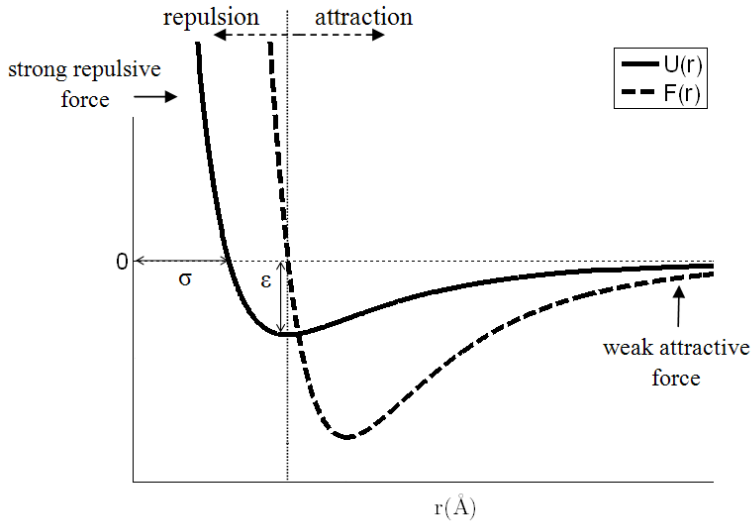

Figure 2.1. Lennard-Jones potential energy, U(r), and the corresponding interatomic force, F(r), plotted against the distance, r. *The Lennard-Jones potential energy curve (black curve) showcases the characteristic attractive van der Waals region followed by the repulsive region. The interatomic force curve (dashed line) depicts the force exerted between the atoms as they approach or separate (adapted from Damasceno et al. [25]).*

When a force causes a displacement in the direction of the force, work is done on the object. Thus work (W) is defined as the energy transferred to or from an object due to the action of a force resulting on a displacement of the object. The work done by a force can change the object's potential energy, $\Delta U(r)$. This relationship is given by the equation: $\Delta U(r) = W = \int F\, dr$. Conservative forces are those for which the work done by the force on a particle moving between two points depends only on the initial and final positions, not the path taken. To find the pairwise additive force $F(r_{ij})$ acting between two particles, we take the negative of the derivative of the potential energy $U(r_{ij})$ with respect to r_{ij}: $F(r_{ij}) = -(dU(r_{ij})/dr)$. The negative sign ensures that the force always points in the direction that reduces the potential energy. Taking the derivative of the Lennard-Jones potential, $u(r_{ij})$, we obtain the force between particles *i* and *j*,

$$F(r_{ij}) - \frac{du(r_{ij})}{dr} = -\frac{24\epsilon}{\sigma}\left[2\left(\frac{\sigma}{r_{ij}}\right)^{13} - \left(\frac{\sigma}{r_{ij}}\right)^{7}\right] \quad \textbf{(2.3)}$$

The Lennard-Jones model alone allows describing simple atomic systems such as rare gases, which only experience short-range repulsions and dispersion forces. For more complex systems other intramolecular and/or intermolecular interactions play a role and must be modeled. This results in the construction of a force field, which is at the heart of molecular mechanics/dynamics.

2.3 FORCE FIELDS

A force field is a set of mathematical equations that describe the potential energy of molecules. These equations take in parameters that govern the strength of the intra and intermolecular interactions often obtained from experimental data, quantum mechanical calculations, or a combination of both. In MD simulations, force fields provide a mathematical description of how atoms interact with each other within a molecule through bonded interactions and with other molecules through nonbonded interactions. There are different types of force fields: (1) All-atom force fields, that offer high chemical detail by comprising parameters for each type of atom in a system, including hydrogen atoms; (2)

United-atom force fields, that treat hydrogen and certain carbon atoms as a single interaction center enhancing computational efficiency while still accounting for most interactions at an atomic level; and (3) Coarse-grained force fields, that represent groups of atoms as single interaction sites and are particularly useful to simulate large macromolecules like membranes, proteins or RNA and DNA, largely sacrificing fine chemical details for computational efficiency.

In this work the widely used all-atom (non-polarizable) AMBER force field, AMBER99SB (the "SB" in AMBER99SB stands for "side chain and backbone corrections") was used to describe ubiquitin. AMBER99SB was built upon the earlier ff94 and ff99 force fields and it aimed to address the limitations of its predecessors[26]. The ff99 force field attempted to correct the limitations in ff94 including an over-stabilization of α-helixes. The previous parameter set did not adequately balance the energy between helical and extended regions in peptide and protein backbones leading to inaccuracies in predicting the relative stability and population of these secondary structure elements. Additionally, previous AMBER force fields neglected the existence of two sets of backbone phi/psi dihedral terms leading to unreasonable conformational preferences for glycine. To improve these aspects, the 99SB force field underwent careful reparametrization of the backbone torsion terms of the ff99 force field, leading to a more balanced representation of four fundamental secondary structure elements (polyproline II helix, β-sheet, α-left-handed, and α-right-handed). The refinement process involved fitting dihedral term parameters by comparing the energies of multiple conformations of glycine and alanine tetrapeptides to high-level ab initio quantum mechanical calculations. Consequently, the ff99SB force field exhibited improved balance among secondary structure elements solving previous issues in the backbone dihedrals for glycine and alanine. These enhancements on torsional parameters for both backbone and side chains were supported by experimental data for short peptides and improved consistency with experimental NMR data for test protein systems, leading to a more accurate representation of protein structures and improved stabilities of helical peptides.

The AMBER-family of protein force fields accounts for covalent bonds through harmonic bond stretching terms derived from experimental data and quantum mechanical calculations and has the following general form:

$$U_{\text{AMBER}} = \sum_{i}^{Bonds} K_b\left(r_i - r_{eq}\right)^2 + \sum_{i}^{Angles} K_\theta\left(\theta_i - \theta_{eq}\right)^2 + \sum_{i}^{Dihedrals}\left[\frac{V_n}{2}\left(1 + cos(n\phi_i - \Upsilon_i)\right)\right] + \sum_{i<j}^{Van\ der\ Waals}\left[4\epsilon_{ij}\left(\left(\frac{\sigma_{ij}}{r_{ij}}\right)^{12} - \left(\frac{\sigma_{ij}}{r_{ij}}\right)^{6}\right)\right] + \sum_{i<j}^{Electrostatics}\frac{q_i q_j}{4\pi\varepsilon r_{ij}} \quad \textbf{(2.4)}$$

The first term describes the stretching of covalent bonds and quantifies the energy associated with the harmonic oscillation of bonded atoms around their equilibrium bond lengths. The second term, $\sum_i^{Angles} K_\theta\left(\theta_i - \theta_{eq}\right)^2$, accounts for the bending of covalent bond angles. $\sum_i^{Dihedrals}[V_n/2(1 + \cos(n\phi_i - \Upsilon_{i,n}))]$ describes the energy associated with dihedral (torsion) angles between bonded atoms, thus capturing the rotational flexibility of covalent bonds. The last two terms account for nonbonded interactions: the Lennard-Jones potential models van der Waals interactions, whereas electrostatic interactions are described by the potential of Coulomb, where q_i and q_j are the partial charges of the interacting atoms, and "ε" is the permittivity of the medium.

2.4 WATER MODELS

Most water models represent water molecules as collections of rigid "bodies" with fixed partial charges that aim to approximate the electronic distribution in the molecule and capture their electrostatic interactions. Despite neglecting certain electronic effects, such as polarization effects, and the finer details of the charge distribution within the molecule, some of these models provide an accurate description of many properties, like the density, viscosity, or the self-diffusion coefficient.

To address the limitations that arise from fixed charges, polarizable water models that account for the effects of molecular polarization, such as AMOEBA[27], have been developed. In these models, the charges can be redistributed as a response to the local electric field. Additionally, flexible water models, such as TIP3P-FB and TIP4P-FB (TIPnP stands for transferable intermolecular potential with n interaction points) that allow the water molecule's geometry to respond to the environment were also developed. Both polarizable and flexible water models provide a more realistic representation of water's behavior. However, their increased complexity comes with an additional computational cost limiting their widespread use, especially for biological systems where a large number of water molecules is involved. Hence, classical rigid water models provide a reasonable compromise between accuracy and computational efficiency. Similarly, polarizable force fields are seldom used to describe biological systems and large systems in general.

In the TIP3P[28] water model, water molecules are represented as three-point charges: two hydrogen atoms and one oxygen atom. The TIP4P[28] model enhances this representation by introducing an additional virtual site commonly labeled "M" which is positioned along the H-O-H bond angle bisector. The reason for introducing this additional site is to achieve a more realistic representation of the charge distribution within water molecules (**fig. 2.2)**. The distance between the M-site and the oxygen atom is fixed at 0.15 Å. In the TIP4P model, the bond length between O-H is fixed at 0.9572 Å and the bond angle formed by the two hydrogen atoms with the oxygen atom is fixed at 104.52°. The oxygen atom carries both a point charge and a Lennard-Jones interaction site and each hydrogen atom is associated with a point charge but does not have Lennard-Jones interactions.

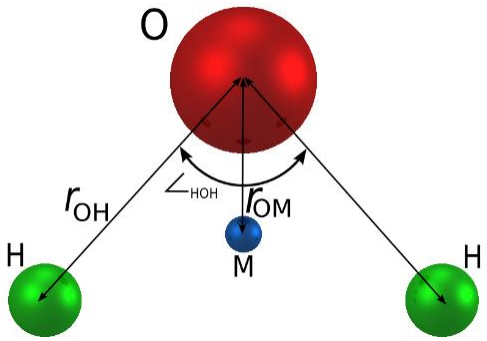

Figure 2.2. TIP4P family water model. *The TIP4P model improves upon the TIP3P model by introducing the additional site M which is positioned at a fixed distance along the bisector of the HOH bond angle, contributing to a more accurate description of water molecules in molecular simulations*
(source: www.sklogwiki.org/SklogWiki/index.php/TIP4P_model_of_water).

The original TIP4P water model, while successful in reproducing certain properties of water, was found to have limitations in accurately representing electrostatic interactions when the Ewald sum (see **section 2.8**) was used to compute electrostatic interactions. Thus, discrepancies were found between the TIP4P water properties when using the Ewald sum and truncated cut-off methods used in the original development of the model. This motivated the development of a reparametrized version of the TIP4P model to be used with Ewald sum-based techniques, denoted TIP4P-Ew[29]. The charges and

bond lengths were adjusted to improve the accuracy of the model when combined with the Ewald summation technique for the treatment of long-range electrostatic interactions. The distance between the oxygen atom and the M-site in the TIP4P-Ew model is smaller (0.1250 Å as opposed to 0.15 Å). The re-parameterization, guided by experimental data, has resulted in a model that better reproduces the structural, thermodynamic, and kinetic properties of bulk water[30].

2.5 INITIAL POSITIONS AND VELOCITIES

Along with the definition of the force field, number of steps, the time-step, ensemble, and other parameters, the definition of initial positions and velocities is performed during initialization. The initial positions can be those of a previous simulation, when available, those of a crystalline phase, or more commonly, atoms and/or molecules are randomly inserted considering the atomic van der Waals radius to avoid atom superposition.

When initial velocities are not available from a previous simulation these can be either randomly generated within some interval or defined according to the Maxwell-Boltzmann distribution at the temperature of interest. The linear momenta of the particles are then scaled to insure a zero total linear momenta[31].

2.6 ENERGY MINIMIZATION

As previously referred, previous to equilibration the system's energy is commonly minimized to prevent steric clashes between atoms which could lead to high repulsions at the beginning of the equilibration stage. Here we used the steepest descent algorithm to minimize the potential energy of the system.

The steepest descent method is an optimization algorithm used to find the minimum of a general nonlinear function. The method is based on the observation that, for a real-valued continuous function f(x), taking steps in the direction opposite to the gradient ∇f(x), should lead to a decrease in the function value. The forces acting on each atom are calculated, and the atoms' positions are adjusted in the direction opposite to the forces (negative gradient direction). The primary goal of the steepest descent algorithm is to find the direction that corresponds to the negative gradient of the function. To find the steepest direction, the algorithm approximates the function $f(x + \Delta x)$ using a first-order Taylor expansion: $f(x + \Delta x) \approx f(x) + f'(x) \cdot \Delta x$. By adjusting the positions of the atoms in the direction opposite to these forces, the system effectively moves towards regions of lower potential energy. This process is repeated iteratively, adjusting the positions of the atoms at each step.

The minimization process continues until the maximum force acting on any atom in the system falls below a specific value. Once the forces are below this threshold, the minimization is considered converged and upon convergence, the system reaches a local energy minimum, and the final minimized coordinates are obtained.

If x(i) is the current point in the search for the minimum and x(i+1) is the updated position after one iteration of the steepest descent algorithm which can be described with the following formula:

$$x_{i+1} = x_i - \alpha \nabla f(x_i) \quad \textbf{(2.5)}$$

where α corresponds to the step size and choosing an appropriate value for α is important considering that a too small or too large value can cause the method to converge slowly or diverge.

2.7 PERIODIC BOUNDARY CONDITIONS AND MINIMUM IMAGE CONVENTION

MD simulations cannot be carried out for system sizes similar to those commonly used in the laboratory, that is, with a number of particles of the order of $N_A(10^{23})$. Thus, in MD, periodic boundary conditions (PBC) are used to eliminate surface effects (unless the latter are the object of study) as particles would experience more interactions with the walls than with other particles, introducing surface effects, absent in a bulk material.

To counter this, a primary cell without physical walls representing the bulk material is defined. This cell is surrounded by identical replicas, known as image cells. The periodicity applies to both the positions and momenta of the image particles in the image cells.

The position of a cell can be described using a vector "α" referred to as the cell translation vector. This vector "α" consists of signed integers or zeros. For example, the primary cell's vector is $\alpha = (0, 0, 0)$. The position of an atom in an image cell is the same as the position of the analogous atom in the primary cell, translated by $\alpha = (\alpha_1, \alpha_2, \alpha_3)$. Atoms and their images can move freely between cells due to open boundaries. When an atom leaves the primary cell, its corresponding image enters the primary cell through an opposite face with the same velocity. This maintains a constant number of atoms in the system (**see fig. 2.3**).

PBC introduce artificial periodicity into the simulation. This periodicity affects some conserved quantities (*e.g.*, angular momentum) and can limit the study of long-range phenomena. The effect of PBC on equilibrium properties like thermodynamic properties and local structure are, however, generally small, and often overshadowed by other sources of error. PBC's impact can be more noticeable on dynamic properties, particularly time correlation functions.

To calculate interactions in a virtually infinite system (*i.e.*, a system with PBCs), the so-called minimum-image convention (MIC) is used. This means each molecule interacts only with its closest neighbors, including image particles. Thus, within MIC, the molecule *j* closest to *i* might not be the original *j*, but a copy from an adjacent cell, *j**. To avoid a particle to see its own images, interactions are calculated only within a maximum distance defined by half the size of the simulation cell. This distance is often further reduced by the introduction of a cut-off distance which accounts for the fact that van der Waals interactions do not extend beyond 10-14 Å, thus, improving computational efficiency. Additional techniques, such as neighbor lists, are also commonly used in MD simulations. These are lists of nearest neighbors, that permit computing pair interactions for small time-windows, in between neighbor list updates, without assessing the nearest neighbors of each atom.

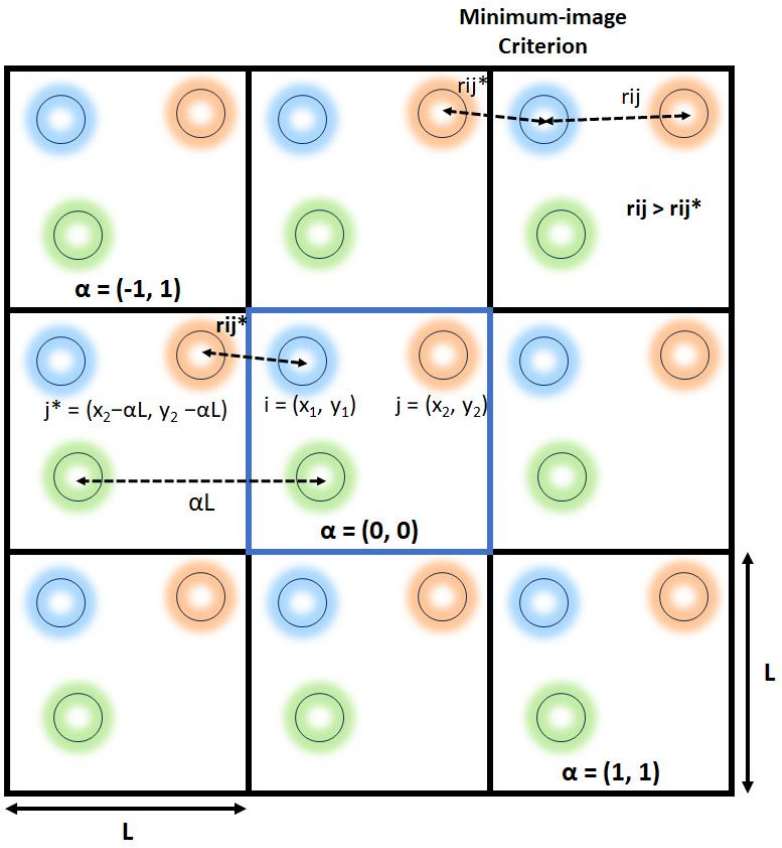

Figure 2.3. Periodic boundary conditions and minimum image criterion. *Periodic boundary conditions involve replicating the simulation cell to eliminate surface effects.*

2.8 EWALD SUMMATION TECHNIQUES FOR LONG-RANGE INTERACTIONS

Electrostatic interactions are long ranged interactions, extending well beyond the size of the primary MD box. Additionally, the Coulombic potential is only conditionally convergent, and simple addition of pairs throughout the periodic system (image cells) will diverge. Thus, Ewald summation-based techniques, such as Particle Mesh Ewald (PME), used herein, are commonly applied to compute long-range electrostatic interactions in systems with periodic boundary conditions. The basic idea is to split the Coulomb interactions into two components: a short-range component that can be computed in real-space and a slow-decaying component that is calculated in the reciprocal space. The method involves neutralizing the atomic charges by the introduction of screening gaussian charge distributions of opposite charge centered on each atomic charge. The sum of these screened charges becomes short-ranged and convergent in the real space. A second sum is then performed, which encompasses similar gaussian charge distributions of opposite sign (compensation Gaussians) which must be subtracted to give the electrostatic potential due to the atomic charges rather than the screened charges. Whereas the latter is divergent in the real space it converges readily in the reciprocal space. A spurious self-interaction term that arises due to the interaction of each point charge with its own screening Gaussian charge distribution must also be subtracted.

In this thesis electrostatic interactions were treated using the particle-mesh Ewald (PME)[32] method, a faster algorithm based on the Ewald sum technique.

2.9 INTEGRATION ALGORITHMS

The time evolution of the system is simulated by repeatedly applying any integration method in order to update the positions and velocities of the particles. Several algorithms have been developed to numerically integrate differential equations, and, in particular, Newton's or Hamilton's equations of motion used in MD. Among these, a particularly efficient algorithm is the Verlet "leap-frog", which is a variation of the original algorithm proposed by Verlet.

In the leap-frog algorithm, velocities and positions are updated at different points in time, leaping over each other (**fig. 2.4**). The equations of the Verlet "leap-grog" algorithm are the following:

$$v(t + \Delta t/2) = v(t - \Delta t/2) + \Delta t \cdot F(t)/m \quad \textbf{(2.6)}$$

$$r(t + \Delta t) = r(t) + \Delta t \cdot v(t + \Delta t/2) \quad \textbf{(2.7)}$$

Having the positions at time-step *t*, the forces are computed, from which the accelerations $(F(t)/m)$ at time-step *t* are obtained. From the accelerations and the known velocities at step (t-Δt/2) the velocities are advanced to the next half-step, (t+Δt/2). Then using the velocities at the half-step (t+Δt/2) the positions at (t+Δt) are estimated. Since the velocities are normally needed at integral time steps, for the calculation of the kinetic energy and/or for instance some transport coefficients, they can be obtained through the following average,

$$v(t) = \frac{v(t+\Delta t/2)+v(t-\Delta t/2)}{2} \quad \textbf{(2.8)}$$

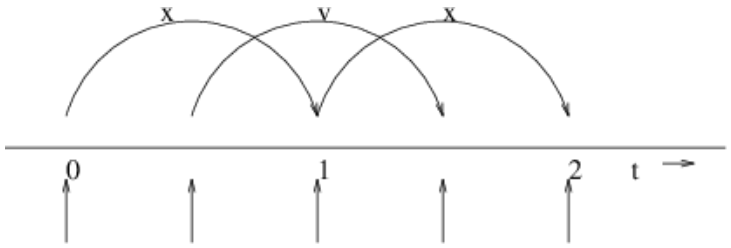

Figure 2.4. Leap-frog integration method. *The Leap-Frog integration method, aptly named after the way frogs leap over each other, is illustrated in this figure. The algorithm involves alternating updates of positions (r) and velocities (v) in discrete steps (from GROMACS User Manual[31]).*

2.10 TEMPERATURE AND PRESSURE CONTROL

The natural thermodynamic state or ensemble of MD is the microcanonical, or isolated system (*N*,*V*,*E*), because usually one defines the number of particles (*N*) and the volume (*V*) of the MD box, and Newton's equations of motion conserve the total energy of the system (*E*). However, experiments are usually performed at either *NVT* (canonical ensemble) or, more commonly, at *NPT* (isothermal-isobaric ensemble) conditions. Thus, one is interested in replicating the latter macroscopic states rather than working in the microcanonical ensemble. This is possible by abandoning Newton's equations of motion and using mathematical thermostats and/or barostats coupled to the equations of motion.

Herein, MD were performed in the *NPT* ensemble although a small (initial) part of the equilibration was always carried out in the canonical ensemble to thermalize the system, before the barostat was turned on.

2.10.1 Thermostats

To achieve temperature control in MD simulations, a thermostat interacts with the system by adjusting the velocities of individual particles in response to deviations from the desired temperature. This adjustment maintains the temperature of the system close to the desired value.

In statistical mechanics, the temperature of a system is related to the average kinetic energy through the principle of equipartition of energy. For a polyatomic system with N particles: $\langle K \rangle = (1/2)N_f k_B T$ where $\langle K \rangle$ represents the average kinetic energy, N_f is the number of degrees of freedom of the system, and k_B is the Boltzmann constant. To keep the temperature of the system constant, the average kinetic energy must remain fixed, while allowing the instantaneous kinetic energy, and, therefore, the temperature, to fluctuate. However, if velocities were rescaled to a specific value at every step, the kinetic energy of the system would not exhibit fluctuations. While more than one thermostat allows overcoming this problem, we shall focus on the velocity rescaling algorithm (V-rescale), or the Bussi thermostat[33].

The Bussi thermostat builds upon the Berendsen thermostat[34] to address the abovementioned limitations also present in the latter. The Berendsen thermostat simulates a system's interaction with an external heat bath, which provides or absorbs thermal energy to or from the system based on temperature differences. An external heat bath is a conceptual construct that represents an infinite reservoir of thermal energy that can exchange energy with the simulated system. When the system's temperature deviates from the desired temperature, the heat bath either provides or absorbs thermal energy to adjust the system's temperature.

The change in temperature of the system is proportional to the temperature difference between the system and the heat bath, with a strength parameter τ indicating the coupling between them: $dT/dt = 1/\tau \cdot (T_{\text{bath}} - T)$. The coupling parameter τ determines the strength of the interaction between the heat bath and the system. A larger τ results in a weaker coupling, meaning that the heat bath's influence on the system is milder and a smaller τ leads to a stronger coupling, where the heat bath has a more significant effect on the system's temperature. The scaling factor (λ) for the velocities in the Berendsen thermostat is given by: $\lambda = \sqrt{1 + \Delta t/\tau \cdot (T_{\text{bath}}/T - 1)}$, where Δt is the time-step. The Berendsen thermostat, although efficient, does not reproduce the proper fluctuations of the canonical ensemble. The latter is, therefore, mostly useful for equilibration purposes.

The Bussi thermostat introduces stochastic (random) fluctuations in the kinetic energy to overcome this limitation. Instead of enforcing a fixed kinetic energy value, the algorithm stochastically rescales the velocities of the particles to kinetic energy values that are randomly drawn from the canonical equilibrium distribution. This results in proper temperature fluctuations. Therefore, the velocity-rescaling thermostat introduces a stochastic term to adjust the kinetic energy distribution: $dK = (K_0 - K) \cdot \Delta t/\tau + 2\sqrt{\left(K \cdot K_0 \cdot 1/N_f\right)} \cdot dW/\sqrt{\tau}$ where K is the current kinetic energy of the system, K_0 is the desired kinetic energy, τ is the time constant for temperature control, and N_f is the number of degrees of freedom in the system.

The term "dW" refers to a Wiener process and it is used to introduce random behavior into the kinetic energy modification process. A Wiener process, also known as a Brownian motion, describes a continuous random fluctuation or increment that changes over time. It is often used to model random processes that have no memory of their past values and display a certain amount of randomness. Brownian motion is one of the most common examples of a Wiener process. It can be thought of as a random walk where each step size is random and follows a Gaussian distribution. A Wiener process is defined with an initial condition: $W(0) = 0$, meaning that the process starts at zero at time $t = 0$. The increments of the process, represented by $W(t) - W(s)$, where $s < t$, are Gaussian (normal

distribution) random variables. The increments of the Wiener process have a mean of 0 (*i.e.*, they are centered around zero) and their variance is proportional to the difference between the two time points: $Var(W(t) - W(s)) = t - s$. This variance property indicates that larger time intervals result in larger fluctuations. For nonoverlapping time intervals, the increments of the Wiener process are independent of each other – the random fluctuations in one time interval do not affect the fluctuations in another nonoverlapping interval. Thus, at each time step of the simulation, "dW" will represent a random increment that contributes to the overall change in the kinetic energy.

2.10.2 Barostat

The *NPT* ensemble is commonly used in MD where the number of atoms (*N*), pressure (*P*), and temperature (*T*) are conserved. Pressure control algorithms (aka barostats) ensure that the pressure remains at a target value throughout the simulation by applying an external stress to the system.

The Berendsen barostat[34], similar to the Berendsen's thermostat envisions the system as weakly connected to a pressure bath. Instead of directly modifying the volume, atomic positions are scaled by λ. The rate of change of pressure over time is proportional to the difference between the pressure of the bath (P_{bath}) and the system's pressure ($P(t)$). The coupling between the two subsystems is determined by the coupling constant τ, which can be adjusted for stronger or weaker coupling. While efficient for equilibration, it doesn't sample the exact *NPT* ensemble and can induce artifacts.

The Andersen barostat[35] introduces an additional degree of freedom corresponding to the volume of the simulation cell, which adjusts itself to equalize internal and external pressures. The Andersen barostat only allows for isotropic deformation of the simulation unit cell. The Parrinello-Rahman barostat[36] extends the Andersen method to allow changes in the shape of the simulation cell and dynamic shape changes. The Parrinello-Rahman barostat is widely employed in MD simulations, making it one of the most commonly used algorithms for controlling pressure. The MD simulations reported here used the latter barostat[36].

2.11 BOND CONSTRAINTS: THE LINCS ALGORITHM

LINCS is an algorithm designed to maintain the correct lengths of covalent bonds within a molecular system during MD simulations[37]. Following the calculation of new positions without considering any constraints, the LINCS algorithm is applied to enforce the desired bond lengths – in the first step of the LINCS algorithm, the new positions of atoms might result in changes in bond lengths which can be seen as "projections" of the new bond vectors onto the old bond directions. By setting these projections to zero, the algorithm resets the bonds to their desired lengths. This step ensures that any deviations from the correct bond lengths due to the unconstrained update are corrected. Similarly, atoms can undergo rotations, which can affect bond lengths. The second step of the LINCS algorithm addresses this issue as well applying a correction to account for any bond lengthening that might have occurred due to these rotations.

2.12 PROPERTY CALCULATION

2.12.1 Density

Density (ρ) is a fundamental physical property of matter that measures how much mass is contained within a given volume. Mathematically, density is defined as the mass divided by the volume, $\rho = m/V$. The standard unit for density in the International System of Units (SI) is kilograms per cubic meter (kg/m³).

2.12.2 Diffusion

The self-diffusion coefficient (*D*) can be obtained from a MD simulation either via a Green-Kubo integral involving the *N* particles velocities auto-correlation function or from the Einstein relationship which connects the diffusion coefficient to the particles' mean square displacement (MSD) over time. The Einstein relation was used in this thesis to assess the self-diffusion coefficient of the components of the DES. This is given by,

$$D = \frac{1}{6N} \lim_{t\to\infty} \frac{d}{dt} \langle \sum_i^N [|r_i(t) - r_i(0)|]^2 \rangle \quad \textbf{(2.9)}$$

where, $r_i(t)$ and $r_i(0)$ represent the positions of the ith particle at time *t* and the origin, respectively, *D* is the diffusion coefficient, and the <> represent an ensemble average of the MSD. For normal diffusion, where particles exhibit Brownian motion, the MSD exhibits linear growth at long times, allowing *D* to be estimated from the slope of the MSD. Notice the particles cannot be subject to periodic boundary conditions. Thus, a trajectory unfolding must be performed to calculate the MSD. The particles typically move farther away over time from where they started, and their individual displacements accumulate. Thus, the mean square displacement will increase. The derivative thus provides a measure of how "fast" this increase occurs. Diffusion is primarily determined by the behavior of individual particles and the statistical precision of its calculation can be improved by averaging over a larger number of particles.

When analyzing the MSD graph to calculate diffusion, we often observe two distinct regions corresponding to different types of motion: the ballistic motion and the diffusive motion (**fig. 2.5**). Initially particles exhibit ballistic motion, moving with a constant velocity and direction. As time progresses, the effects of random forces and "collisions" with other particles induce a diffusive motion, with particles moving randomly (Brownian motion). Dividing the slope of the diffusive region by six yields the diffusion coefficient, which quantifies the rate of particle spreading due to random motion.

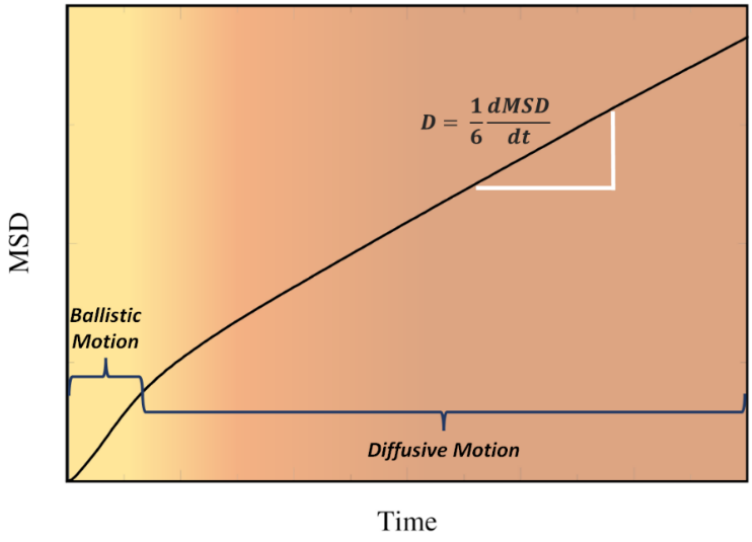

Figure 2.5. Schematic representation of the mean squared displacement (MSD) as a function of time. *At long times, the MSD plot exhibits a linear relationship, and the slope of this region is directly related to the diffusion coefficient as per Einstein's relation.*

2.12.3 Viscosity

The shear viscosity was calculated through the Green-Kubo approach, which involves the calculation of the integral of the time correlation function of the stress tensor (aka pressure tensor) elements:

$$\eta = \frac{V}{10k_BT}\int_0^\infty \left\langle \sum_{\alpha\beta}^{9} P_{\alpha\beta}(t)P_{\alpha\beta}(0)\right\rangle dt \qquad \textbf{(2.10)}$$

The $P_{\alpha\beta}$ represent the symmetrized traceless component of the stress tensor, $J_{\alpha\beta}$:

$$P_{\alpha\beta} = \frac{1}{2}\left(J_{\alpha\beta} + J_{\beta\alpha}\right) - \frac{1}{3}\left(J_{xx} + J_{yy} + J_{zz}\right)\delta_{\alpha\beta} \qquad \textbf{(2.11)}$$

where $\delta_{\alpha\beta}$ is the Kronecker delta.

This expression involves six distinct elements, out of nine, and allows improving the statistics over the original Green-Kubo formula which involves the average over only the three different off-diagonal elements, $J_{\alpha\beta} = J_{\beta\alpha}$, of the stress tensor,

$$\eta = \frac{V}{3k_BT}\int_0^\infty \left\langle \sum_{\alpha\beta}^{3} J_{\alpha\beta}(t)J_{\alpha\beta}(0)\right\rangle dt \qquad \textbf{(2.12)}$$

also used here for comparison purposes; no significant differences were found between the viscosity calculated with eqs (2.10) and (2.12).

Unlike diffusion, which is a molecular property viscosity is a collective property depending on the entire system. Thus, whereas for diffusion the calculation can be averaged over the number of molecules, this is not possible for viscosity, requiring, therefore, significantly longer MD simulations to calculate the viscosity accurately, especially for high viscous fluids such as some DES.

2.13 STRUCTURAL PROPERTIES

2.13.1 Root Mean Square Deviation

The root mean square deviation (RMSD) applied to the structure of molecules is a measure of the similarity between two molecular structures at different times. The RMSD is calculated by summing the squared distances between the corresponding atom pairs at time *t* and, for instance, time zero, and subsequently taking the square root,

$$RMSD(t) = \left[\frac{1}{N}\sum_{i=1}^{N}|r_i(t) - r_i(0)|^2\right]^{1/2} \quad \textbf{(2.13)}$$

The RMSD allows assessing the structural fluctuations in biomolecules throughout a MD simulation. In this work, the RMSD was used to evaluate the effect of a (Bet:Gly) DES on the structural stability of UBQ. Low RMSD values indicate a high degree of structural similarity between the compared molecular structures. High RMSD values indicate significant structural differences between the compared molecular structures suggesting significant conformational changes. Here, the RMSD of the backbone atoms of UBQ was used to assess differences between the structure of UBQ along the simulations with the crystal structure (1UBQ[38]).

2.13.2 Secondary Structure

DSSP (Dictionary of Protein Secondary Structure) is a method to identify and classify the secondary structure elements in proteins. This method was developed in 1983 by Wolfgang Kabsch and Chris Sander[39]. The basic principle of DSSP relies on the hydrogen bonding patterns between amino acid residues in a protein: certain patterns of hydrogen bonding occur within secondary structure elements, such as α-helices and β-sheets. The algorithm analyses the geometry and hydrogen bonding patterns for each residue, based on the coordinates of the atoms involved. When proteins are exposed to a DES, changes in its stability may be reflected in changes in its secondary structure. The DSSP algorithm provides means to quantify these structural changes and was used here to probe UBQ's secondary structure.

2.13.3 Radius of Gyration (R_g)

The radius of gyration (R_g) is a parameter that provides information about the compactness of a protein, and it is commonly used to probe structural changes throughout a simulation. R_g is defined by the root mean square distance from each residue of the protein to its center of mass and its relationship is given by equation 2.14[40–44].

$$R_g = \left[\frac{\sum_{i=1}^{N} m_i r_i^2}{\sum_{i=1}^{N} m_i}\right] \quad \textbf{(2.14)}$$

2.13.4 Solvent Accessible Surface Area (SASA)

The solvent accessible surface area (SASA) is a measure of the exposed surface area of a molecule to the solvent. Similar to the radius of gyration, SASA provides insights into the size (compactness) or exposure of protein structures to the solvent. SASA is computed by simulating the solvent with a probe sphere roughly the size of a water molecule. This probe rolls over the atoms of the

protein to model how a solvent molecule can or cannot access the protein's surface and during this process, it traces out the surface of the protein that is accessible to the solvent and any part of the protein's surface that is not covered by the probe sphere is considered inaccessible to the solvent[45]. Higher SASA values indicate a larger surface area of the protein is accessible to the solvent indicating increased interactions between the protein and the solvent. Additionally, higher SASA values in DESs may indicate increased exposure of hydrophobic regions of the protein to the solvent, potentially disrupting hydrophobic interactions that contribute to the protein's stability[46,47].

2.13.5 Radial Distribution Functions (RDFs)

The radial distribution function (RDF) describes the probability of finding a particle at a given distance from a "reference particle". The RDF is defined by the following equation,

$$g(r) = \frac{1}{N\rho}\sum_{i=1}^{N}\sum_{j\neq i}^{N}\frac{\delta(r_{ij}-r)}{4\pi r^2} \quad \textbf{(2.15)}$$

where, ρ is the numerical density (N/V) and $\delta(r_{ij}-r)$ is the Dirac delta function, formally used to account for particles found at a distance $r_{ij}=r$ while taking the value zero elsewhere. In practice finite distance bins are defined to determine whether a particle is at a distance of $r\pm\Delta r$ from the reference particle and $N(r\pm\Delta r)$ is divided by the volume $V(r\pm\Delta r)$ of the spherical bin to give the local density $N(r\pm\Delta r)/V(r\pm\Delta r)$. The factor $1/4\pi r^2$ accounts for the surface area of a spherical shell at distance r, appearing due to the integration over the spherical coordinates, θ and ϕ since $g(r)$ does not depend on the particles' orientation.

The RDF of a liquid is characterized by the existence of a few peaks, characteristic of the existence of short-range order, converging to 1 at long distances indicating that the probability of finding a particle is independent of the distance from the reference particle (absence of long range order).

The peaks in a RDF correspond to the solvation layers or coordination spheres. The number of particles in a coordination sphere can be obtained through integration of the RDF to give the respective coordination numbers (CNs). Thus, the first CN can be obtained from,

$$\mathrm{CN} = 4\pi\rho\int_0^{r_{\min}} r^2 g(r)\, dr \quad \textbf{(2.16)}$$

where r_{min} stands for the first minimum of the RDF.

2.13.6 Protein Torsional Dynamics

The torsional dynamics of the protein backbone was assessed by calculating the ϕ (phi) and ψ (psi) time correlation functions. The dihedral time correlation function proposed by van der Spoel and Berendsen was adopted[48]. The latter is given by,

$$C(t) = \langle cos[\alpha(0)]cos[\alpha(0+t)] + sin[\alpha(t)]sin[\alpha(0+t)]\rangle \quad \textbf{(2.17)}$$

in which $C_\alpha(t)$ reduces to the fundamental Pythagorean trigonometric identity at zero delay time, that is, $C_\alpha(0) = 1$, and where $\alpha = \phi, \psi$ were assessed.

2.13.7 Water Orientational Dynamics

The orientational dynamics of water was also studied through the calculation of the orientational auto-correlation functions[49],

$$C_l(t) = P_l[u_{rOH}(0) \cdot u_{rOH}(t)] \quad \textbf{(2.18)}$$

where $\mathbf{u}_{\mathbf{rOH}}$ is the intra-molecular OH unit vector and P_l is the l^{th} order Legendre polynomial (l = 1, 2, and 3); results are reported for l = 2.

CHAPTER 3

Force Field Optimization for Deep Eutectic Solvents

3.1 MOLECULAR DYNAMICS SIMULATIONS OF DESs

MD simulations provide a powerful tool to understand the behavior of DESs at the molecular level and, therefore, gain insight into their unique properties. For instance, the influence of water on the structure of (ChCl:U) DES was assessed by several groups through MD[50–52]. These studies were important to attempt to understand the structure of the DES at a molecular level, with a recent MD study[51] arguing against the conclusions from neutron diffraction and the empirical potential structure refinement (EPSR) method, concerning the non-monotonic hydration of the components with the water molar ratio[6].

The role of water on the structure of (Bet:Gly) was also recently studied through MD simulations[53]. A relatively smooth transition from a DES to an aqueous solution of the components was found in that study, with a major structural transformation at 70 mol %; 29.5 wt % water.

The accurate characterization of DESs through MD simulations presents a significant challenge due to the intricate interplay of ionic interactions, hydrogen bonding, and strong polarization effects. Additionally, DESs are a relatively new class of solvents, and limited experimental data is available, making it difficult to validate the force fields. The number of possible combinations of HBAs and HBDs is vast and the way each organic molecule affects the properties of the solvent does not follow a straightforward or predictable pattern. This makes it challenging to develop a force field that is universal and applicable to all DESs, and instead, it is often necessary to optimize a force field for each component in a mixture. This process can be time-consuming and computationally expensive. Polarizable force fields offer a potential solution by allowing charge redistribution in response to electric fields. Nonetheless, the associated computational costs have deterred their generalized adoption.

Here we reparametrized a GAFF-based force field for both betaine (Bet) and glycerol (Gly) to accurately describe the density and viscosity of the neat DES.

3.2 GAFF OPTIMIZATION

GAFF provides a set of parameters for the bonded and non-bonded interactions of a molecule, based on AMBER bond lengths, angles, and dihedral correlations, Lennard-Jones parameters, and a set of charges calculated either through electronic structure calculations or a semi-empirical method. GAFF is, therefore, compatible with AMBER allowing simulating a GAFF molecule along with biomolecules modelled by AMBER. However, since GAFF was developed based on parameters for molecules in an aqueous environment it is not surprising that such force fields may not accurately describe the properties of the respective substances. Thus, one common approach is to optimize the force field charges to match some experimental properties. There is no generalized value for the atomic charges scaling factor, and this usually requires testing a range of different values to find the optimal one for a specific system.

In this work we carried out a rescaling of the electrostatic parameters and Van der Waals radius, for reasons discussed below, to simulate (Bet:Gly:Wat) (1:2:ζ; ζ = 0,1,2,5, and 10) DES.

3.3 METHODS

3.3.1 Partial Charges Calculation

Atomistic models of Bet (canonical SMILE: C[N+](C)(C)CC(=O)[O-]) and Gly (canonical SMILE: C(C(CO)O)O) were obtained using the Avogadro software (version 1.2.0). The geometries of the DES's components, Bet and Gly, were then optimized through density functional theory, at the B3LYP and 6-31G* basis set theoretical level. Vibrational analysis was carried out to assure that the optimized geometry corresponded to a local or global minimum, and that no imaginary frequencies occurred; a single imaginary frequency would correspond to a first order saddle point, a transition state in the potential energy surface, symbolically identified with a minus sign.

Merz-Singh-Kollman charges[54] were computed at the HF/6-31G* level in the gas phase, the theoretical level prescribed in the GAFF approach. All QM/MM calculations were carried out using the Gaussian09 software package[55]. RESP charges[56] were then computed using the "Antechamber" program, which is part of the AmberTools suite[57]. The generated charges were later modified to improve the force field's accuracy. The Lennard-Jones sigma (σ) was also adjusted. The reparametrized force field that provided the best agreement with the experimental data was then used to study the stability of a prototypical globular protein, ubiquitin (**Chapter 4**).

3.3.2. Molecular Dynamics Simulations

MD simulations were performed in the *NPT* ensemble using the GROMACS software package[58]. The simulation system was enclosed in a cubic box, with periodic boundary conditions. To control the temperature and pressure, the thermostat developed by Bussi *et al.*[33] and the Parrinello-Rahman barostat[36] were used. Electrostatic interactions were computed using the particle-mesh Ewald method[32]. A 1 nm cutoff distance for non-bonded van der Waals interactions and the real space component of the electrostatic interactions was used. Additionally, the covalent bonds between heavy atoms and hydrogen atoms were constrained with the LINCS algorithm[37]. The simulations of the anhydrous DES involved a system comprising 128 Bet molecules and 256 Gly molecules. MD of the DES with water (Bet:Gly:Wat) (1:2:ζ; ζ = 1,2,5, and 10) comprised 128 molecules of Bet, 256 molecules Gly, and 128, 26, 640, and 1280 water molecules. The leap-frog algorithm[59] was employed to solve the equations of motion with a time-step of 1 fs.

To ensure meaningful results, the simulations were run for a total duration of 1 μs, allowing for the accurate calculation of the viscosity.

3.4 RESULTS AND DISCUSSION

We first assessed the quality of the "unchanged" RESP atomic charges and, as expected, these failed to reproduce the experimental data. Thus, both the density and viscosity were found to be overestimated (see **fig. 3.1 (a-b)**). Furthermore, according to the calculated viscosity, the (Bet:Gly) model is possibly a solid. Whereas the density was not too far off from the experimental value, the computed shear viscosity was completely unsatisfactory making it impossible to validate the GAFF model.

Nonbonded parameters, used to define intermolecular interactions such as electrostatic interactions, have a strong impact on the way the molecules interact with one another and, consequently, on the DES properties. Hence, the initial focus involved the manipulation of the atomic charges to improve the force field's predictive accuracy. Specifically, the atomic charges were scaled by a factor $\lambda_Q < 1$ to decrease the density and viscosity of the DES via a weakening of the electrostatic interactions.

The scaling procedure using λ_Q ranging between 0.8 and 1 revealed that, although the density exhibited a slow decay with decreasing λ_Q (**fig. 3.1 (a)**), viscosity displayed a marked sensitivity to electrostatic charges, characterized by a rapid decline (**fig. 3.1 (b)**). No single λ_Q value allowed simultaneously reproducing both the density and viscosity, thereby highlighting the inadequacy of GAFF in accurately modeling the DES through charge scaling alone (see **Appendix A Table A.1**). This overestimation of the density suggested the formation of overly compact structures.

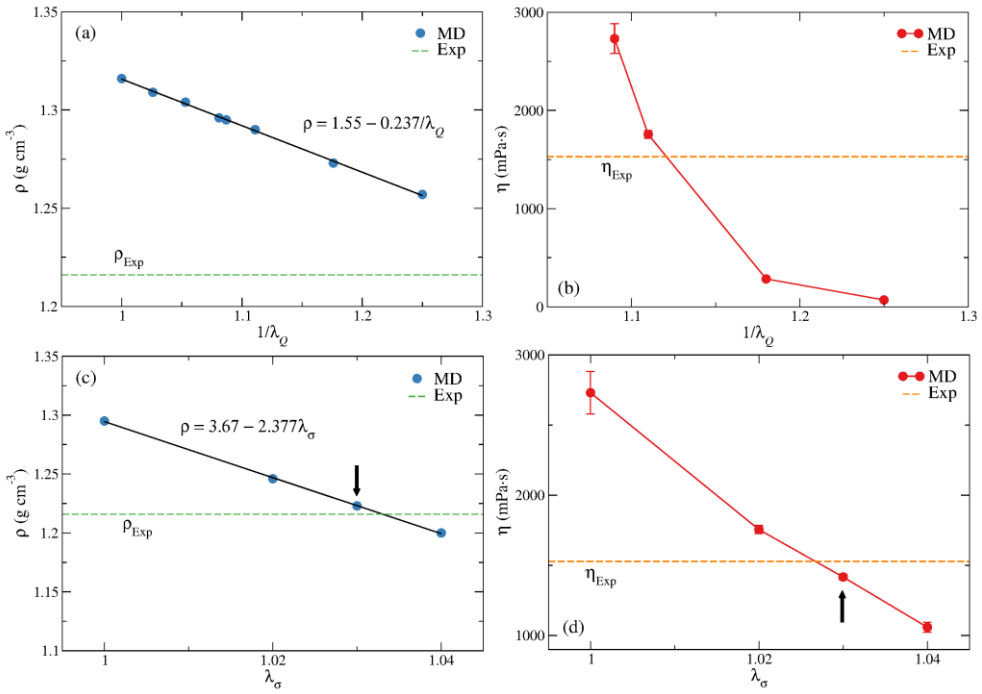

Figure 3.1. Charge and van der Waals radius scaling factors with density and viscosity. *(a) Relationship between the charge scaling factor, λ_Q, and the density of the system. (b) Viscosity dependency of λ_Q. (c) Density dependency and (d) viscosity dependency of λ_σ with λ_Q fixed at 0.92.*

A second scaling factor ($\lambda_\sigma > 1$) was, therefore, introduced to manipulate the LJ potential's σ value, in particular, to reduce molecular compactness and, therefore, the density.

The application of a second scaling factor allows for more flexibility in adjusting the force field to match the experimental properties. This, in turn, introduces the possibility of finding several combinations of scaling factors that could accurately describe both properties (density and viscosity).

A series of preliminary calculations with λ_Q= 1 and varying λ_σ showed a fast decrease of the density while η decreased more gradually. Based on these observations, λ_Q was set in a way that the resulting viscosity was slightly higher than the experimental value. Then, λ_σ was adjusted to obtain a density that closely matched the experimental value (**fig. 3.1. (c) and (d)**). This procedure allowed minimizing λ_σ, and, therefore, placing most of recalibration into the electrostatic charges.

The optimized GAFF force field (GAFF-opt) scaling parameters were λ_Q = 0.92 and λ_σ = 1.03, corresponding to an 8% reduction in atomic charges and a 3% increase in atomic σ. The results demonstrate that GAFF-opt exhibits a minor overestimation of the experimental density by 0.58% (1.216 g/cm^3) and a viscosity underestimation of approximately 7%, as summarized in **Table 3.1**.

Table 3.1. Influence of van der Waals radius scaling on (Bet:Gly)'s properties.

Exp./MD λ_σ	ρ (g·cm^{-3})	η (mPa·s)
Experimental	1.216	1528
1.00	1.294	2731 ± 151
1.02	1.246	1755±29
1.03[a]	1.223	1417±20
1.04	1.200	1059±35

[a] λ_σ chosen to run the MD simulations of ubiquitin.

Analysis of (Bet:Gly) at various water content levels is presented in **fig 3.2**. The figure shows the variation of ρ and η with the water content ζ (ζ = 0, 1, 2, 5, and 10) corresponding to the following water molar percentages (mol %) 25, 40, 62.5, 76.9, and weight percentages (wt %), 5.6, 10.7, 23.0, and 37.4. The ρ and η were fitted to the equation: $Z = Z_0 * exp[-a_z / (\zeta + b_z)]$, where Z is either ρ or η, while Z_0, a_z, and b_z are property dependent empirical. This equation was previously shown to describe well the density, viscosity, self-diffusion, and structural parameters for different DESs systems[51,53].

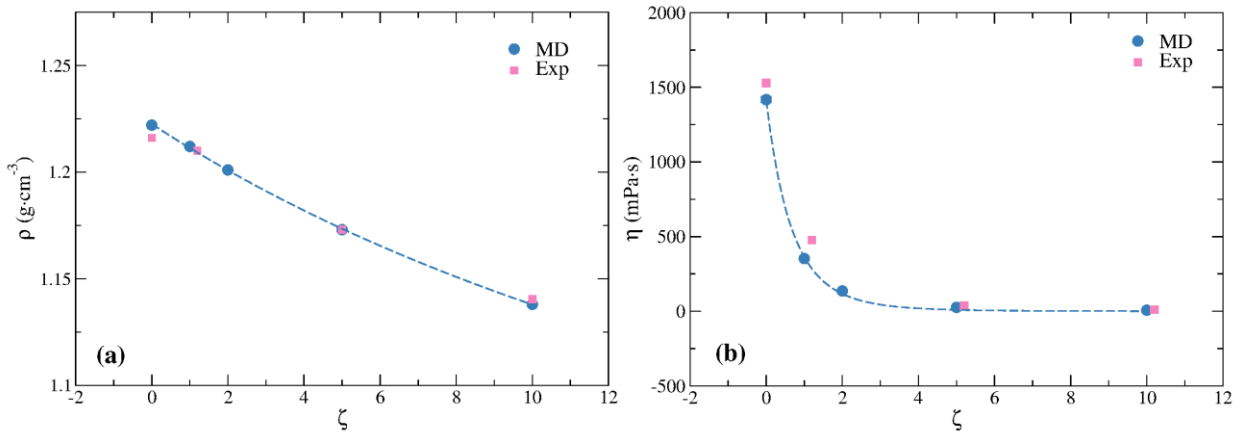

Figure 3.2. (Bet:Gly:Wat) DES properties at 298 K and 0.1 MPa. *(a) Density and (b) Shear Viscosity of (Bet:Gly:Wat) at various compositions (1:2:ζ; ζ = 0, 1, 2, 5, and 10) under standard conditions of 298 K and 0.1 MPa.*

Remarkably, the obtained results exhibit a high level of agreement with the experimental data for density (**fig. 3.2 (a)**). However, when it comes to viscosity, the model slightly underestimates the values, with the extent of error diminishing as the water content increases (**fig. 3.2 (b)**).

A comparative analysis with an alternative FF, OPLS-aa, recently reported in our group[53] is also provided. Notably, both FFs align well in terms of RDFs. Insights into the RDFs show that GAFF-

opt has modestly lower coordination numbers when compared to OPLS-aa (**fig. 3.3**). In spite of an increase of the σ in the GAFF-opt, relative to the GAFF model, it can be seen that the onset of the RDFs still appears at shorter distances compared with the OPLS-aa, with the exception of the Gly-Gly RDF for which these are similar (**fig. 3.3 (c)**).

The RDFs at different water contents were also calculated (see **Appendix A fig. A.1**) showing the effect of water penetration in the DES's components coordination spheres as the water fraction increases. These results are much similar to those reported by Monteiro *et al.*[53] with the above mentioned OPLS-aa force field.

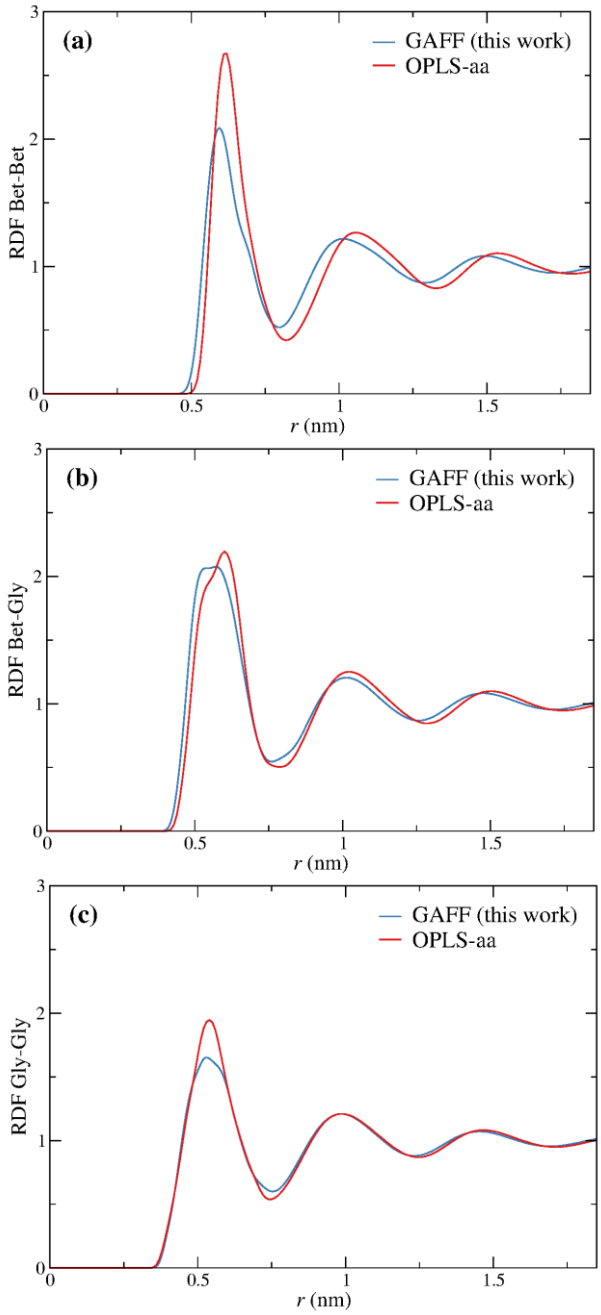

Figure 3.3. ***Radial distribution functions for different component pairs within the (Bet:Gly) DES using GAFF and OPLS-aa.*** *Panels (a), (b), and (c) display RDFs for Betaine-Betaine, Betaine-Glycerol, and Glycerol-Glycerol, respectively. The RDFs were computed using the GAFF-opt force field developed in this study and are compared with those obtained with the OPLS-aa force field proposed by Monteiro et al.*[53]].

3.5 CONCLUSION

This study sought to refine GAFF to improve its accuracy in predicting properties like density and viscosity for a NADESs: (Bet:Gly). The inability to reproduce the density and viscosity reinforced the insufficiency of the default GAFF parameters. The approach of solely manipulating atomic charges through scaling factors was found to be insufficient, as no single scaling factor could simultaneously capture both the density and viscosity; we demonstrated that reducing atomic charges led to a significant decrease in viscosity while the effect on density was relatively smaller. To address these issues, an approach involving a second scaling factor operating upon the σ of the Lennard-Jones potential (*i.e.*, the vdW radius) was introduced. By iteratively adjusting the scaling factors, an optimized GAFF force field (GAFF-opt) was developed. This optimized force field exhibited an 8% reduction in atomic charges ($\lambda_Q = 0.92$) and a 3% increase in atomic sigma ($\lambda_\sigma = 1.03$). GAFF-opt demonstrated improved predictive accuracy, with a minor 0.58% overestimation of experimental density and an underestimation of viscosity by approximately 7%. These findings collectively suggest that the proposed modifications to GAFF effectively addressed the limitations of the original force field and brought it closer to experimental observations for DESs.

CHAPTER 4

Protein Stability in Deep Eutectic Solvents: Solvent Dynamics and the Role of Water

4.1 THE HIDDEN THIRD LIQUID PHASE OF LIFE

Water is the primary solvent of life as most cellular processes take place in an aqueous environment. Lipids are a diverse group of molecules that includes fats, oils, and certain components of cell membranes. Lipid-rich environments provide a medium for processes like membrane formation and energy storage. Intriguingly, numerous biological reactions involve molecules like secondary metabolites (paclitaxel, terpenoids, flavonoids) and macromolecules (lignin, cellulose) that often demonstrate poor solubility within traditional cellular environments[60].

One key characteristic of NADESs is that they often contain naturally occurring osmolytes – small organic molecules involved in processes like osmoregulation and protection against stress. The presence of naturally occurring osmolytes, like sugars, polyalcohols, and amino acids, in similar concentrations to the components known to form NADESs, raises the possibility that nature might have leveraged NADESs since early-stages of life for diverse functions. This concept was initially proposed by Choi and colleagues in 2011[61].

The authors found these components exist in the cells in a proportion that is conducive to the formation of NADESs, suggesting that the necessary conditions for NADESs formation are naturally occurring within the cells. The consistency of this molar ratios aligning with conditions favoring NADESs formation supports the idea that organisms have evolved to maintain this ratio for specific functional purposes. This consistency may indicate a purposeful adaptation or strategy developed by organisms to harness the benefits of NADESs. Based on these findings, it was proposed that: *"Everywhere in living systems NADESs occur and form a third liquid phase of intermediate polarity"*[62].

The presence of NADESs in the cell provides a possible explanation for a variety of biochemical processes that involve compounds which are not soluble in the usual aqueous (water-based) or lipid (fat-based) environments. For instance, it could shed light on the processes of biosynthesis, including the transport and storage of compounds that are not soluble in water. Remarkably, studies on the solubility of secondary metabolites and macromolecules emphasize the aptitude of NADESs to dissolve and extract these compounds[60,63–66].

Furthermore, this concept could provide insights into how certain biological entities, like seeds, manage to endure extended periods of drought and cold. The presence of NADESs might even play a role in the water uptake mechanism of cacti from the atmosphere. Thus, this hypothesis suggests that NADESs might have important roles within organisms like metabolite solubility, storage and transport, water content regulation, and cellular protection.

4.2 PROTEIN FOLDING, STRUCTURE, AND MISFOLDING

Proteins are often dubbed the cellular workhorses due to their diverse and indispensable functions within living organisms. Proteins serve as hormones (*e.g.*, insulin), cellular receptors (*e.g.*, insulin receptors), membrane channels and transporters, the cytoskeleton (*e.g.*, actin and tubulin), transporters of various substances in the blood, antibodies, transcription factors, an energy source, etc. Their significance is underscored by their prevalence, accounting for more than half the dry weight of a cell[67].

The folded structure is essential for the protein's biological activity and proper function. The amino acid sequence determines how the protein will fold in the endoplasmic reticulum (ER). Therefore, the stabilization of their native structure is a critical aspect for all biological organisms. However, their native structure and, consequently, function, can be disrupted by destabilizing factors such as changes in temperature, pH, hydration, and/or the presence of chemical denaturants[68].

Most proteins (*i.e.*, globular proteins) have primary, secondary, and tertiary structures. Constructed from a set of 20 amino acids dictated by the genetic code and synthesized within the ribosome after translation from mRNA, the primary structure of a protein is the linear sequence of amino acids (random coil) linked together through peptide bonds. Hydrogen bonds form between atoms in the polypeptide backbone, creating structures like α-helices and β-sheets. α-helices, the most prevalent secondary structures, are coiled structures stabilized by hydrogen bonds between the peptide backbone's –CO–NH– groups. β-sheets consist of extended strands forming a pleated sheet arrangement and they come in parallel and antiparallel forms. The folding of secondary structures involves hydrophobic interactions, hydrogen bonding, electrostatic interactions, van der Waals forces, and disulfide bonds, which contribute to the stabilization of this tertiary structure. This structure is critical for the protein's function and determines its active site, binding pockets, and overall shape. Some proteins are composed of multiple polypeptide chains that interact to form functional complexes – quaternary structures – and these are complex proteins with multiple functional subunits.

The pioneering experiments by Anfinsen emphasized that, under favorable conditions, a protein consistently folds into its unique native structure dictated by its amino acid sequence, a concept for which Anfinsen received the Nobel Prize in Chemistry in 1972. But while amino acids impart traits through their side chains, a protein's native/folded structure possesses characteristics that transcend the sum of individual amino acid attributes. The proper folding of proteins is influenced by various external factors like temperature, pH, interaction with other chemicals, mechanical forces, molecular crowding, electric and magnetic fields, or solvent fluctuations.

DESs have been explored as potential media for the preservation of biomolecules. DESs could provide a tailored and protective environment that preserves protein structure, activity, and stability making them valuable tools in a wide range of applications, such as basic research, pharmaceutical development, cryopreservation, where the integrity of stored proteins is critical.

The objective of this study is to investigate how a NADES, (Bet:Gly) with varying water molar ratios, affects the protein's structure, dynamics, and stability of a protein, ubiquitin.

4.3 OSMOLYTES AND NATURAL DEEP EUTECTIC SOLVENTS

Osmolytes can help stabilize proteins and preserve their function in aqueous systems (*e.g.*, the cellular environment) by shielding them from denaturing stresses like dehydration and freezing. They accumulate in cells as a response to abiotic stresses and can be classified into four main categories: polyols (sugars and sugar derivatives), uncharged amino acids, amino acid derivatives, and methyl ammonium compounds[69]. The presence of osmolytes has been shown to significantly enhance the stability of proteins and preserve enzymatic activity. This is believed to be associated with the exclusion of the osmolytes from the protein surface (*i.e.*, preferential exclusion/preferential hydration mechanism) leading to an increase in the surface tension of water that counteracts any increase in the surface area, typical of denatured conformations, thus promoting protein-protein interactions which means that proteins can retain their folded shape – preferential hydration[70]. Basically, the preferential hydration of a protein and consequent exclusion of the osmolytes from the protein surface results in a destabilization of the unfolded states in the presence of osmolytes[71]. Thus, osmolytes don't interfere with the proteins' structure leaving the native state mostly unaltered in the absence of stress factors, which allows enzymes to maintain similar catalytic activities at high osmolyte concentrations. Therefore, osmolytes are often seen as potential stabilizers for enzymes and proteins in industrial processes (*e.g.*, to preserve the activity of enzymes/proteins during storage and transportation), for biopharmaceutical formulations, or to increase the stability and shelf-life of products.

4.3.1 Betaine

Betaine (aka trimethylglycine) is a naturally occurring osmolyte present in several organisms such as plants (sugar beet molasses - primary source of betaine for industrial production[72] -, spinach, and whole grains), animals (including humans) and microorganisms. The chemical structure of betaine ((CH3)3N+CH2COO-) consists of a central nitrogen atom (N_{BET}) that is attached to three methyl ($-CH_3)_{BET}$ groups and one carboxyl $(-COO^-)_{BET}$ group. Betaine is a zwitterionic molecule[73] meaning that it has both a positive and a negative charge. N_{BET} has a positive charge due to the presence of three electron-donating $(-CH_3)_{BET}$ groups, each of which donates an electron to N_{BET}. However, N_{BET} remains positively charged because it is bonded to one $(-COO^-)_{BET}$ group at the other end of the molecule which is negatively charged. The negative charge on the $(-COO^-)_{BET}$ group is justified by the presence of a lone pair of electrons on the oxygen atom in the carboxyl group due to the loss of a proton. The positive N_{BET} atom and negative $(-COO^-)_{BET}$ group balance each other out, resulting in a zwitterionic structure for betaine.

Betaine is a hygroscopic[74], crystalline powder that is soluble in water and polar solvents (such as methanol, ethanol, and propanol[75]). It has a molecular weight of 117.15 g/mol[76] and a melting point of approximately 570 K[77]. The overall pK_a value of betaine is approximately 1.8, which means it acts as a strong acid. At a pH below its pK_a, the concentration of protons is higher than the concentration of betaine and thus, betaine will exist primarily in its protonated form and in this state, the carboxyl group of betaine is protonated and carries a neutral charge $(COOH)_{BET}$,. The higher hydrophobicity of the protonated form of betaine will be reflected in a lower solubility in water. At a pH above its pK_a, betaine will exist primarily in its deprotonated form. The methyl groups in betaine contribute to its overall hydrophobicity, which can affect its solubility in nonpolar solvents. At physiological conditions, (pH higher than pK_a), betaine exists primarily in its deprotonated form – the zwitterionic state. Betaine's ability to protect cells from osmotic stress is thought to be related to its zwitterionic nature[78]. Betaine is known for its crucial role in the metabolic cycle of methionine by serving as an alternative source of a methyl group essential to synthetize methionine (an essential amino acid) from the metabolization of homocysteine[79].

As an osmolyte, betaine is involved in osmoregulation and cell protection[80,81]. It stabilizes proteins[82–84], by being excluded from the hydrophobic side chains[85], membranes[86], cell volume, growth rate in microorganisms, protects against apoptosis[87] and helps to maintain proper protein folding[88] and enzymatic activity[89]. Betaine's carboxyl group can form hydrogen bonds with water[90] which enhances its solubility in aqueous environments and helps prevent water loss from the cell. While osmolytes typically stabilize proteins *in vivo*, the effect of betaine on protein seems to be concentration-dependent[91]. Natalello *et al.*, found that they could manipulate the formation of soluble protein assemblies and insoluble aggregates, as well as disassemble or dissociate aggregates that have already formed in a protein sample by adjusting the betaine concentration[91].

4.3.2 Glycerol

Glycerol (aka glycerine or propane-1,2,3-triol), is an organic molecule widely used in the pharmaceutical, cosmetics, and food industries. Approximately 90% of glycerol production is achieved by processing natural oils or fats, where glycerol is obtained as a by-product through processes like saponification or transesterification[92].

Glycerol (C(C(CO)O)O) is a clear, colorless, and odorless liquid with a sweet taste composed of a three-carbon chain, and each carbon atom has a hydroxyl group (-OH) attached to it. Glycerol's three hydroxyl groups influence its solubility, *i.e.*, it is completely soluble in water and alcohols, phenol,

glycol, amines, and other solvents, but has limited solubility in acetone, diethyl ether, and dioxane. The presence of hydroxyl groups also makes it a good solvent for substances like iodine and bromine. Glycerol's solvent capabilities extend to organic and inorganic solids, making it important in pharmaceutical preparation[92,93].

It is hygroscopic, retaining moisture from the air until equilibrium with atmospheric water vapor is achieved[92]. It has a high viscosity, making it sticky. Its boiling point is 563.15 K under standard atmospheric pressure (0.1 MPa) and its melting point is 291.15 K. Under normal atmospheric pressure and at 293.15 K, glycerol has a molecular weight of 92.09 g/mol, a density of 1.261 g/cm^3, and a viscosity of 1.5 Pas. The high viscosity and boiling point are due to extensive intermolecular hydrogen bonding[93].

One of the most notable reactions to osmotic stress is the synthesis and accumulation of glycerol. When *Saccharomyces cerevisiae* experiences a sudden decrease in external osmolarity, they undergo a rapid release of their internal glycerol content. Under hypo-osmotic conditions, Fps1p channels open up, allowing the efflux or release of glycerol from inside the cell to the external environment. This controlled release of glycerol helps the yeast cells adapt to the sudden decrease in external osmolarity and maintain their internal balance. On the other hand, when yeast cells encounter hyper-osmotic conditions, Fps1p channels close, preventing glycerol from leaving the cell. This mechanism helps cells retain glycerol when facing increased osmotic stress[94].

The protective mechanism by which polyols exert their effects on proteins is a subject of ongoing debate. One prevailing explanation is preferential hydration. In this context, polyols like glycerol are excluded from the protein's surface, leading to favorable interactions between water molecules and the protein. This promotes a hydrated environment around the protein, which contributes to its stability. This concept of preferential hydration suggests that polyols protect proteins indirectly through their impact on the solvent environment. MD simulations suggested that glycerol does not form strong hydrogen bonds with proteins, supporting the notion of preferential hydration. This implies that glycerol's protective effect is mainly due to its non-contact influence on the solvent environment surrounding the protein[95].

However, other researchers have proposed different mechanisms. Vagenende and collaborators used MD simulations to show that glycerol can engage into significant electrostatic and hydrophobic interactions with specific protein side chains, resulting in the creation of an amphiphilic protein surface. This amphiphilic surface acts as a protective shield, preventing unwanted conformational changes and the aggregation of protein molecules. This mechanism was thought to lead to compact protein conformations with reduced SASA stabilization of partially unfolded intermediates. Contrary to the common belief that protein stabilization by polyols is determined solely by the molecular size of the polyol, it was found that glycerol-induced protein compaction primarily arises from electrostatic interactions. These interactions guided the orientation of glycerol molecules at the protein surface, resulting in the exclusion of glycerol from certain regions. Regions of the protein surface characterized by hydrophobicity and amphiphilic characteristics were more likely to interact preferentially with glycerol. These regions tended to be solvated by glycerol, especially in cases where protein intermediates were prone to aggregation. The researchers hypothesized that glycerol prevents protein aggregation by inhibiting protein unfolding and by stabilizing partially unfolded intermediates through preferential interactions with hydrophobic surface regions. Another mechanism involved the preferential hydration of specific regions in proximity to the protein surface[96].

At lower concentrations, glycerol's stabilizing effects dominate, and it helps maintain the native structure and function of proteins. However, glycerol can indeed exhibit some level of toxicity to cells and tissues.

4.3.3 Betaine-Glycerol (1:2) Natural Deep Eutectic Solvent

Although it's been commonly used as a hydrogen bond donor, glycerol doesn't strictly fit the criteria of a DES, where both components are solid at room temperature. However, the exact adherence to this specific definition will not concern us here[53].

4.3.4 Protein Dynamics and Solvent Fluctuations: Preferential hydration and/or Solvent Slaving

Although proteins are commonly portrayed as static structures, they are dynamic, continuously experiencing fluctuations. The atoms within a protein continuously vibrate and rotate, resulting in structural fluctuations. Fluctuations are crucial for enabling various processes, such as ligand binding and unbinding. The so-called β-fluctuations are primarily driven by the intrinsic properties of the molecule, although the presence of a solvent environment can modulate their occurrence and dynamics to some extent. However, the dominant influence of the solvent is often observed in α-fluctuations, where the solvent can strongly affect the rates and pathways of larger-scale conformational changes and transitions, such as protein folding and ligand binding[97]. These two types of fluctuation have been rationalized into a protein solvent slaving mechanism[98].

Slaving refers to a dependency between the motions of proteins and the movements of the surrounding solvent. This implies that protein motions are directly dependent on the fluctuations of the surrounding solvent molecules. The solvent molecules are not stationary; they are in a constant state of motion which causes them to constantly rearrange and fluctuate in their positions around the protein. As these molecules move and fluctuate near the protein, they interact with the protein, affecting its conformational changes and dynamic behavior.

There are two distinct classes of protein processes based on their relationship to solvent fluctuations[98]:

(1) Nonslaved processes in which protein motions are independent of solvent fluctuations and do not rely on changes in the temperature-dependent behavior of the solvent. Such processes occur regardless of the fluctuations of the surrounding water molecules within the solvent. One specific example of a nonslaved process is the rebinding of carbon monoxide (CO) to a protein. This process happens directly between the CO molecule and myoglobin (a protein responsible for the storage of O_2 in the muscles) without significant involvement or influence from the surrounding solvent molecules. Instead, it occurs primarily due to the specific binding affinity and interactions between the protein and the CO molecule[98];

(2) Slaved processes in which the protein motions are directly influenced by solvent fluctuations and exhibit temperature dependencies similar to the temperature-dependent behavior of the solvent. These processes depend on the dynamics of the surrounding solvent. When the solvent has a higher viscosity, the slaved protein motions may occur at a slower rate because the water molecules become trapped within the solvent. Conversely, when the solvent has a lower viscosity, the water molecules can move more freely and interact more readily with the protein resulting in faster protein motions and more rapid conformational changes. Changes in the rates of slaved protein motions due to changes in solvent viscosity can have important biological implications: for instance, in a cellular environment, various factors can influence the viscosity of the cytoplasm, or the extracellular environment and they may affect the behavior and function of proteins, such as enzymatic activity, ligand binding, and conformational changes essential for cellular processes. One specific example of a slaved process is the escape of CO from myoglobin into the surrounding solvent. As the CO molecule is released from the protein's binding site, its escape into the solvent is influenced by the dynamics of the solvent. The rate of CO escape occurs at a frequency proportional to the solvent fluctuation rate.

The rate coefficients of chemical reactions often follow an Arrhenius law, where the rate is proportional to exp(-E_a/RT), where E_a is the activation energy, R is the gas constant, and T is the absolute temperature. However, in the case of the rate at which ligand escape occurs, $k_{exit}(T)$, and other related rate coefficients, this Arrhenius behavior is not observed. The rate coefficient $k_\alpha(T)$ represents the rate of the relaxation process of the solvent. For some proteins the two rate coefficients, $k_{exit}(T)$ and $k_\alpha(T)$, show similar behavior suggesting a relationship between protein motions and solvent dynamics[97,99].

However, $k_{exit}(T)$ is noticeably slower compared to $k_\alpha(T)$, indicating that the protein's motions are influenced by the solvent but occur at a significantly different pace. The slowing of $k_{exit}(T)$ is attributed to the fact that large-scale protein motions involve numerous elementary steps, denoted as n_{exit}. Large-scale motions of the protein involve a series of smaller, elementary steps that collectively lead to the overall motion and each of these elementary steps requires the involvement of the solvent, implying that the rate of protein motions depends on the rate of solvent fluctuations and the rate at which the protein undergoes these steps is directly connected to the rate of solvent fluctuations[97]. Mathematically, $k_{exit}(T)$ is described as

$$k_{\text{exit}}(T) = \frac{c \cdot k_\alpha(T)}{n_{\text{exit}}(T)} \quad \textbf{(4.1)}$$

where c is a coefficient accounting for the interaction between solvent fluctuations and protein motions. The equation suggests that the rate of protein motion ($k_{\text{exit}}(T)$) is a product of the solvent relaxation rate ($k_\alpha(T)$), the number of elementary steps ($n_{\text{exit}}(T)$) involved in the motion, and the interaction coefficient (c). Both protein folding and large-scale motions involve the exploration of different conformations on the energy landscape. The rate of myoglobin's structural relaxation upon CO release, for instance, is approximately inversely proportional to the first power of the viscosity of the surrounding solvent, meaning that in a more viscous environment, myoglobin undergoes conformational changes more slowly[100].

According to Kramers' theory[101], a protein is assumed to exist in two stable states, A and B which correspond to two distinct structural conformations.

Metastable states are the intermediate configurations that are relatively stable but not as stable as A and B. These states exist in the potential energy landscape as local minima. In the context of protein folding, one state typically represents the native (N) and biologically functional conformation, and the second state represents the unfolded (U) conformation of the protein, where it lacks its defined three-dimensional structure. The two stable states, N and U, are separated by a potential energy barrier which the protein needs to overcome to transition from N ↔ U.

In this N ↔ U transitioning process, the system passes through several unstable intermediate states, referred to as the transition states "S". Kramers' theory states that the reaction rate depends on the activation energy of the transition. In the Kramers high friction regime, the combined effects of the solvent's interactions with the reactant molecules lead to a high degree of friction in the system. This means that the combined effects of the solvent's interactions with the N ↔ U process is significantly influenced by the surrounding solvent.

The rate of the reaction (denoted as κ) represents the probability of crossing the energy barrier and successfully transitioning from state A to state B. In the Kramers high friction regime, κ is inversely proportional to the solvent viscosity. In the context of folding and unfolding of proteins, κ represents the folding rate and it is given by:

$$\kappa = \frac{A}{\eta} \exp\left(\frac{\Delta G}{k_B T}\right) \quad \textbf{(4.2)}$$

Here, A is a constant and ΔG is the free energy barrier for folding. Thus, the results reported by Ansari *et al.* are consistent with the predictions of Kramers theory.

However, it was observed that in some folding experiments, κ does not follow the expected 1/η dependence[97]. Instead, it was found that in fast processes like dihedral angle motions in α-helix formation, κ follows a power-law dependence on the solvent viscosity, η^(-α), where $0 < \alpha < 1$[102].

4.4 PROTEIN STABILITY IN DEEP EUTECTIC SOLVENTS

There has been a growing trend in investigating DESs as environmentally friendly mediums for application in biochemical processes, with a specific emphasis on biomolecular stability and catalysis. For instance, the effect of different DESs on the catalytic activity of cytochrome P450 BM-3 in producing indigo (indigo is not soluble in water and its production involves the use of various chemical pollutants), a blue dye, from indole, was investigated to find more environmentally friendly and efficient production methods[103]. A direct relationship between the pH, water content, and temperature of the DESs and the catalytic activity of the P450 BM-3 enzyme was found, suggesting that optimization of these parameters can enhance the efficiency of the catalytic process in DESs. The physical properties of the DESs are affected by the water content and temperature of the solvent. For example, an increase in water content results in a significant decrease in the viscosity of the DESs. These changes in the physicochemical properties can affect the stability and catalytic activity of enzymes.

Gorke *et al.*[104] showed for the first time that the denaturing effect of urea can be antagonized by the presence of ChCl. Not only was unfolding avoided, but also enzymatic activity was preserved in a (ChCl:U) (1:2) DES. This experimental result raised several questions about the dynamic behavior of (ChCl:U) in the presence of an enzyme. It was only possible to understand how the enzyme, Candida antarctica lipase B (CALB), interacts with urea and choline chloride, at an atomic level, through MD studies[105]. ChCl and CALB form hydrogen bonds, and these CALB-ChCl interactions prevent urea from interacting with CALB's core. In addition to enzymatic stability in DESs with high urea concentrations, perhaps the most groundbreaking result was the improvement of the catalytic activity in the presence of a (ChCl:Gly) DES[104].

On another study, the structure of native horseradish peroxidase (HRP), comprised by 31% α-helix, 9% β-sheet, 16% turns, and 44% random coil, was investigated in various NADESs. While no significant changes in the random coil (~42%) and turns (~15%) content, compared to the PBS control, variations were observed in α-helix and β-sheet contents depending on the NADES. Thus, in Betaine:Xylose:Water, α-helix and β-sheet contents became nearly equal (20% α-helix and 23% β-sheet), whereas in Betaine:Sorbitol:Water , there was an increase in α-helix at the expense of a β-sheet decrease (35% α-helix and 5% β-sheet). The structural changes induced by (Bet:Sorb:Wat) are thought to favor enzymatic activity since activity loss has been associated with diminished α-helix content. Decreasing α-helix structure by about 18% led to a reduction of relative HRP activity to 12%[85].

When lysozyme was placed in (ChCl:U) (1:2) and (ChCl:Gly) (1:2) DESs, its fluorescence emission spectra showed a small blue shift and a narrower spectra compared to a standard buffered solution. This shift in the fluorescence response indicates that the tryptophan side chains within lysozyme were experiencing a less polar and more uniform environment in the DESs, which suggests a more compact conformation for lysozyme within the DESs, with the tryptophan residues in a relatively constrained and less exposed manner compared to the standard solution. At room temperature, the far-UV CD spectra of lysozyme in buffered solutions, (ChCl:U) and (ChCl:Gly) were similar, suggesting minimal impact on the protein's secondary structure under these conditions[106]. Similarly, at lower DES concentrations (up to 30% volume/volume), bromelain takes on a more compact structural conformation. However, as DES concentrations increase, bromelain tends to adopt a somewhat elongated structure[107].

As the temperature increases, the intrinsic fluorescence characteristics of lysozyme change to broader and red-shifted spectra due to the increasing exposure of tryptophan residues to the solvent — a consequence of the unfolding processes happening in response to elevated temperatures. Folding studies of lysozyme in the buffered solution aligned with the established two-state lysozyme unfolding, where both the tertiary and secondary structures are disrupted simultaneously. When cooled in a buffer, lysozyme regained its original tertiary structure. In contrast with the behavior in aqueous buffered solutions, the mean fluorescence energy in (ChCl:U) DES exhibited a nearly linear decrease from 293.15 K to 358.15 K suggesting a departure from the two-state unfolding process observed in aqueous solutions. Thus, in both DESs, lysozyme denatured through folding intermediates rather than an all-or-none transition seen in aqueous solutions. Upon cooling, the unfolding process was not fully reversible and the urea-based DESs caused greater destabilization of the protein's structure under thermal conditions. In contrast, when the eutectic mixtures were diluted with water, the denaturation process became reversible and proceeded in two stages. Lysozyme's activity was also impacted in both concentrated and neat (ChCl:Gly) DES, but its activity recovered with increasing dilution in water and was fully restored after removing the DESs[106].

In other cases, DESs can, instead, increase the unfolding temperature of proteins. This means that the proteins may remain stable at higher temperatures when immersed in (ChCl:Gly). A Trp-cage mini-protein was shown to remain stable at considerably higher temperatures in the DES solvent compared to a water medium. At 400 K, the protein denatures in a water medium, while it still retains its native structure in the DES. However, at 450 K, the enhanced diffusion of (ChCl:Gly) causes distortions in the stable interactions between the Trp-cage mini-protein. As a result, the protein's stable folded structure becomes compromised, leading to the unfolding of the protein. Therefore, it seems that DESs' slower dynamics and perhaps enhanced viscosity may play a role in protein stabilization at high temperatures[108]. The same DES led to an enhancement in the thermodynamic stability of RNase A, surpassing its stability in a purely aqueous environment[109].

At high temperatures, NADESs lead to HRP aggregates, a phenomenon not observed in the control PBS buffer and that can hinder enzyme activity[85]. NADESs led to an approximately 60% increase in enzymatic activity of HRP at 310.15 K compared to control buffer. (Bet:Sor:W) caused a two-fold increase in enzymatic activity compared to the control buffer. HRP follows a denaturation model where an intermediate state is observed before full unfolding. The increase in enzymatic activity is justified by a significant reduction of the temperature at which the protein starts to undergo structural changes that eventually lead to unfolding in the presence of (Bet:Sor:Water) and (Bet:Suc:Pro:Water) suggesting that NADESs might prompt the HRP intermediate state along with secondary structure alterations that lead to a gradual unfolding process, during which the enzyme shows increased activity, extending beyond the neat buffer control. The exposed distal heme pocket forms hydrogen bond-like interactions potentially boosting enzymatic activity[85]. Notably, bromelain also maintains a significant portion of its enzymatic activity within the DES, and in some instances, its activity even surpasses that of its native state. The fluctuation time around the bromelain's active site increases gradually with higher DESs concentrations, particularly beyond 30% volume/volume - when its structure is more elongated[107].

Wahlgren and co-workers[110] assessed the potential of (ChCl:Gly) (a residual amount of water, 0.58 wt%, was found after incorporation of the protein), in storing lysozyme, showing that the protein remained stable even after 40 days of storage at room temperature. The enzyme retained its activity when placed in an aqueous environment either by transferring from the DES to an aqueous buffer (reconstituted) or by increasing the water content within the DES (hydration). The inclusion of water in the DES was found to drastically enhance a lipase's activity. When the DES was used alone, the conversion rates were extremely low, below 2%. However, when the DES was mixed with water in binary combinations, the reactions exhibited near-complete conversions[111]. And while anhydrous

ChCl:Propylene glycol tended to deactivate β-glucosidase, the addition of water counteracted these adverse effects[112].

The relationship between hydration and protein structure seems to be non-monotonic[113]: as water content in the solvent increases, one might expect the protein's conformational changes to follow a consistent pattern, such as a gradual and continuous shift towards a more native-like state. The non-monotonic behavior suggests that there are distinct points or regimes of hydration where the protein's structure undergoes particular changes that are not linearly connected.

The non-monotonic behavior can be broken down into different hydration regimes: at low hydration levels, typically below around 10 wt % water in a 1:2 ratio of (ChCl:Gly), water molecules intermingle with the DES network, displacing chloride anions (Cl^-) in the process. This new arrangement of the solvent tends to interact more extensively with proteins through hydrogen bonds and electrostatic interactions. This influences the bovine serum albumin's (BSA) electrostatic environment, ultimately leading to further loss of folding which leads to a more pronounced exposure of hydrophobic residues, driving the formation of transient oligomers through attractive interactions. There is a reduction in the structural patterns found within the secondary structure coupled with an increase in unordered structure. But while the protein changes conformation, it maintains a certain level of globularity in the DES as compared to the aqueous buffer; at 10 to 40 wt % hydration, water molecules take on the role of dissociating the DES components into smaller clusters while filling the gaps within the structure. The presence of water leads to the gradual restoration of an ordered secondary structure, accompanied by a decrease in unordered structure; when hydration is beyond approximately 40 wt %, the DES components fully dissociate, diffusing freely. Consequently, the influence of the DES on protein behavior diminishes, and water primarily takes upon the role of solvating the proteins – a shift towards preferential solvation. The introduction of water facilitates conformational shifts in the protein and the native secondary structure is largely restored.

The thermal denaturation process at low hydration levels adheres to a two-state unfolding mechanism. At high DES hydration levels (> 36.5 wt % H_2O) and in aqueous buffer (100% H_2O), BSA exhibited a non-two-state transition that suggests the involvement of intermediate states or protein aggregation during the unfolding process.

DESs showed the capability to protect BSA against thermal unfolding and the transition temperature at which BSA undergoes thermal denaturation is higher when in pure (ChCl:Gly) (neat solvent) and lower when in an aqueous buffer. An increase in the half-denaturation temperature was found, allowing it to withstand higher temperatures before denaturation. Additionally, the energy required to unfold the protein, (*i.e.*, the free energy of denaturation) was higher in BSA solvated in hydrated DESs compared to the protein solvated in aqueous buffer. Initially, as the hydration levels increase from low to moderate, the free energy of denaturation increases meaning that the protein becomes more stable as hydration increases, particularly within the range of 0.37 to 10.3 wt % H_2O. This behavior is consistent with the protein adopting a more folded and stable structure as water content rises. However, as hydration continues to increase beyond this moderate range, in particular at high hydration levels (above 36.5 wt % H_2O), the variation in free energy of denaturation becomes non-monotonic: a higher free energy of denaturation is found in the DES with 36.5 wt % H_2O compared to the DES with 53.4 wt % H_2O. Thus, the protein's stability does not consistently increase with hydration, as could be expected. This non-monotonic behavior indicates a non-monotonic relationship between hydration and stability underscoring the complex interplay between hydration, solvent composition, and protein dynamics/stability.

Regarding protein stability in the NADESs studied here, (Bet:Gly) (1:2), an enhanced enzymatic activity of CALB was found, whereas betaine-xylitol (Bet:Xyl) led to a reduction, suggesting that the presence of Gly in the (Bet:Gly) system contributes to the stability of the enzyme. It is worth mentioning that the viscosity of (Bet:Xyl) was reported to be 11504±5 mPas, 10 times higher than that

of (Bet:Gly). The secondary structure appeared to undergo minimal alterations, as evidenced by CALB's secondary structure remaining predominantly unaffected in the presence of (Bet:Gly)[114].

Among several betaine-based DESs, the utmost activity of laccase was observed in a 20% (v/v) solution of (Bet:Gly) (1:2) DES. Specifically, when stored at a temperature of 4°C, the presence of Bet and Gly had a remarkable impact on enhancing the enzyme's stability as it retained over 6.5 times more of its original activity compared to when it was stored in a typical aqueous buffer solution. In contrast, ChCl-based DESs led to a decrease in enzymatic activity. The stability of laccase in (Bet:Gly) was also higher at elevated temperatures (80°C and 90°C) compared to aqueous solutions of the DES components[115].

(Bet:Gly) (1:2) improved enzyme stability across a range of temperatures, including -20°C, 4°C, and 37°C, when compared to a conventional buffer solution. Although there are various differences between the properties of an aqueous buffer and DESs, one particular aspect — namely, the influence of solvent viscosity — was not assessed in this study[116].

The molecular mechanism responsible for the observed increase in enzymatic activity and thermal stability within the (Bet:Gly) DES remains elusive. The study of protein stability in DESs through MD simulations has the potential to provide foundational insights into the influence of water and the thermodynamic and kinetic intricacies associated with the folding/unfolding and structural phenomena reported in experimental studies.

In order to bridge the gap between practical applications and a fundamental understanding on the effect of the water content and high temperatures in the structure of a representative globular protein, ubiquitin was studied herein through MD simulations in (Bet:Gly:Water) (1:2:ζ; $\zeta = 0, 1, 2, 5, 10$) DESs.

4.5 METHODS

Ubiquitin was chosen here as a prototypical system for investigating protein stability in a DES primarily due to its small size. Moreover, this protein has been extensively studied for playing an important role in protein degradation pathways and cellular signaling. A DES comprising Bet (HBA) and Gly (HBD) in a molar ratio of 1:2 was chosen for this study. The reasons for the selection of this DES are twofold: the availability of experimental values of density and viscosity and the fact that betaine-based DES are currently being used as a model systems at FCUL and NOVA, concerning biomolecular stability.

Ubiquitin was studied in a (Bet:Gly) DES in anhydrous and aqueous environments at 298 K and 0.1 MPa. The following systems were studied (Bet:Gly:Wat) (1:2:ζ; ζ = 0, 1, 2, 5, and 10) corresponding to the following water molar percentages (mol %) 25, 40, 62.5, 76.9, and weight percentages (wt %), 5.6, 10.7, 23.0, and 37.4. The AMBER99SB force field was used to model ubiquitin, whereas DES was modeled with the GAFF-opt (*i.e.*, $\lambda_Q = 0.92$ and $\lambda_\sigma = 1.03$) force field, previously discussed, and water was described by the TIP4P-Ew model.

The initial conformation of ubiquitin was obtained from the crystallographic structure of human erythrocytic ubiquitin refined at a resolution of 1.8 Å, available in the Protein Data Bank (PDB name: 1UBQ[38]). The crystal structure description emphasizes the compact and tightly hydrogen-bonded nature of ubiquitin, with approximately 87% of the polypeptide chain involved in hydrogen-bonded secondary structure.

The structure exhibits a three and one-half turns of α-helix, a short 3_{10}-helix segment, a mixed β-sheet comprising five strands, and seven reverse turns. Additionally, a hydrophobic core is formed between the β-sheet and α-helix.

The protein was solvated by 450 molecules of Bet and 900 molecules of Gly for the (Bet:Gly:Wat) (1:2:0) system in a cubic box with PBCs. The aqueous systems (Bet:Gly:Wat) (1:2:ζ) with ζ = 1, 2, 5, and 10, contained, respectively ζ×450, water molecules.

Following energy minimization of the system using the steepest-descent algorithm the systems were equilibrated in the *NVT* ensemble, for 100 ps. The protein was restrained by using harmonic restraints, during this short simulation and, therefore, only the solvent relaxed. This was followed by another equilibration period (100 ns) in the isothermal-isobaric (*NPT*) ensemble.

Upon completing the NVT and NPT equilibration phases, the production trajectories were propagated in the *NPT* ensemble for 500 ns/replica (five replicas). The temperature was controlled via the Bussi *et al.*[33] thermostat whereas the Parrinello-Rahman barostat[36] was employed to maintain a constant pressure.

The electrostatic interactions were computed with the PME method[32]. This technique combines real-space and Fourier-space calculations to accurately represent long-range electrostatic effects. A cutoff radius of 1 nanometer was applied, beyond which non-bonded van der Waals and real space part of the electrostatics interactions, were neglected. The LINCS algorithm was invoked to constrain the heavy atoms-hydrogen motions.

To explore the thermal stability of UBQ both in water and the DES, some simulations were also carried out at high temperatures (373 K, 410 K, 425 K, and 450 K) and 0.1 MPa. Above the boiling point of water simulations in neat water were performed under pressurized conditions at which real water remains liquid; simulations at high temperatures and 0.1 MPa were also carried out to assess the effect of the pressure. The chosen temperature-pressure combinations were 373 K and 0.1 MPa, 410 K, and 425 K at 0.5 MPa, and 450 K at 1 MPa. While the MD simulations of UBQ in the DES were carried out at high temperatures and 0.1 MPa, some simulations were also performed at high pressures to assess the effect of pressure. The trajectories were propagated for 1.9 μs followed by an initial equilibration period of 100 ns. The equations of motion were integrated using the Verlet leap-frog algorithm, with a time step of 1 fs for the DES systems and 2 fs for the neat water systems. Additionally, simulations of UBQ in water were conducted with a 1 fs time step (replica 2) at all temperatures to ascertain any potential time-step dependence of protein stability.

4.6 RESULTS AND DISCUSSION

4.6.1 Role of Water and Viscosity on Ubiquitin Stability

The R_g and the secondary structure of UBQ in anhydrous and hydrated (Bet:Gly) as well as in water at 298 K and 0.1 MPa were analyzed (**fig. 4.1)**. A narrower R_g distribution for UBQ is observed in (Bet:Gly) (1:2) relative to water, which suggests that UBQ adopts more compact conformations in the DES environment compared to water. However, upon adding water to the DES, the R_g distribution starts to broaden indicating the protein adopts a wider range of conformations as the water content increases. Interestingly, there is a non-monotonic shift of the main peak. At ζ = 5 the protein's R_g distribution becomes more spread out and at the highest water molar ratio investigated (ζ = 10), the R_g distribution becomes more similar to that observed in pure water.

The non-monotonic behavior of the R_g is seemingly consistent with the results reported by Sanchez-Fernandez *et al.*[113] where protein structures in a DESs containing ChCl and either glycerol or urea undergo non-monotonic changes with the hydration content.

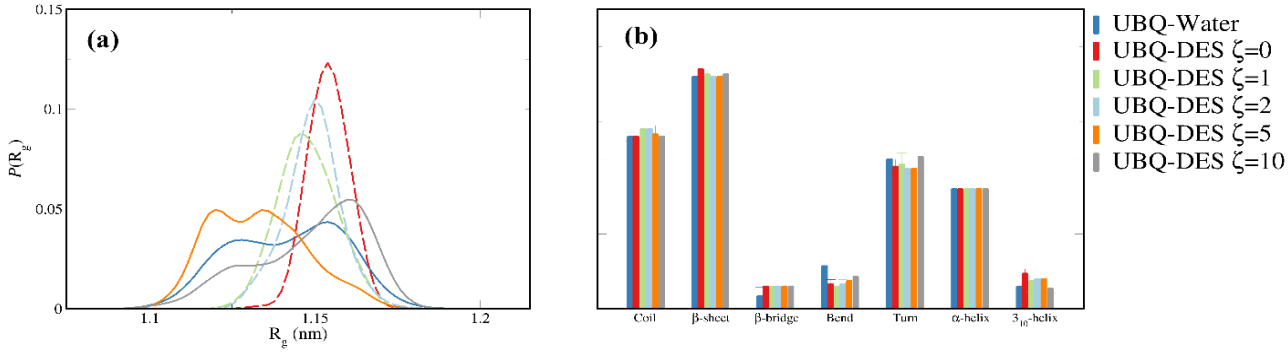

Figure 4.1. Radius of gyration distribution and secondary structure. *(a) distribution of the radius of gyration; (b) secondary structure of ubiquitin is compared across different hydration levels within the DES and in water.*

The percentage of secondary structures, specifically α-helices and β-sheets, in UBQ is nearly identical in both water and the DESs (ζ = 0, 1, 2, 5, and 10). The secondary structure content measured is approximately 16% α-helix and around 31% β-sheet. These values closely align with those determined through crystallographic studies[117]. Thus, despite variations in the R_g distribution, the secondary structure remains unaffected which implies that the structural arrangement of the protein's backbone is stable and does not change significantly in response to (Bet:Gly). To understand how water affects the protein dynamics in the DES environment, the fraction of water molecules in the DES, specifically in close proximity to the protein – so-called "biological" or bound water – was quantified. The biological water population was defined as water molecules located within 5.5 Å of any heavy atom (non-hydrogen atom) of the protein. This distance cutoff, although somewhat arbitrary encloses most water molecules that have a direct influence on the protein's local environment encompassing the coordination sphere of most amino acids.

When water is added to the DES, water molecules start forming a hydration layer around the protein. However, even at ζ =10, this hydration layer is relatively small compared to the total amount of water present in solution. Specifically, the hydration layer around UBQ is formed by less than half of the water molecules that would surround the protein in pure water (approximately 600 molecules of water) meaning that a significant portion of the water (> 75%) remains "trapped" in the DES rather than preferentially interacting with UBQ's surface (**figure 4.2**). These results suggest that (Bet:Gly) creates an environment where water is largely excluded from the protein's surface which contrasts with the behavior reported for aqueous solutions of osmolytes where water molecules seem to exhibit preferential hydration around proteins[70,118–120].

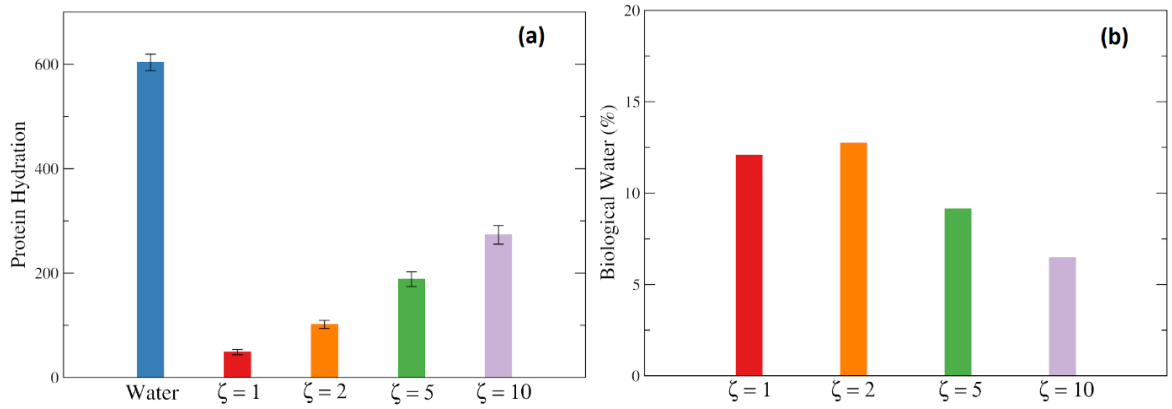

Figure 4.2. Hydration and percentage of biological water in UBQ's hydration layer. *(a) Absolute number of water molecules within the protein's hydration layer. Biological water is defined as water molecules within a radial distance of < 5.5 Å from any heavy atom, which typically includes the first hydration layer of amino acid side chains; (b) percentage of biological water in relation to the total water content is depicted.*

The addition of water to (Bet:Gly) reduces its overall viscosity making it more comparable to conventional solvents like water or other solutions commonly used in protein folding studies (η at ζ = 5 is 26 mPas and η at ζ = 10 is 7.3 mPas). As a consequence of the lower viscosity due to the addition of water, α-fluctuations in proteins become more pronounced. However, the addition of water to the DES does not (necessarily) uniformly favor the dynamics of all parts of the protein. So, the effect of adding water on the protein's behavior is not necessarily the same for all regions of the protein. β-fluctuations occur predominantly at regions exposed to the surrounding solvent and they involve smaller-scale motions within those solvent-exposed regions. In conventional solvents, it is believed that a complete and homogeneous hydration shell readily forms around the protein. This hydration shell plays a key role in influencing the dynamics and behavior of the solvent-exposed segments of proteins. However, in the DES, a complete and well-defined hydration shell does not form upon water addition, possibly affecting the dynamics of the protein beyond the α-fluctuations associated with the viscosity.

To probe the protein dynamics, we calculated the torsional dynamics of the protein, using **eq. 2.17**. Protein torsions can be viewed as fundamental units of motion that contribute to the overall folding and unfolding processes. By analyzing the time-correlation functions of the rotational movements around the backbone bonds N-Cα (dihedral angles phi, Φ) and Cα-C (dihedral angles psi, Ψ) in both water and (Bet:Gly:ζ), we aimed to understand how the presence of water affects the torsional dynamics of UBQ, in particular, the α-helix (amino acids 23 to 33) of UBQ. The choice of the α-helix is because our results indicated (see **section 4.6.2**, **fig. 4.7** upper panel) that the initial stages of unfolding initiated from this segment of the protein.

The time-correlation functions for the torsional dynamics around the Ψ dihedral angle of UBQ's α-helix indicate that the torsional dynamics undergo a significant slowdown in the DES compared to water (**fig 4.3**). This slowdown in the torsional movements of Ψ is evident when ζ values are low. However, increasing the water content in the DES restores the torsional movements of Ψ to a more dynamic state, similar to what is observed in water. The same trend is observed for the time-correlation function for torsional dynamics around the Φ dihedral angle (**Appendix A fig. A.2)**.

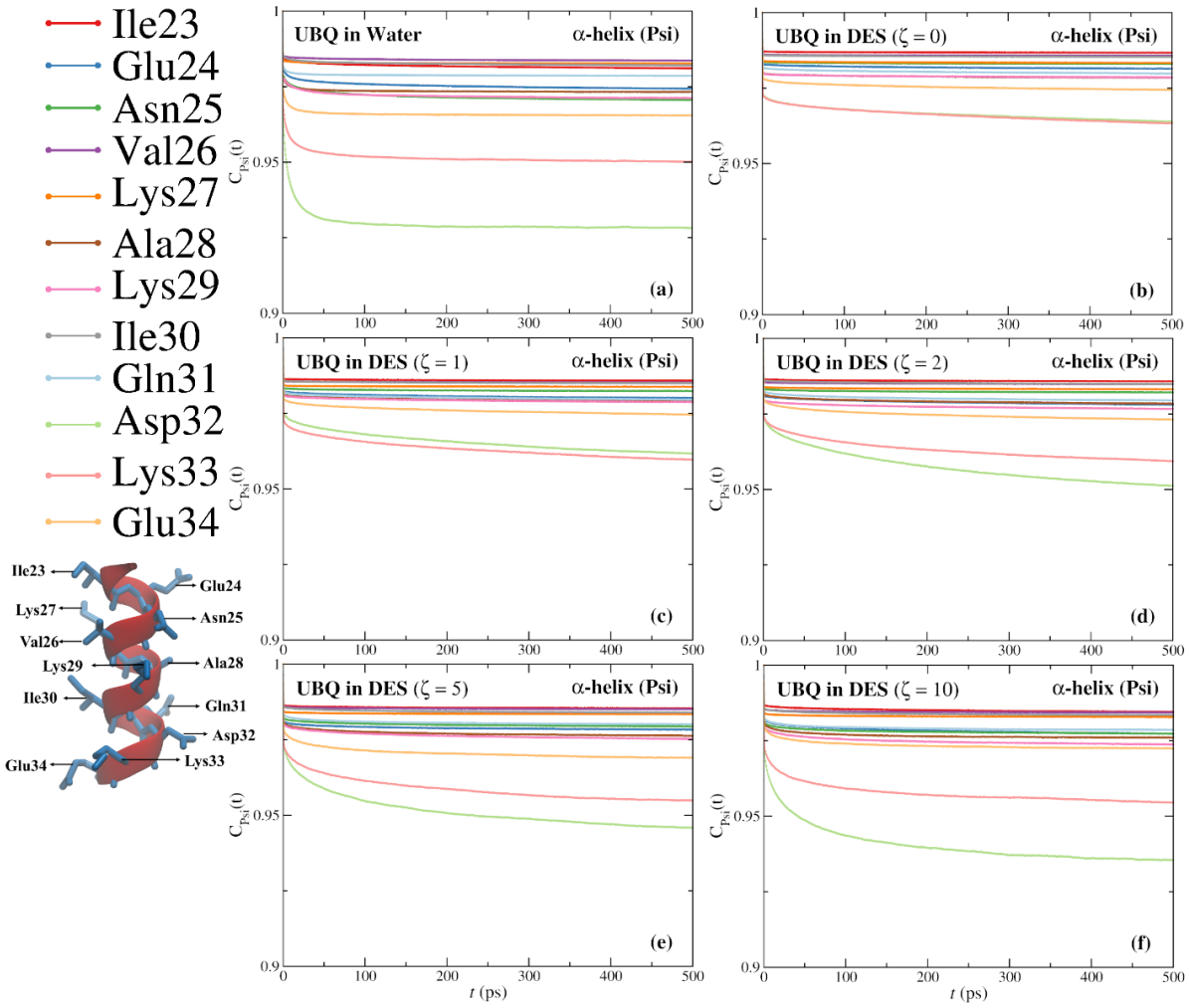

Figure 4.3. Torsional dynamics of UBQ α-helix in water and (Bet:Gly). *Torsional dynamics time correlation functions for the psi angles of the α-helix (amino acids 23-33) in UBQ in pure water and UBQ in (Bet:Gly) with varying water contents. The simulations were conducted at 298 K and 0.1 MPa.*

Fig. 4.3 also indicates that the addition of water results in non-uniform effects on the α-helix's backbone torsions with distinct amino acids showing distinct responses. For some amino acids, the torsional dynamics shows a monotonic increase with the solvent viscosity decrease, whereas for others this variation is non-monotonic. This indicates that local hydration, in addition to the decrease of the viscosity (a collective property) plays an important role. To assess the hydration level of UBQ's α-helix, the coordination number (*i.e.*, number of water molecules) in the first hydration layer of each C_α were calculated by integrating their respective RDFs up to the first minimum, (**fig. 4.4 (a)**). As can be seen the hydration of the backbone does not vary monotonically for every amino acid with the changes in the water content, (*e.g.*, Glu24, Lys27). Hydration numbers around the backbone atoms (C_α, C, and N) up to 5.5 Å were also computed for comparison purposes. A similar conclusion can be drawn (**fig. 4.4 b-d)**.

When considering the role of water on the protein dynamics both the number of water molecules and their dynamics is important. The dynamics of water molecules will be affected by their local environment. Thus, the local density of water molecules, and their interactions with other water molecules, the DES, and the protein, will affect their translational and rotational dynamics. This, in turn, should reflect in the protein dynamics.

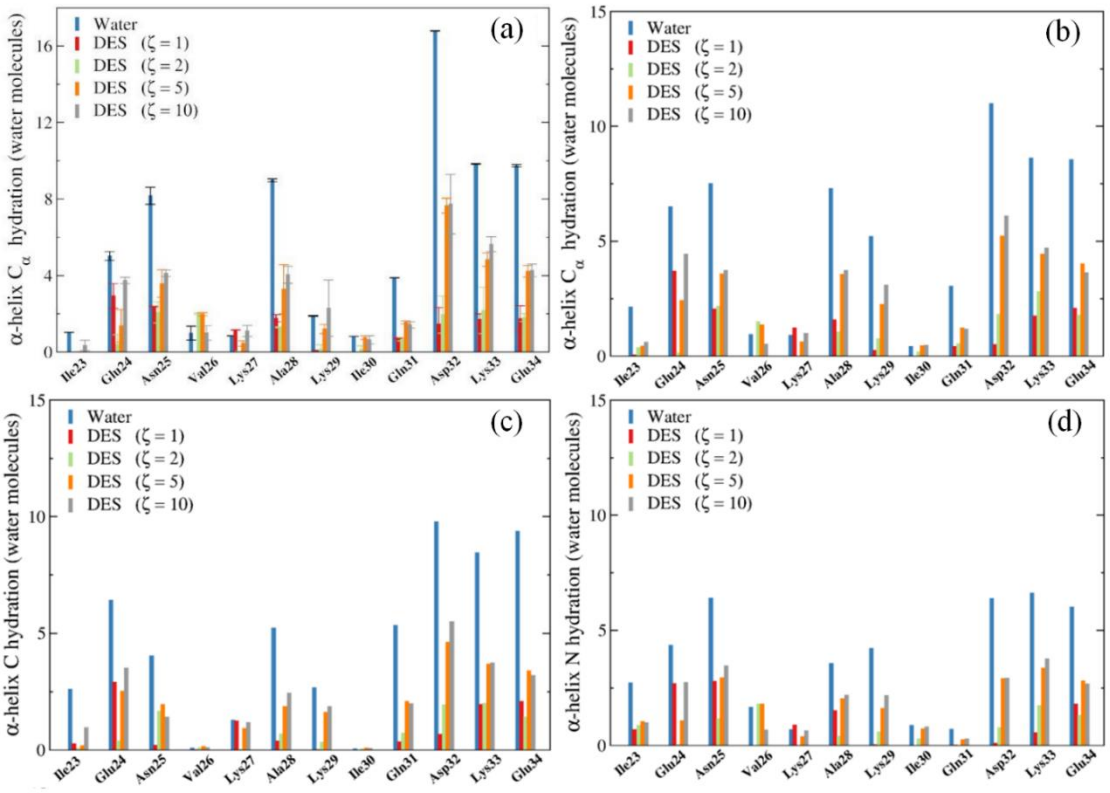

Figure 4.4. Water coordination around the (a) C_α first coordination sphere of UBQ's α-helix and within 5.5 Å of UBQ α-helix backbone atoms: (b) C_α, (c) C, and (d) N.

Hence, we now analyze the water dynamics of water molecules next to the α-helix. The dynamics of water was probed by calculating the orientational dynamics of water molecules (eq. 2.18) in the first hydration shell of the C_α of UBQ's α-helix, in neat water and in the different DES (**fig. 4.5**).

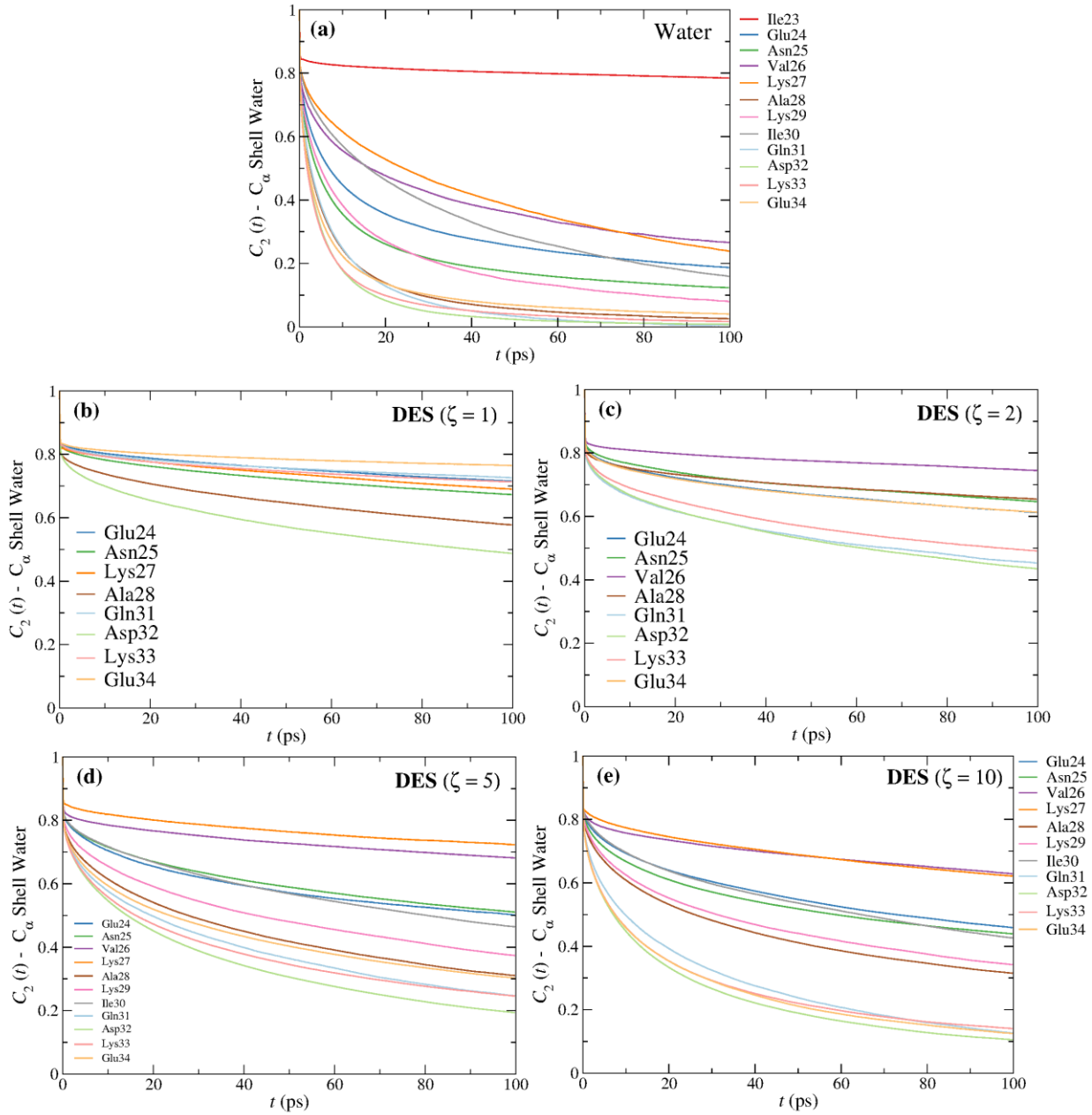

Figure 4.5. Orientational time correlation functions of water molecules in the first hydration shell of the Cα of each amino acid from UBQ's α- helix in (a) water and in the (b-e) different hydrated DES.

As can be seen the orientational dynamics of water near the α-helix is neither uniform nor monotonic with the water content for all amino acids. Water molecules next to some amino acids, such as Asp32, Lys33, or Glu34, exhibit a much faster orientational dynamics compared to others.

For Ile23, the torsional dynamics is especially slow, even in water, consistent with its low hydration and the slow torsional dynamics of this amino acid (see **fig. 4.3**). Furthermore, this amino acid is only residually hydrated in the DESs (see **fig. 4.4**) precluding the calculation of the orientational dynamics of water. The relatively fast orientational dynamics of water near Ile30 in water might seem contradictory to the slower dynamics of Ile23 since both depict a low hydration number. Ile30 has less than one water molecule in its hydration shell (approximately 0.8 water molecules on average). Moreover, this single water molecule is located at a considerable distance from the Cα of Ile30. One possible explanation for the relatively fast orientational dynamics near Ile30 is that this water molecule

might share the hydration shell with its nearest neighbors, specifically Lys29 and Gln31 for which a faster orientational dynamics is found.

These results support a close relationship between the orientational dynamics of water and the torsional dynamics of the protein. This, in turn, indicates that both the viscosity and protein-water coupled dynamics influence UBQ's conformational stability.

To quantitatively assess the difference in the torsional dynamics between UBQ's α-helix in water and the DES, the dihedral time correlation function of Asp32 and Glu24 were fitted to a two-term relation of the form:

$$C(t) = a + be^{-\frac{t}{\tau}} \quad \textbf{(4.3)}$$

where τ is the dihedral relaxation time (**fig. 4.6 a-b**). These amino acids display a monotonic and non-monotonic variation, respectively, of the hydration number with the water content in the DES (see **fig. 4.4**). A monotonic variation of the orientational dynamics can, however, be seen next to both amino acids (**fig. 4.6 c-d)**.

The torsional dynamics of Asp32 shows a monotonic variation with the solvent's viscosity characterized by a power law relationship with a fractional exponent of 0.31 (**fig. 4.6**). In contrast, the variation of the torsional dynamics of Glu24 with the viscosity, is non- monotonic.

The relationship between the water content and protein refolding remains a subject of ongoing research and investigation: there have been experimental reports where the amount of water in the solvent is inversely correlated with a protein's ability to refold[103]. However, the underlying reason for this observed behavior is not fully understood.

In the context of "protein slaving", our results indicate that the torsional dynamics of UBQ in a DES depend on both the solvent viscosity and the coupled dynamics between the protein and its solvation shell.

The "solvent slaving" mechanism provides as explanation on how the solvent "enslaves" the protein's large-scale motions and limits its conformational substates. However, the protein's potential energy surface dependence of the solvent (thermodynamic consideration) is not considered. Thus, different solvents, such as water and DES, involve distinct protein-solvent interactions, possibly altering the thermodynamic equilibrium between the folded and unfolded states.

Thus, while the solvent slaving mechanism provides insight into the kinetics of protein dynamics and how solvent fluctuations influence the conformational changes, it does not address how the equilibrium between the F-U states are influenced by the solvent properties.

The studied NADES's, (Bet:Gly), ability to preserve UBQ's overall structure comes at the cost of significantly reducing its conformational dynamics. This loss of dynamics can be critical for certain proteins, such as enzymes, that rely on their dynamic nature to efficiently bind to substrates. When proteins, in general, lose their conformational dynamics, they might become less effective at performing their biological functions. Our study suggests that (Bet:Gly) can "freeze" or restrict the protein's movements. However, upon the addition of water to the DES, the protein's dynamics is restored, which may lead to the recovery of the protein's normal function.

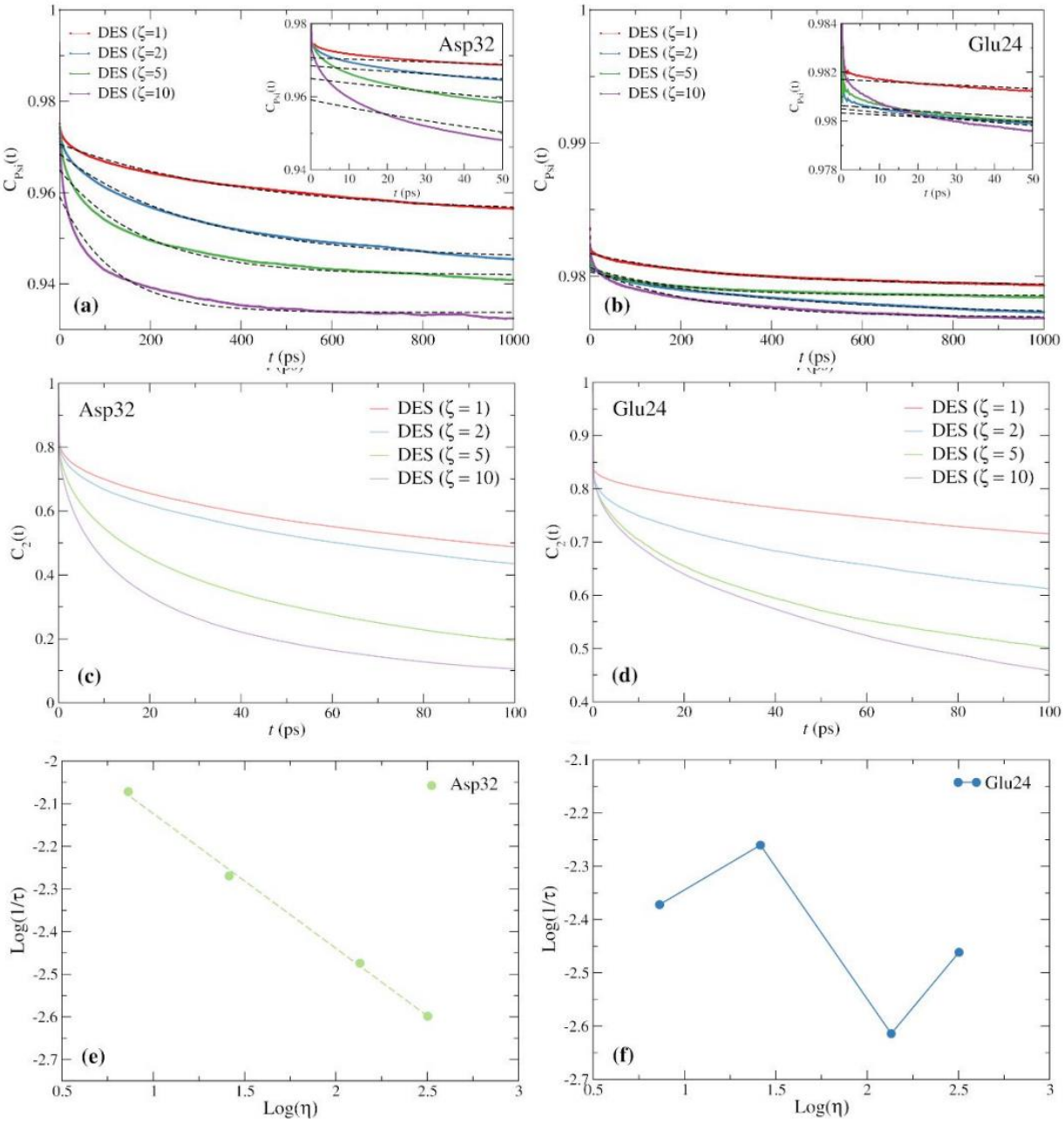

Figure 4.6. Torsional dynamics of (a) Asp32 and (b) Glu24 with dashed lines representing fits to equation (4.4); Orientational dynamics of water molecules in the Cα hydration shell of (c) Asp32 and (d) Glu24; (e) The logarithm of the inverse of the torsional relaxation time as a function of viscosity for Asp32 exhibits a power law dependence of the viscosity, $1/\tau = A\eta^{-\gamma}$, with an exponent γ = 0.31, where the dashed line indicates a linear fit. (f) Glu24 exhibits a non-monotonic dependence on viscosity.

4.6.2 Thermal Stability of UBQ: Insights from High-Temperature MD Simulations

UBQ was further studied in water and the anhydrous DESs at high temperatures and pressures. The data suggests that in water, within the timeframe of the simulations, UBQ starts to lose its structural stability at a temperature around 373 K, consistent with a previous computational study that predicted the melting temperature of UBQ to be ~ 372 K[121]. Both of these values are close to the experimental melting temperature of approximately 390 K, reported by Wintrode *et al.*[122].To assess the thermal

stability, several structural parameters (RMSD and percentage of α-helix and β-sheet) of UBQ were analyzed at varying temperatures from 373 K to 450 K. The maximum temperature of 450 K was chosen based on the unexpected observation that UBQ's structure remained stable and seemingly did not experience significant unfolding events in (Bet:Gly) within approximately 2 microseconds at temperatures below 450 K.

In **fig. 4.7**, the RMSD of UBQ in water and in (Bet:Gly) is presented for two different replicas. The second replica (R2) of UBQ in water was performed with a shorter time-step of 1 fs, while the first replica (R1) was performed with a time-step of 2 fs. The results show that at lower temperatures, UBQ appears to be more stable in the second replica (Δt = 1 fs). However, at higher temperatures (425 K and 450 K), there is no significant difference in stability between the two replicas, suggesting that the simulation time-step does not strongly influence the overall results on the stability of the protein at these temperatures. A similar behavior was observed for other structural properties, such as the R_g and SASA of UBQ. Additionally, the effect of pressure on the water systems was investigated, ruling out any significant impact. The last configuration of UBQ in these MDs is also displayed in **fig. 4.7**.

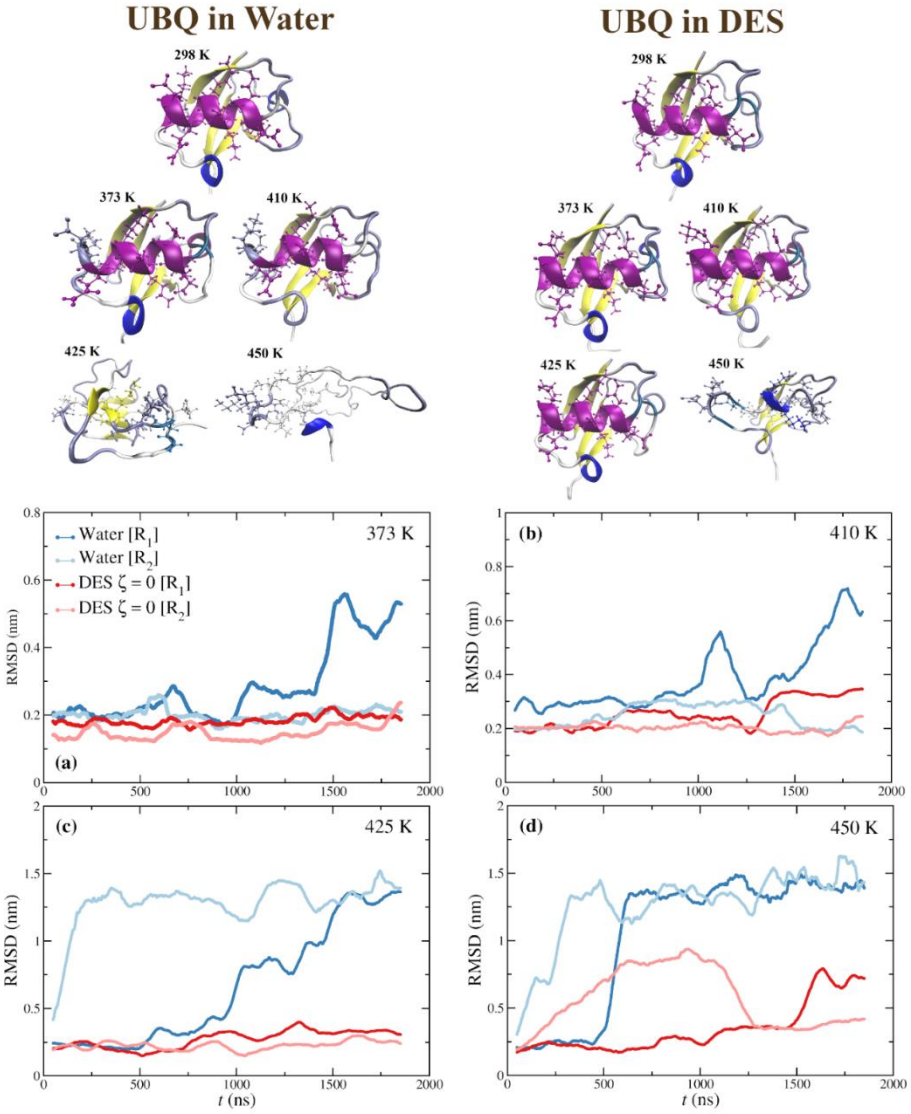

Figure 4.7. UBQ conformations in water and (Bet:Gly) at increasing temperatures and RMSD of UBQ's backbone in water and (Bet:Gly) at different temperatures. Top: *Final conformations UBQ obtained from 1.9 μs MD simulations under various temperature conditions. Bottom: RMSD of UBQ backbone atoms relative to its crystal structure at four different temperatures (373 K, 410 K, 425 K, 450 K). To provide a clearer view of the data, moving averages were calculated using a 100 ns window.*

In water, fluctuations of the α-helix are observed to start at 373 K, indicating that the α-helix begins to lose its stability. However, these fluctuations are reversible, meaning that the α-helix can still recover its original conformation. In the DES, the α-helix exhibits lower fluctuations at all temperatures. However, at high temperatures, the fluctuations increase significantly, making it challenging to draw conclusions regarding the thermal stability differences between the two solvents. In contrast, the fluctuations of the β-sheet secondary structure are less ambiguous and easier to interpret: (Bet:Gly) shows a higher preservation of the β-sheet structure at every temperature, suggesting that the β-sheet is more stable in the DES environment compared to water (**fig. 4.8**).

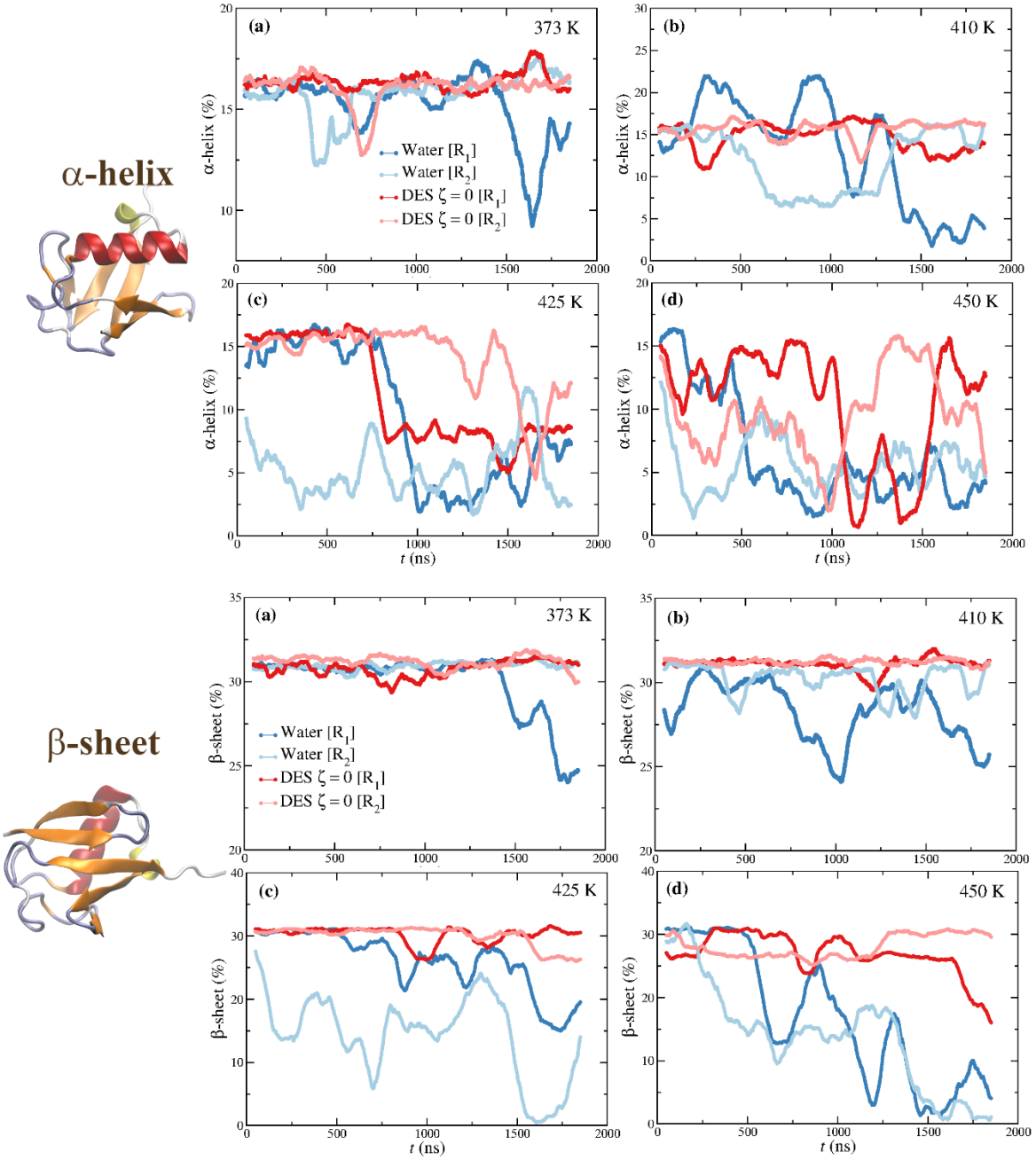

Figure 4.8. α-helix and β-sheet percentage of UBQ in water and DES at different temperatures. *The upper panel shows the α-helix content, while the lower panel displays the β-sheet content. To provide a clearer representation of the data, moving averages are calculated using a 100 ns window.*

Fig. 4.9 shows the dihedral time-correlation functions of the α-helix amino acids at different temperatures. The torsional dynamics is highly conserved in the DES even at high temperatures, meaning that, despite changes in the percentage of α-helix, the dihedral angles remain relatively stable and do not undergo significant fluctuations. In contrast, in water, the dihedral angles around the Cα-C bond and the N-Cα bond are much more labile. Therefore, in the DES, the rotations of these dihedral angles are significantly restricted or slowed down, even at very high temperatures. This "freezing" effect suggests that the protein's structure is better preserved in the DES.

At 298 K the values of the viscosity for the different water molar ratios, discussed in the previous section, are: $\eta = 318 \pm 5$ mPa.s for $\zeta = 1$; $\eta = 135 \pm 2$ mPa.s for $\zeta = 2$; $\eta = 26 \pm 0.5$ mPa.s for $\zeta = 5$; $\eta = 7 \pm 0.2$ mPa.s for $\zeta = 10$. η falls down relatively fast with temperature and the viscosity at high temperatures is: $\eta = 21 \pm 0.3$ mPa.s at 373 K; $\eta = 8 \pm 0.3$ mPa.s at 410 K; $\eta = 6 \pm 0.2$ mPa.s at 425 K; $\eta = 4 \pm 0.1$ mPa.s at 450 K. Nevertheless, the protein's torsional dynamics at these conditions are only slightly faster than those observed in the aqueous DES. These results point to the importance of water to the conformational dynamics of UBQ. Thus, UBQ remains relatively "frozen", even at high temperatures, and, therefore, much lower viscosities than at room temperature. These findings highlight the critical role of water-protein interactions in preserving the conformational dynamic of UBQ, on one hand, and the ability of the DES to "preserve" the protein even at very high temperatures when the UBQ completely unfolded in water.

The combined effect of steric hindrance and protein-solvent electrostatic interactions seem to contribute to the unique behavior of the protein in this dehydrated environment.

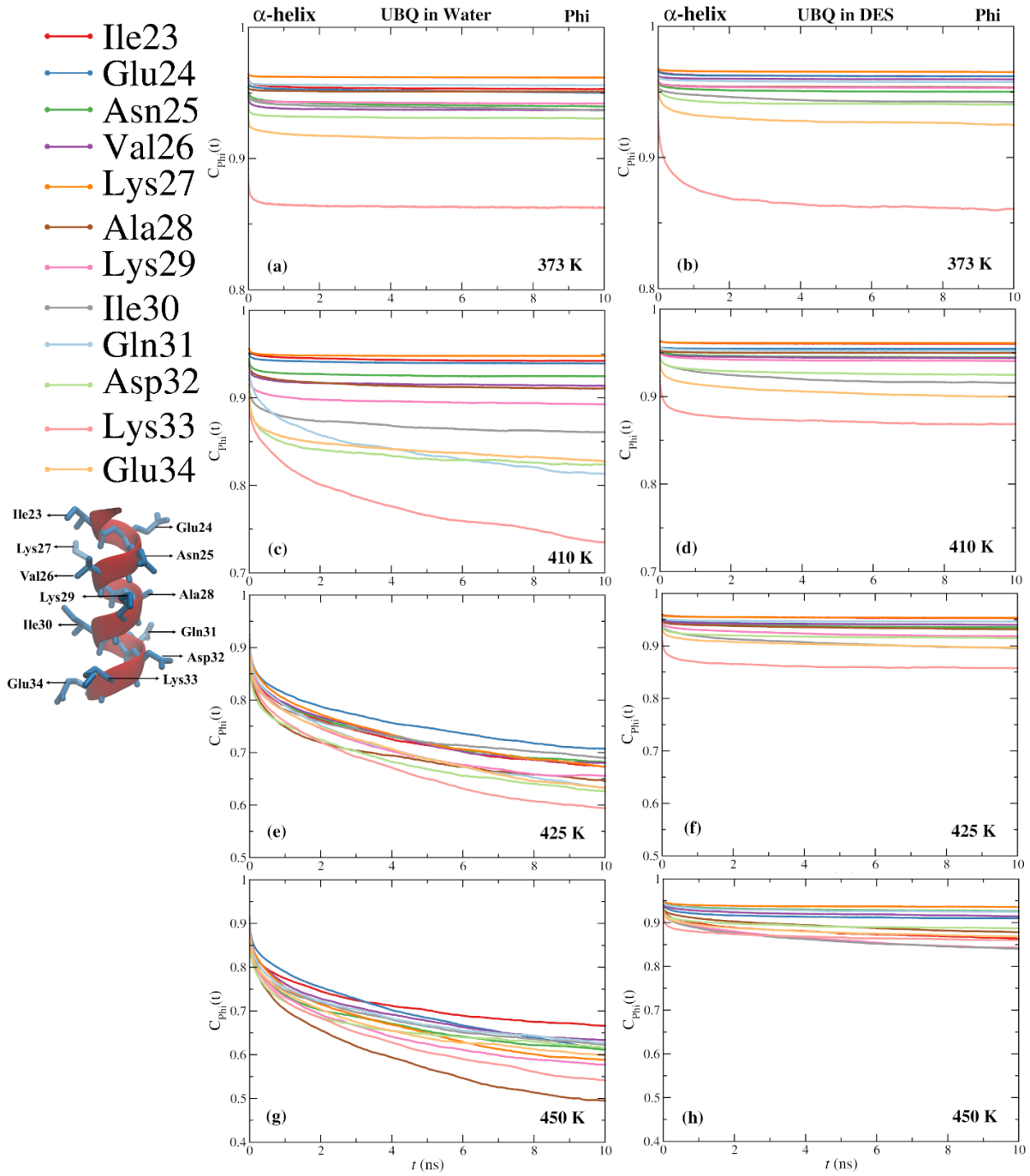

Figure 4.9. Torsional dynamics time correlation functions of UBQ's α-helix at high temperatures in water and (Bet:Gly). *Torsional dynamics time correlation functions for the psi angles of the α-helix segment (amino acids 22-34) in UBQ.*

4.7 CONCLUSION

Unlike the conventional preferential hydration mechanism or water entrapment theory, our findings suggest a novel and intricate kinetic explanation involving betaine and glycerol molecules not being excluded from the protein interface. Thus, instead, the DES seems to trap water molecules, preventing the formation of an extended hydration layer around the protein. This mechanism contributes to the stability of UBQ in aqueous DES solutions, presenting an intriguing departure from the established hypothesis for osmolytes-mediated protein stabilization. Under the slaving model, in turn, the protein's motions are influenced by the dynamic fluctuations of the surrounding solvent molecules. As the solvent molecules move and rearrange, they create a dynamic environment around the protein and proteins will, in turn, respond to these changes. For UBQ to undergo a significant conformational change, it must navigate through a series of small steps, each influenced by the instantaneous configuration of the solvent molecules. The slaving model proposes that large-scale motions in proteins occur through a series of small steps, like small-scale torsional motions, with the motion of each step being dictated by the fluctuations of the surrounding solvent. We found that the torsional dynamics of the backbone of the UBQ's α-helix was slowed down in the presence of (Bet:Gly) compared to water and that this slowdown can be attributed to the viscosity and dehydration next to the protein.

The enhanced thermal stability, also observed in this work, can be attributed to a comparable slowdown in the backbone torsional dynamics, suggesting that the DES environment influences the protein's dynamic response to temperature changes. Such insights have the potential to elucidate puzzling observations, such as non-monotonic protein folding behavior in DESs with varying water molar ratios and the source of the thermal stability of enzymes in DES.

CHAPTER 5

The Potential of Deep Eutectic Solvents as Next-Generation Cryoprotectants

5.1 CRYOPROTECTANT AGENTS

Cryopreservation is the preservation of biological material at extremely low temperatures. In the late 18th century, Lazzaro Spallanzani observed that sperm retained mobility even under cold temperature conditions[123]. This early discovery set the stage for exploring the preservation of both spermatozoa and red blood cells. However, due to the limited understanding of the cryopreservation process and the lack of sophisticated techniques, the success of preserving cells and tissues varied widely and scientists encountered difficulties in replicating successful outcomes; during the early stages of cryopreservation, the freezing and thawing lead to the formation of ice crystals that can damage cell structures and impair their viability. When cryopreserved reproductive cells were used for fertilization or implantation, early embryonic death frequently occurred, resulting in infertility and failed attempts at reproduction.

In the 1950s, James Lovelock proposed that the cryopreservation process caused osmotic stress in cells leading to the formation of ice crystals, explaining why some cells did not survive the freezing and thawing process. The application of cryopreservation to human materials began in 1954 – this year marked the first successful use of cryopreservation in human reproduction with three pregnancies resulting from the insemination of previously frozen sperm. This marked the first successful use of cryopreservation in human reproduction[124,125]. In 1948, C. Polge *et al.*, while working with semen collected from male fowl, froze it in a mixture that contained glycerol (instead of a fructose solution) due to a mistake in labeling. To their surprise they found that the glycerol solution allowed the fowl spermatozoa to survive freezing at 203.15 K[126].

Following this initial discovery of the effectiveness of glycerol in cryopreservation, subsequent developments have relied on the addition of cryoprotective agents to the cell media before freezing to protect the cells from the damage caused by ice crystal formation. When added to the cell media, glycerol effectively acts as a cryoprotectant, shielding cells from the damaging effects of rapid ice crystal growth. The key mechanism behind glycerol's cryoprotective action lies in its ability to reduce the freezing point of the cell media. This results in the formation of a "glass-like" state, called vitrification, which significantly reduces the ice crystal formation. Additionally, glycerol can penetrate the cell membranes due to its small molecular size and high permeability. Once inside the cells, glycerol acts as a cryoprotectant by replacing water, thus reducing the subsequent damage caused by ice crystal formation.

Dimethyl Sulfoxide (DMSO) is perhaps one of the most used cryoprotective agents in the field of cryopreservation. DMSO acts by increasing the porosity of cellular membranes and promoting vitrification of water. By making the membrane more porous, DMSO allows water molecules to move more freely through the membrane. Similar to glycerol, DMSO helps to prevent the formation of large ice crystals by increasing the concentration of solutes inside the cell. This increase in solute concentration causes vitrification, instead of crystallization. The nature and concentration of the cryoprotectant, as well as the temperature at which it is added, play a crucial role in preserving cell viability.

Typically, a concentration of 5% to 15% of cryoprotectant is sufficient to enable isolated cells to survive freezing and thawing from liquid nitrogen temperatures.

In general, cryoprotectants are substances that, when dissolved in water, disrupt the orderly arrangement of water molecules, lowering the freezing point of the solution below 273.15 K. Thus, cryoprotectants prevent ice from forming both inside and outside of cells when tissues or cells are exposed to extremely cold temperatures. Additionally, they tend to reduce the size of ice crystals. The preferential exclusion/preferential hydration theory proposes that some solutes, often used as cryoprotective agents, preferentially interact with water molecules rather than with biomolecules. As a result, cryoprotective agents like glycerol, sucrose, or betaine are excluded from the surface of

biomolecules, stabilizing their native conformation. However, some cryoprotectants have specific properties that make them toxic to cells. Whereas cryoprotectants are thought to disrupt water's hydrogen bonding network, precluding, or delaying the formation of nascent ice crystals, their interference with hydrogen bonding can sometimes lead to nonspecific toxic effects, *i.e.*, hydrogen bond disruption may not be limited to water molecules but can also affect other molecular structures, including biomolecules. Two other pictures, the water replacement and water entrapment hypotheses, have been proposed to explain how cryoprotectants interact with biomolecules[127,128]. According to the former, cryoprotectants replace water and interact with biomolecules through hydrogen bonding. The water entrapment hypothesis proposes that cryoprotectants trap water around biomolecules, preventing dehydration-induced conformational changes. However, recent research has suggested that during dehydration, water surrounding membrane phospholipids is removed - a process that is not prevented by cryoprotective agents[129]. This suggests that neither the replacement nor the entrapment of water might play a significant role in protecting membranes during freezing.

There are two main types of cryoprotectant based on their ability to penetrate cell membranes (**fig. 5.1**): (1) Nonpermeable cryoprotectants, such as sugars (*e.g.*, trehalose and sucrose), are unable to penetrate the cell membrane, remaining in the surrounding solution. These compounds act primarily by increasing the osmolarity of the extracellular space leading to cellular dehydration, reducing the risk of intracellular ice crystal formation. When the temperature drops during the cooling process, these cryoprotectants, along with the water in the extracellular solution, undergo a transition into a highly viscous solution. The increased viscosity of the vitrified extracellular solution hinders the movement of water molecules. The water molecules inside and outside the cells tend to move to areas of higher solute concentration through osmosis. However, the high viscosity of the extracellular solution effectively "traps" the water inside the cells. By keeping the water within the cells and preventing freezing, nonpermeable cryoprotectants help maintain the integrity of the cell membrane and the structures within the cell. (2) Permeable cryoprotectants, such as DMSO and glycerol, can penetrate the cells. These can cause an initial reduction of the cell volume by drawing water out of the cell. However, this is followed by an influx of water and cryoprotective agents until equilibrium is reached, with similar concentrations inside and outside the cell. Throughout this "hydration" phase an increase in cell volume is observed by replacing a significant portion of intracellular water with the cryoprotective agent, without causing excessive dehydration of the cell. These agents offer intracellular protection because they tend to stabilize the native state of biomolecules[129–132].

Glycerol can penetrate the cell membrane, where it interacts with the lipid bilayers, helping stabilizing the cell membrane structure and preventing the formation of damaging ice crystals inside the cell[133]. When added to the cell media at concentrations typically around 10%, DMSO can enhance the cell membrane permeability to water molecules, allowing water to flow more freely into and out of the cell[134].

When cells encounter stressors like heat, cold, oxidation, or desiccation, they respond by producing significant amounts of trehalose. Trehalose has been applied in several applications, including to protect proteins from denaturation, to stabilize vaccines, and safeguard bacterial cultures or cells. Trehalose can interfere with the formation of intermolecular disulfide bonds preventing proteins from aggregating when exposed to moisture, thereby preserving their quality and efficacy during storage. Trehalose has also demonstrated favorable properties in stabilizing IgG1 antibodies, recombinant botulinum serotype A vaccines during the lyophilization process, and has been used successfully in the cryopreservation of sperm and stem cells. Trehalose's exceptional efficacy lies in its ability to replace cellular water, thereby stabilizing and safeguarding cellular membranes and proteins during freezing processes. While cells can produce trehalose in response to stress, when externally added, it is typically considered a nonpermeating cryoprotectant. Trehalose alone is not highly effective as a cryoprotectant, primarily because it cannot easily enter cells. To enhance the cryoprotective

properties of trehalose, several strategies that aim to facilitate the delivery of trehalose into cells have been developed. One approach involves microinjection, which is a technique used to inject trehalose directly into cells. This method ensures that trehalose reaches the interior of the cells where it can protect cellular structures during freezing. Some studies have explored the use of mutant bacterial toxins to create pores or openings in cell membranes[135]. These pores can facilitate the entry of trehalose into cells. Another strategy involves genetic engineering to enable the internal synthesis of trehalose within cells. The precise mechanism of how trehalose stabilizes proteins is not completely understood. Trehalose is believed to stabilize proteins and membranes by interacting with their partially unfolded or denatured states, rather than the native, folded structures. This stabilization occurs through the displacement of the water molecules surrounding proteins and membranes. Unlike some other osmolytes that preferentially exclude themselves from the surface of biomolecules, trehalose is thought to operate by interacting directly with partially unfolded or denatured states of proteins and membranes. It is believed that trehalose molecules act as a physical barrier between different protein molecules, preventing them from interacting with each other. When there are enough trehalose molecules around each protein molecule, it reduces both the unfolding and aggregation propensity decreases, resulting in increased protein stability[73,136–138].

Betaine was found to be non-toxic and highly efficient in its cryoprotective capabilities. Furthermore, betaine demonstrated negligible cytotoxicity, even after prolonged exposure to cells. The underlying mechanism behind the effectiveness of betaine was hypothesized to involve its rapid uptake by cells through membrane proteins, providing intracellular protection[73]. Additionally, its effectiveness seems to lie in its capacity to significantly lower the freezing point of water[139,140]. Betaine was observed to improve the integrity of the plasma membranes of sperm tails[141]. However, while betaine may have some benefits at lower concentrations, it may have detrimental effects on semen quality at higher concentrations[142].

Unlike some conventional cryoprotectants (*e.g.*, glycerol and DMSO), glucose falls into the low molecular weight non-penetrating cryoprotectants category. This means that glucose does not easily cross the cell membrane. During the freezing process, water inside and outside the cell tends to form ice crystals, which can lead to cell damage. Glucose helps balance osmotic stress by regulating water movement in and out of the cell, reducing ice crystal formation. Glucose contributes to stabilizing the structure of cell membranes, especially during the freezing and thawing process[143].

Sucrose, as an extracellular cryoprotectant, helps shield the spermatozoa from the adverse effects of cold shock. It does so by surrounding the sperm cells in the semen diluent media. When the temperature drops rapidly during freezing, the presence of sucrose in the extracellular environment forms a protective barrier around the sperm cells. Sucrose helps maintain the structural integrity of the cell membranes by preventing or minimizing the formation of ice crystals and by reducing the osmotic stress that can occur during freezing and thawing. By doing so, it acts as a protective shield for the spermatozoa, ensuring that their cell membranes remain intact[144].

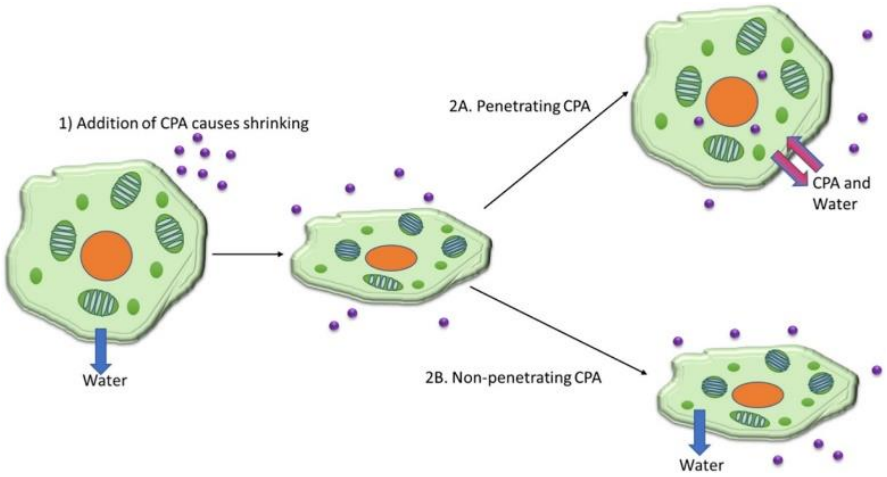

Figure 5.1. Cellular responses to penetrating and non-penetrating cryoprotectants. *Penetrating cryoprotectants are typically small molecules capable of easily diffusing through cell membranes. In contrast, non-penetrating cryoprotectants encompass molecules incapable of membrane penetration (source: Raju et al., 2021 [145]).*

Currently, the typical process of cryopreservation involves four main steps: (1) cryoprotectant agents addition, where cells are exposed to the cryoprotectants for a certain period of time to allow them to penetrate the cells and protect them during the freezing process; (2) freezing, where, to slow down metabolic and biochemical processes, the temperature is reduced at a controlled rate, either gradually or rapidly, to reach a specific low temperature such as 193.15 K or the temperature of liquid nitrogen (77.15 K); (3) thawing where the frozen cells are gradually (or rapidly) warmed up allowing them to transition from a frozen state back to a viable state; (4) cryoprotectant agent removal from the cells. This final step is necessary because some cryoprotectants can be toxic to cells.

In the early 1980s, advancements in cryopreserving embryos led to the first reported human pregnancy from a frozen-thawed embryo in 1983. This practice has evolved into strategies like the "freeze-all" approach, where high-quality embryos are cryopreserved for later transfer, using cryoprotective agents like glycerol, DMSO, and propanediol. The Cryopreservation of oocytes and embryos has grown due to various factors, including medical considerations and patient preferences. However, there are concerns about potential effects on offspring health. Research suggests a possible link between vitrification, especially involving DMSO, and epigenetic dysregulation/imprinting disorders, which involve changes in gene expression patterns influenced by environmental factors, including cryopreservation reagents. DMSO may interfere with DNMT3a enzyme activity, affecting DNA methylation. Vitrification might also alter DNA methylation levels in imprinted genes' regulatory regions. Epigenetic changes following cryopreservation could occur through mechanisms like cryoprotectant toxicity or the generation of reactive oxygen species during freezing-thawing. With the increasing use of cryopreservation techniques in assisted reproductive technologies, there's a need to understand potential long-term health implications for children born through these methods[146–151].

Cryopreservation offers a way to store genetic material, like seeds, from endangered or slow-growing species[152,153], and it has had a significant impact on regenerative medicine, transfusion medicine, and various other biomedical and biotechnological fields. Stem cells are crucial in regenerative medicine, but they have a limited viability window after collection. Cryopreservation allows these cells to be frozen, expanding their availability for clinical use and improving quality control. However, challenges include reduced cell viability upon thawing and potential adverse reactions in patients due to cryoprotectants like DMSO[154–158]. Current storage of red blood cells is limited to 42 days at 277.15 K, leading to potential shortages during emergencies. Cryopreservation could extend storage to 10 years, but it faces challenges, especially for rare blood types. In North America, red blood cells are typically cryopreserved with 40% glycerol and must be processed for over

an hour to reduce glycerol levels to less than 1%, making immediate transfusions challenging. Furthermore, removing the cryoprotectant before transfusion is labor-intensive and costly[159,160]. Cryopreservation has also transformed organ transplantation but faces limitations. Current methods lead to wastage of donated hearts and lungs, with about 60% discarded annually due to short preservation time on ice, typically around four hours[161,162].

Despite its vast potential, cryopreservation faces a significant limitation due to its heavy reliance on two toxic cryoprotective agents, DMSO and glycerol. DMSO, the preferred cryoprotectant, can cause side effects (such as nausea, vomiting, and abdominal cramps, as well as more serious cardiovascular, respiratory, renal, hemolytic, and hepatotoxic issues). Additionally, DMSO can induce oxidative stress, gene expression changes, and damage cell structures such as organelles, cytoskeletons, and membranes, leading to reduced cell viability and functionality.

Improving cryopreservation techniques, including reducing DMSO concentrations and exploring DMSO-free alternatives, is essential for successful stem cell preservation while minimizing side effects. Consequently, research in cryopreservation focuses on finding alternative cryoprotective agents, including substances like sugars, amino acids, and acetamides. However, success in discovering suitable alternatives has been limited.

Recent studies have introduced a promising strategy in cryopreservation, using mixtures of different cryoprotectants instead of relying on a single agent[163–166]. For example, a combination of trehalose, sucrose, glycerol, and skimmed milk at specific concentrations significantly improved the survival rate of *Lactobacillus plantarum* and *Lactobacillus casei* by preserving bacterial cell membranes. In another study, a combination of DMSO and ethylene glycol was found to be the most effective in preserving the ultrastructural organization of seminiferous tubules, maintaining cellular proliferation potential similar to the control group[163]. Additionally, a combination of ethylene glycol and propanediol was identified as the best for maintaining blastocyst viability[165]. Another successful combination was glucose and DMSO at a specific concentration, which doubled viability compared to using either compound alone, mainly by reducing toxic effects associated with cryoprotective agents[166].

Nature provides effective solutions that could offer insights for overcoming challenges in cryopreservation. Many organisms, including certain cold-tolerant animals and plants, have evolved mechanisms to survive harsh winters: they accumulate specific types of metabolites such as sugars, polyols, organic acids, and choline derivatives. These substances are notable for their remarkable ability to form NADESs when mixed in specific molar ratios. Inspired by the strategies used by cold-tolerant organisms, NADESs could pave the way toward more sustainable and efficient cryopreservation approaches. Importantly, NADESs could address the toxicity challenge associated with conventional cryoprotectants like DMSO[167].

A study that involved comparing the cryoprotective efficiency of (Pro:Glu) (5:3), (Pro:Glu) (1:1) and (Pro:Sor) (1:1) DES with glycerol and DMSO using *Saccharomyces cerevisiae* showed that that NADESs could offer a safe and biocompatible alternative[168]. The cryopreserved cells using those NADESs displayed healthier profiles with smooth outer surfaces. In contrast, cells preserved with glycerol and DMSO exhibited rough outer surfaces or even significant distortion. NADES-cryopreserved cells also showed higher cell viability (75–80%) with minimal apoptosis (<1.0%). The authors suggested that NADESs strengthened hydrogen bonding as temperature decreased, thereby restraining water molecule motion which led to effective inhibition of ice recrystallization and protection of cells from ice-induced mechanical damage.

Hornberger *et al.* aimed to create an optimized cryoprotective agent using a combination of trehalose and glycerol NADES mixed with normosol-R and supplemented with isoleucine. Strengthened hydrogen bonding in cryoprotective agents has been associated with enhanced cryoprotective properties. This strengthening effect is more pronounced in NADES than in individual components. The NADES was shown to affect ice morphology differently, compared to glycerol and

trehalose alone; this was linked to a decrease in the risk of lethal intracellular ice formation. Higher NADES concentrations result in reduced ice crystal formation. However, higher osmotic stress from higher concentrations can lead to cell loss. The addition of isoleucine to NADES-based solutions was found not to alter the thermophysical properties of the solution significantly. However, it has a positive impact on the survival and proliferation of cells after thawing. While it might be assumed that cryoprotective agents that exhibit less ice formation would result in improved cell preservation after thawing, this study indicated that this assumption does not always hold true. The correlation between reduced ice formation (favored by lower melting temperatures and enthalpies) and enhanced post-thaw cell recovery is not straightforward and factors beyond ice control play a significant role in determining how effectively cells are preserved during cryopreservation. This could include interactions between the cryoprotective agent and the cellular structures, as well as other biological mechanisms that influence cell survival and recovery after thawing. As a result, a broader range of factors when designing and selecting cryoprotective agents should be considered, moving beyond ice crystallization minimization[169]. Another study challenged the notion that cryopreservation outcomes are solely determined by ice crystal control[170]. NADESs consisting of intracellular metabolites like glucose, xylitol, proline, and sorbitol were explored as alternatives for lactic acid bacteria cryostorage due to their ability to inhibit ice crystal formation. NADESs' cryopreservation of lactic acid bacteria involved multiple factors: ice crystal formation, intracellular protein denaturation, and cell membrane integrity. It was also observed that choline chloride-based NADESs were optimal for short-term cryopreservation, while glycerol-based NADESs excelled in long-term cryopreservation.

When relatively large amounts of NADESs are present water crystallization is effectively prevented, reducing the risk of ice-induced damage to cells. Moreover, the melting temperatures of these mixtures are consistently lower than those of pure water, meaning that the formation of ice crystals is delayed. Conversely, when smaller quantities of NADESs are introduced, they prompt alterations in the temperature at which water crystallizes. This effect can lead to a decrease in the crystallization temperature, with potential reductions of up to -22.1 K. Importantly, the introduction of NADESs does not just impact the crystallization temperature; it also influences the characteristics of the crystals that form. Specifically, the inclusion of (Pro:Glu) (5:3) NADES in the water mixture results in a notable change in crystallization temperature, even when the NADES is present in smaller proportions compared to a (Glu:U:Pro) (1:1:1) mixture. Furthermore, the presence of (Pro:Glu) NADES leads to the formation of smaller crystals with distinct shapes compared to bulk water. The smaller and differently shaped crystals formed in the presence of (Pro:Glu) NADES could potentially have a protective effect considering that these altered crystals might mitigate the risk of damaging cell walls during the freezing process[171].

Cryopreservation of sperm is known to lead to alterations in various sperm parameters, which can negatively affect sperm viability, motility, acrosome integrity, and DNA integrity. To mitigate these effects, researchers have turned to using NADESs as potential cryoprotective agents. (Pro:Gly) (1:3), (ChCl:U) (1:2), and (ChCl:Sor:Wat) (2:5:6), exhibit positive effects on preserving sperm quality while preserving the expression levels of genes coding for crucial channel proteins located in the sperm membrane (TRPV1, TRPV4, OGG1, and SPACA3) suggesting that these solvents can effectively protect sperm functionality during freezing and thawing processes. Additionally, it was found that certain NADESs had a positive impact on maintaining chromatin condensation[172].

The primary aim of the study reported herein, was to assess the cryoprotective potential of three distinct DESs in the context of human cell permeability. Specifically, the performance of the DESs using the HaCaT cell line was evaluated. The formulation of these DESs and their component ratios can be found in **Table 5.1**.

Table 5.1. DESs used in this work and their respective molar ratios.

NADESs	Component A	Component B	Component C	Component D	Molar Ratio
Tre:Gly	Trehalose	Glycerol			1:30
Tre:Glu:Sor:Wat	Trehalose	Glucose	Sorbitol	Water	1:1:1:30
Bet:Gly:Suc:Wat	Betaine	Glycerol	Sucrose	Water	2:3:1:5

5.2 MATERIALS AND METHODS

5.2.1 Chemicals

Cryoprotectants: DMSO (10% v/v), 3 DESs (10% w/v) comprising Betaine, Sucrose, Glycerol, and Water (Bet:Gly:Suc:Water) in the molar ratio (2:3:1:5), Trehalose and Glycerol (Tre:Gly) in a molar ratio of 1:30 and Trehalose, Glucose, Sorbitol, and Water (Tre:Glu:Sor:Wat) in the molar ratio (1:1:1:13) and the corresponding physical mixtures for each DES (at 10% w/v).

Phosphate-buffered saline (PBS) aqueous solutions in deionized H_2O with the following concentrations: 140 mM of sodium chloride (NaCl), 10 mM of phosphate buffer, and 3 mM of potassium chloride (KCl). The resultant PBS solution exhibited a pH of 7.4.

Accutase® (cell detachment solution) – 1 X Accutase enzymes prepared in Dulbeccos PBS (0.2g/L KCl, 0.2g/L $KH2PO_5$, 8g/L NaCl, and 1.15g/L Na_2HPO_4) containing 0.5 mm EDTA·4Na and 3 mg/L Phenol Red.

Dulbecco's Modified Eagle Medium (DMEM) (4.5 g/L of glucose, L-glutamine, and sodium pyruvate) supplemented with 10% of fetal bovine serum (FBS), 1% of penicillin and streptomycin.

Poly-L-lysine - positively charged synthetic polymer that interacts with the negatively charged cell membrane, promoting cell immobilization.

5.2.1 Methodology

First described in 1988[173], HaCaT cells were originally established from human keratinocytes obtained from adult human skin biopsies. They were subsequently immortalized through the spontaneous introduction of the Simian Virus 40(SV40) large T antigen, allowing them to undergo "unlimited" cell division while maintaining their phenotypic characteristics. The T antigen is a viral protein derived from the SV40, a DNA virus that primarily infects monkeys. The large T antigen promotes the replication of the viral DNA within infected cells by binding to and inactivating certain tumor suppressor proteins in the host cell, such as p53 and retinoblastoma[174]. HaCaT cells display close similarities to normal human keratinocytes making them a valuable model system[175]. As a result, they have been extensively characterized and used as an *in vitro* model. Working with HaCaT cells with a spherical shape, makes it easier to measure and calculate cell volume changes accurately in shrink/swell studies.

HaCaT cells were washed multiple times with PBS to remove any residual culture medium. These cells tend to aggregate, which may complicate cell counting or single-cell analysis. Therefore, 7 mL of Accutase® was added to aid in the detachment, and cells were incubated at 37 ºC for 5-10 minutes. Accutase® is a cell detachment solution that contains enzymes derived from marine sources that exhibit proteolytic activity collagenolytic activity. 13 mL of DMEM was then added to neutralize the Accutase® solution followed by centrifugation at 300×g for 3 minutes to separate the cells from the surrounding medium and the supernatant containing residual Accutase® and DMEM. After discarding the supernatant, the cells (found in the pellet) were resuspended in DMEM and 20 µL of cells suspension were added to 180 µL of media (DMEM). Next, 10 µL of the resulting cell suspension was used for

cell counting using a Neubauer chamber. the following formula was used to calculate the initial cell concentration (c_i) using a Neubauer chamber:

$$c_i = Number\ of\ cells\ counted \times Dilution\ factor \times 10000 \quad \textbf{(5.1)}$$

The initial concentration of cells was 6×10^4 cells/mL. A total volume of 34.5 µL of HaCaT cell suspension was mixed with 966 µL of DMEM. From this mixture, 250 µL of the cell suspension was plated in a 24-well plate for further analysis. Next, 250 µL of a 20% (w/v) of each tested NADES or physical mixture, or 20% (v/v) of DMSO were added to each well, to reach a final concentration of 10% (w/v) or 10% (v/v), respectively. To minimize cell movement and facilitate the observation under the microscope, poly-L-lysine was added.

For visualization, image capture, and analysis, the ZEN blue software platform (version 3.4.91) was used in this study. To capture the dynamics of the cellular response to the abovementioned substances, a series of time-lapse images were acquired. At first, images were captured at three time points: 0 seconds (baseline), 2 seconds, and 60 seconds. However, considering that the DESs exhibit slower penetration into the cells, additional time points (120 seconds, 180 seconds, 300 seconds, 600 seconds, and 2400 seconds) were included to capture their effects and temporal changes in cellular volume (**fig. 5.2.**). The captured images of the cells, obtained under a microscope equipped with a 20× objective lens, were imported into the ZEN blue software, and analyzed. The analysis of the captured images involved quantifying the cell diameter using image analysis software integrated within the ZEN blue platform to estimate the cell volume. It was assumed that the cells exhibited a spherical shape for simplification purposes. Once the diameters were obtained, the corresponding cell volumes were calculated using the formula for the volume of a sphere $V_{\text{sphere}} = (4\pi/3)(d/2)^3$, where V and d represent the volume and diameter of the cell, respectively.

To remove any inherent variations in cell size that might have existed (unrelated to the experiments) due to genetic differences, different growth rates, or other factors, the cell volume data was normalized to the initial time point (t = 0). By normalizing the data to the initial time point, we can effectively focus on the changes in cell volume exclusively induced by the DESs and eliminate the influence of any pre-existing differences among the cells.

$$Normalized\ cell\ volume\ = \frac{Cell\ volume\ at\ time\ point\ t}{Cell\ volume\ at\ time\ point\ 0} \quad \textbf{(5.2)}$$

To ensure the accuracy and reliability of the results as well as to account for any variations that may naturally arise between individual cells, at least six cells were assessed for each solvent tested.

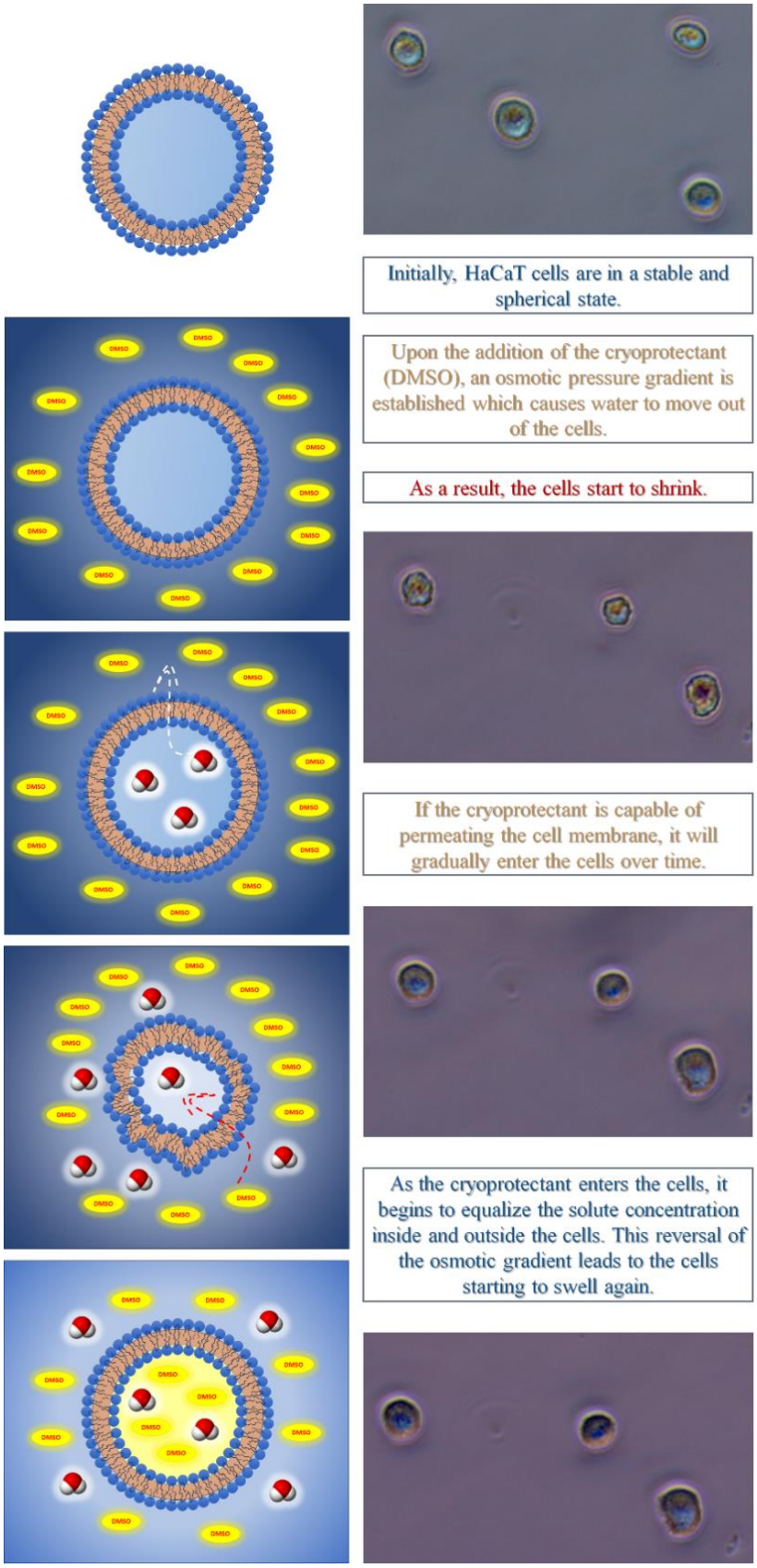

Figure 5.2. Cell response to cryoprotectant (DMSO) addition. *When the cryoprotectant is introduced, osmotic pressure causes water to exit the cells, leading to cell shrinkage. Over time, if the cryoprotectant can penetrate the cell membrane, it reverses the osmotic gradient, causing the cells to swell again.*

5.3 RESULTS AND DISCUSSION

In this study, we evaluated the cryoprotective properties of three distinct cryoprotectant formulations: (Bet:Gly:Suc:Wat), (Tre:Gly), and (Tre:Glu:Sor:Wat). These formulations were tested against their respective physical mixtures (PM_BGSW, PM_TG, and PM_TGSW) to demonstrate that each DES is more than just the sum of its parts, concerning its cryoprotective properties.; it possesses distinct characteristics and behaviors that differentiate it from its constituent components. **Figure 5.3 (a)** compares the shrinkage/swelling analyses for each DES tested along with DMSO.

HaCaT cells can regulate their gene expression to produce transport proteins specific to osmolytes like betaine. When HaCaT cells experience osmotic differences that lead to cell shrinkage, they can increase the production of betaine transporters (such as BGT1 and GABA) to enhance the uptake of betaine into the cells[176,177]. If the final cell volume after exposure to betaine is significantly higher than the volume of the DES itself, it might suggest that the volume increase observed when cells are exposed to (Bet:Gly:Suc:Wat) is not due to the increased expression of betaine transporters (**fig. 5.3 (b)**). It should be noted, however, that for THP1 cells, no swelling was reported when exposed to betaine and the solute that lead to higher solute permeability is in fact glycerol[178]. (Bet:Gly:Suc:Wat) exhibits similar results to Gly (permeating) and Suc (nonpermeating). Hence, it is possible that the potential cryoprotective mechanism of (Bet:Gly:Suc:Wat) is similar to that of one of these components. Another possibility is that some of its components behave as permeating cryoprotectants (similar to glycerol) and others behave as nonpermeating cryoprotectants (similar to sucrose). The results obtained with (Bet:Gly:Suc:Wat) are intriguing because they indicate that this DES may have the potential to be as effective as glycerol in terms of cell volume recovery. Despite of its widespread use, glycerol does not provide the same level of cryoprotection as some other cryoprotectants like DMSO and even though it is classified as a typical penetrating cryoprotectant, it displays relatively poor penetrability[168]. The inclusion of sucrose in cryoprotectant media prevents osmotic-based shrinkage which can lead to cellular damage[179]. While sucrose may not be considered a top-performing cryoprotectant, it still demonstrates some ability to protect cells during the cryopreservation process[180,181]. Sucrose's role as an extracellular cryoprotectant is to protect the spermatozoa's plasma membrane from mechanical damage during cryopreservation. Sucrose's protective effect on the plasma membrane is attributed to the presence of carbohydrates on the outer surface of the cell membrane, forming structures known as cell sheaths. It is thought that sucrose interacts with these carbohydrates, creating a protective barrier. Even if the carbohydrates in the spermatozoa cell membrane are damaged during cryopreservation, the added sucrose is expected to act as a substitute, helping maintain the structural integrity of the cell sheath[144]. So, while sucrose is not necessarily used as the primary cryoprotectant, it is often added to the cryoprotective solution to provide a layer of structural protection to the cells. To consider the DES as a viable alternative to glycerol, further studies are needed, specifically, understanding how the DESs enter the cells, its mechanism of action, and assess its toxicity.

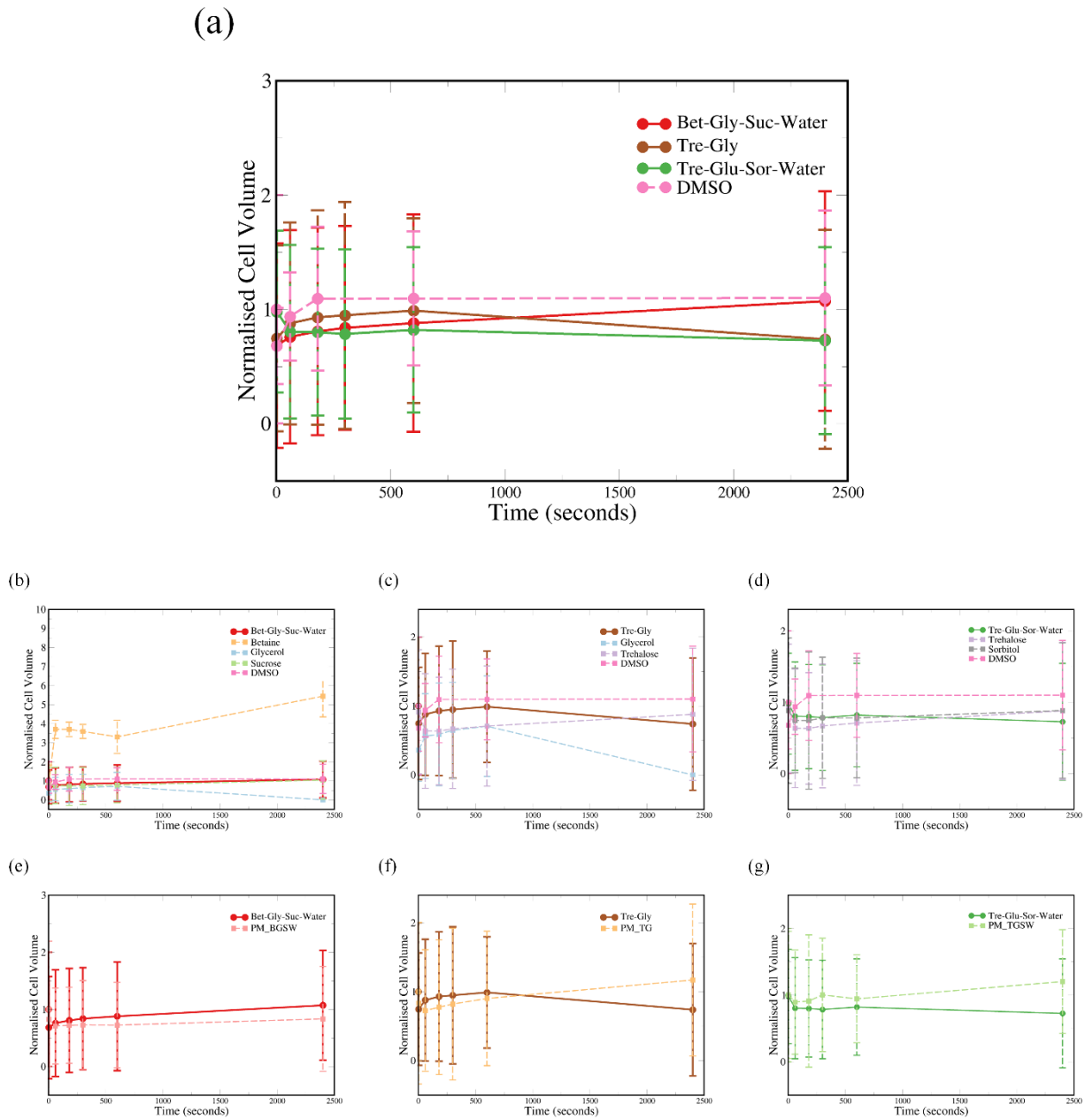

Figure 5.3. Comparative HaCaT cell volume responses to DESs. *(a) The studied NADESs were compared to the widely used DMSO; (b) Bet:Gly:Suc:Wat reveals similarities with both DMSO and sucrose; (c) Tre:Gly exhibits a behavior similar to DMSO in terms of initial cell recovery, but with a subsequent decrease in cell volume, raising questions about its sustained effects; (d) Tre:Glu:Sor:Wat seems to be unable to enter the cells; Additionally, (e) Bet:Gly:Sor:Wat, (f) Tre:Gly, and (g) Tre:Glu:Suc:Wat are compared to their corresponding physical mixtures.*

The ultimate goal is to find a cryoprotectant or combination of compounds that is as effective as glycerol but potentially less toxic to cells.

Comparing (Bet:Gly:Suc:Wat) to DMSO (a small molecule), it is notable that both exhibit similar initial cell shrinkage (at 2 seconds), but over time, (Bet:Gly:Suc:Wat) shows a more gradual increase in cell volume, reaching a level comparable to DMSO at 2400 seconds. This suggests that (Bet:Gly:Suc:Wat) has the potential to be as effective as DMSO, one of the most widely used cryoprotectants, in terms of cell volume recovery during the cryopreservation process. Once again, further research is needed to assess other aspects like toxicity to determine its viability as an alternative to DMSO.

Proteomic analysis revealed that trehalose induced the expression of proteins associated with dehydration protection. Trehalose appears to trigger a cellular response in HaCaT cells that enhances their ability to survive and function under dehydrating conditions[182]. (Tre:Gly) has a milder effect on cell volume reduction, inducing a smaller decrease in cell volume compared to glycerol and trehalose alone (**fig. 5.3(c)**). Thus, (Tre:Gly) leads to a faster recovery of the cell volume as indicated by the increase in the cell volume over time. However, cell volume starts to decrease again at 600 s in the case of (Tre:Gly). While (Tre:Gly) initially promotes a faster volume recovery, it may not provide sustained protection against volume reduction over extended periods. Whereas this decrease may not necessarily indicate cell damage, but rather the cells adjusting to the osmotic conditions of the solution they are in, the former cannot be disregarded. Cell membranes may become compromised, leading to the loss of intracellular contents and a volume reduction, which could be related to the toxicity of the cryoprotectant. While glycerol is present in a much higher molar ratio than trehalose in this DES, their interactions lead to a behavior that may not be directly proportional to their molar ratios so the suggestion that this mixture is not a DES solely based on its molar ratio seems to be an oversimplification. The behavior of (Tre:Gly) is the result of its molecular interactions, which differ significantly from what one would expect in a simple glycerol solution. Additionally, the specific interactions and properties of this DES seem to provide benefits in terms of cell recovery, although they may also lead to adverse effects since (Tre:Gly) mitigates the initial osmotic shock by reducing the loss of cell volume, inducing a faster cell volume recovery, seemingly offering, therefore, short term advantages over individual components, like glycerol.

Thus, as a potential cryoprotectant, (Tre:Gly) exhibits a milder effect on cell volume reduction compared to glycerol and trehalose alone, accompanied by a faster initial recovery of cell volume. However, the observed decrease in cell volume at 2400 s suggests the possibility of long-term toxic or damaging effects associated with (Tre:Gly). In comparison to DMSO, (Tre:Gly) demonstrates similarities concerning initial cell recovery but, once again, lacks sustained effects. Further research is needed to unravel the underlying mechanisms behind (Tre:Gly)'s behavior, towards the rational design of enhanced cryoprotectant strategies to address its limitations.

It is evident that (Tre:Glu:Sor:Wat) does induce an initial cell shrinkage (water leaving the cells), as expected (**fig. 5.3(d)**). However, the absence of a subsequent recovery and the continuous decrease in cell volume over time suggest that (Tre:Glu:Suc:Wat) may not effectively enter the cells to promote cell volume recovery. This suggests that (Tre:Glu:Sor:Wat) does not mitigate the osmotic shock and maintain cell integrity. This is in contrast to DESs like (Bet:Gly:Suc:Wat) and (Tre:Gly), which showed full or partial recovery over time.

At the initial time point (2 s), PM_BGSW induces a more pronounced cell shrinkage (0.8265) compared to (Bet:Gly:Suc:Wat) (0.6834) suggesting that water loss from the cells is more immediate and significant compared to PM_BGSW (**fig. 5.3(e)**). This can be considered a favorable characteristic for (Bet:Gly:Suc:Wat) as a cryoprotectant in the context of cryopreservation, as it helps minimize the risk of intracellular ice formation inside cells during freezing. (Bet:Gly:Suc:Wat) shows a relatively steady increase in cell volume, indicating gradual entry into cells. In contrast, the results suggest that PM_BGSW might enter the cells in a slower and less efficient manner. PM_BGSW's failure to recover the initial cell volume indicates that it is unable to effectively recover the cells from the initial osmotic shock. The (Bet:Gly:Suc:Wat) DES not only enables volume recovery but actually surpasses the initial cell volume over time. This suggests that (Bet:Gly:Suc:Wat) is more successful at mitigating osmotic shock and supporting cell recovery, which aligns with the desired characteristics of a cryoprotectant.

Both (Tre:Gly) and PM_TG exhibit a similar magnitude of cell shrinkage, however, (Tre:Gly) induces this shrinkage faster, suggesting a more rapid water loss from the cells. On the other hand, PM_TG suggests a slower entry into the cells since (**fig. 5.3. (f)**). The initial osmotic shock is comparable in terms of magnitude and while the initial shock is similar, the key distinction is in the

recovery phase. PM_TG exhibits a gradual recovery of cell volume over time, indicating its ability to mitigate the osmotic shock and support cell recovery.

PM_TGSW leads to a recovery in cell volume over time, and the final volume is higher than the initial volume suggesting that the physical mixture is more effective at mitigating the osmotic shock and supporting cell integrity during compared to the (Tre:Glu:Sor:Wat) DES (**fig. 5.3. (g)**). This emphasizes that, in this specific case, the physical mixture appears to be a more suitable cryoprotectant than its corresponding DES formulation. The presumable stronger hydrogen bonding within the (Tre:Glu:Sor:Wat) DES may not be as beneficial for cryoprotection compared to the physical mixture. And although the presence of sorbitol and trehalose results in swelling, at 2400 s neither sorbitol (0.8844055925) or trehalose (0.8788633118) lead to a full volume recovery whereas the physical mixture did result in a full recovery (1.203591289 at 2400 s).

The magnitude of the initial shrinkage indicates the magnitude of the osmotic shock induced by different components: Glycerol (0.6410127485) > Trehalose (0.3654388265) > DMSO (0.3205159828) > (Bet:Gly:Suc:Wat) (0.3166226382) > PM_BGSW (0.2907728605) > Sucrose (0.2795860874) > PM_TG (0.2739368332) > Sorbitol (0.2565177077) > (Tre:Gly) (0.2533141033) > PM_TGSW (0.1084429658) > Betaine (0.1026150951). The results indicate that glycerol, trehalose and DMSO result in the highest osmotic shock, while betaine, PM_TGSW and (Tre:Gly) lead to the lowest osmotic shock among the tested components.

It appears that the presence of stronger hydrogen bonding in DESs may be favorable when the components are predominantly permeating cryoprotectants, as observed in the DESs formulations where betaine and glycerol (both permeating) are the main components. On the other hand, when the formulation consists mostly of nonpermeating cryoprotectants, the stronger hydrogen bonding may not lead to favorable cryoprotective effects, as seen in the (Tre:Glu:Sor:Wat) DES. Regardless, these differences unequivocally demonstrate that the DES is not merely a mixture of its individual components. These results highlight that the effects previously observed are a result of the unique interactions and properties that emerge when these components are combined to form the DES.

The reasons for this difference and their effects on cell physiology are complex but it seems as though that for this particular DES, stronger hydrogen bonding hinders cellular penetration whilst for (Bet:Gly:Sor:Wat) and (Tre:Gly), it seems to enhance it. (Bet:Gly:Suc:Wat) (2:3:1:5) contains primarily permeating cryoprotectants (betaine and glycerol) and (Tre:Gly) (1:30) contains a very high ratio of glycerol, a permeating cryoprotectant. However, (Tre:Glu:Sor:Wat) (1:1:1:13) lacks a significant proportion of permeating cryoprotectants; it mainly consists of nonpermeating cryoprotectants. The DESs containing predominantly permeating cryoprotectants were favorable in cryopreservation. In contrast, the DES formulation lacking a significant proportion of permeating cryoprotectants did not perform as well.

5.4 CONCLUSION

The contrast between cell volume response between (Bet:Gly:Suc:Wat) and betaine alone hints at distinct mechanisms of action which require further examination. (Bet:Gly:Suc:Wat) revealed intriguing similarities with both glycerol (a permeating cryoprotectant) and sucrose (a nonpermeating cryoprotectant). This suggests that (Bet:Gly:Suc:Wat) might share its cryoprotective mechanism with one of these components or have a hybrid mechanism including permeating and nonpermeating elements, resulting in a combined cryoprotective effect. The cell volume recovery dynamics of (Bet:Gly:Suc:Wat) was found to be comparable to the widely used cryoprotectant DMSO. It seems reasonable to conclude that the (Tre:Gly) DES exhibits a behavior similar to DMSO concerning the initial cell recovery (after exposure to these substances) and initial cell volume loss. However, a major distinction is that the effect of (Tre:Gly) on the cell volume does not seem to be sustained over an extended period. In the case of (Tre:Gly), there is a subsequent cell volume decrease at 2400 s (40 min). Understanding the underlying mechanism of (Tre:Gly) concerning its effect on the cells, especially the source of the eventual volume decrease, is essential, as it could provide insights into the difference between (Tre:Gly)and DMSO helping its optimization as a cryoprotectant agent.

(Bet:Gly:Sor:Wat), (Tre:Gly), and (Tre:Glu:Suc:Wat) were tested against their corresponding physical mixtures (PM_BGSW, PM_TG, and PM_TGSW) manifesting distinct characteristics and behaviors. (Bet:Gly:Sor:Wat) displayed the ability to mitigate cell shrinkage, promote recovery, and surpass initial cell volume. Similarly, (Tre:Gly) demonstrated rapid cell shrinkage, with (PM_TG) showing a similar initial shock but slower recovery. This indicates the potential of (Tre:Gly) to alleviate osmotic shock and enhance recovery. In contrast, (Tre:Glu:Suc:Wat) failed to initiate cell recovery, suggesting limitations in maintaining cell integrity. (PM_TGSW) outperformed this DES, implying that the assumed stronger hydrogen bonding within (Tre:Glu:Suc:Wat) hindered cellular penetration, unlike (Bet:Gly:Sor:Wat) and (Tre:Gly). These assays showed, therefore, that DESs rich in permeating components performed favorably, while the one lacking them displayed a suboptimal performance.

CHAPTER 6

Conclusions and Future Perspectives

The first part of this thesis undertook an optimization of the GAFF force field to simulate a (Bet:Gly) DES. We addressed the inherent limitations of the default GAFF parameters, particularly in predicting the density and viscosity of this NADES. Our findings underscored the inadequacy of solely manipulating atomic charges through scaling factors, as it failed to simultaneously capture the density and viscosity behaviors. To overcome these challenges, we introduced a second (size) scaling factor, on the Lennard-Jones potential. This additional degree of freedom allowed us to match more closely the experimental data. The iterative process of adjusting these scaling factors culminated in the development of an optimized GAFF force field (GAFF-opt) characterized by an 8% reduction in atomic charges ($\lambda_Q = 0.92$) and a 3% increase in the atomic sigma ($\lambda_\sigma = 1.03$). GAFF-opt exhibited a minor (0.58%) overestimation of the experimental density and an underestimation of viscosity by approximately 7%.

In the second part of this thesis, we studied the dynamics and the molecular basis underlying the widely reported stability of biomolecules, particularly proteins, in deep eutectic solvents. Our findings challenge the preferential hydration mechanism, used to explain protein stability by osmolytes (common components of NADESs). Contrary to this hypothesis, the DES studied here traps water molecules within its structure. This precludes the formation of a conventional hydration layer around UBQ resulting in a significant slowdown of the protein conformational dynamics. This phenomenon, governed by elementary kinetic steps, hinted at the role of protein-solvent shell coupled fluctuations, in addition to the viscosity. These insights aligned with the framework of protein slaving and provided a new perspective on how DESs may influence protein structure as well as its response to temperature changes.

The third and final part of this thesis ventured into a closely related practical application by examining the permeability of DES into HaCaT cells and their potential as new cryoprotectants. We found a stark contrast in cell volume responses between (Bet:Gly:Suc:Wat) and betaine alone, hinting at distinct mechanisms of action. The behavior of (Bet:Gly:Suc:Wat) displayed intriguing similarities with both glycerol (a permeating cryoprotectant) and sucrose (a nonpermeating cryoprotectant). Moreover, our findings revealed that (Tre:Gly) exhibited cell volume recovery dynamics comparable to the widely used cryoprotectant DMSO. However, it also exhibited a subsequent decrease in cell volume at a later stage, a phenomenon not observed with DMSO.

In order to enter the cells, DESs must have chemical properties that allow the components to interact with osmosensors or transport proteins on the cell membrane. If the molecule lacks the necessary chemical features that match the binding sites of osmosensors or transporters, it may not be recognized and this may be one of the reasons why certain DESs, although theoretically suitable for regulating osmotic stress, may not be uptaken by cells.

Cells have evolved to recognize and transport natural osmolytes efficiently. NADESs, however, despite being formed by osmolytes, may not be recognized by these recognition systems in cells. A DES may be seen as a “strange compound” by the cell during osmotic crisis. However, the fact that some DESs can effectively enter the cells, either through diffusion or perhaps aided by membrane proteins, suggests that the cells recognize some DESs in times of stress. Cells have specific transporters for different osmolytes. A NADES might not be a substrate for any of the existing transporters even if it contains a natural osmolyte suggesting that some key structural feature is not recognized by transporters possibly due to the interactions amongst the components in the DES, even at low concentrations.

However, it must be taken into consideration that cells have complex regulatory mechanisms, signaling pathways, and feedback loops, that are activated to respond to osmotic stress. DESs may not integrate effectively into these cellular signaling networks. Very little is known about DESs’ impact on gene expression and their interactions with genetic material. The impact of well-established

cryoprotectants in general on the genetic component of cryopreserved biomaterial is actually a topic of ongoing debate.

This study did not assess cellular viability. The uptake of the tested DES provides some evidence that cells are viable, but nothing can be said concerning the long-term effects of the tested NADESs and their toxicity on HaCaT cells.

The fact that the mathematical equation used to model the change in cell volume (V_{cell}) over time in the presence of a solute did not perform well when the "solute" used were DESs is also a point of interest. Thus, considering this is a well-established model, it is important to address why some volume changes in the presence of some DESs are accurately predicted whilst others are not. Understanding the underlying mechanisms of these effects may hold the key to optimizing the use of DESs as cryoprotectant agents.

Future MD simulations should aim at deciphering DESs-membrane interactions underlying the observed effects on cell volume. These simulations may bridge the gap between theory and experiment and perhaps help answer some of the questions that remain unanswered. Simultaneously, experimental investigations are instrumental in validating and contextualizing these computational findings. Highlighting the synergy between computational and experimental approaches was one of the goals of this thesis. It is not merely a choice between one or the other; instead, it is a harmonious partnership where each methodology complements the other. Computational simulations offer atomic-level explanations that aid in the experimental process. Conversely, experimental results ground our simulations in real-world applications, ensuring that our more fundamental research translates into practical solutions.

REFERENCES

(1) Paiva, A.; Craveiro, R.; Aroso, I.; Martins, M.; Reis, R. L.; Duarte, A. R. C. Natural Deep Eutectic Solvents – Solvents for the 21st Century. *ACS Sustain. Chem. Eng.* **2014**, *2* (5), 1063–1071. https://doi.org/10.1021/sc500096j.

(2) Kohli, R. Applications of Ionic Liquids in Removal of Surface Contaminants. In *Developments in Surface Contamination and Cleaning: Applications of Cleaning Techniques*; Elsevier, 2019; pp 619–680. https://doi.org/10.1016/B978-0-12-815577-6.00016-5.

(3) Vasil'eva, I.; Morozova, O.; Shumakovich, G.; Yaropolov, A. Betaine-Based Deep Eutectic Solvent as a New Media for Laccase-Catalyzed Template-Guided Polymerization/Copolymerization of Aniline and 3-Aminobenzoic Acid. *Int. J. Mol. Sci.* **2022**, *23* (19), 11409. https://doi.org/10.3390/ijms231911409.

(4) Halder, A. K.; Cordeiro, M. N. D. S. Probing the Environmental Toxicity of Deep Eutectic Solvents and Their Components: An In Silico Modeling Approach. *ACS Sustain. Chem. Eng.* **2019**, *7* (12), 10649–10660. https://doi.org/10.1021/acssuschemeng.9b01306.

(5) Hammond, O. S.; Bowron, D. T.; Edler, K. J. Liquid Structure of the Choline Chloride-Urea Deep Eutectic Solvent (Reline) from Neutron Diffraction and Atomistic Modelling. *Green Chem.* **2016**, *18* (9), 2736–2744. https://doi.org/10.1039/C5GC02914G.

(6) Hammond, O. S.; Bowron, D. T.; Edler, K. J. The Effect of Water upon Deep Eutectic Solvent Nanostructure: An Unusual Transition from Ionic Mixture to Aqueous Solution. *Angew. Chem.* **2017**, *129* (33), 9914–9917. https://doi.org/10.1002/ange.201702486.

(7) Di Pietro, M. E.; Tortora, M.; Bottari, C.; Colombo Dugoni, G.; Pivato, R. V.; Rossi, B.; Paolantoni, M.; Mele, A. In Competition for Water: Hydrated Choline Chloride:Urea vs Choline Acetate:Urea Deep Eutectic Solvents. *ACS Sustain. Chem. Eng.* **2021**, *9* (36), 12262–12273. https://doi.org/10.1021/acssuschemeng.1c03811.

(8) Pandey, A.; Pandey, S. Solvatochromic Probe Behavior within Choline Chloride-Based Deep Eutectic Solvents: Effect of Temperature and Water. *J. Phys. Chem. B* **2014**, *118* (50), 14652–14661. https://doi.org/10.1021/jp510420h.

(9) Antunes, M.; Campinhas, A.-S.; de Sá Freire, M.; Caetano, F.; Diogo, H. P.; Colaço, R.; Branco, L. C.; Saramago, B. Deep Eutectic Solvents (DES) Based on Sulfur as Alternative Lubricants for Silicon Surfaces. *J. Mol. Liq.* **2019**, *295*, 111728. https://doi.org/10.1016/j.molliq.2019.111728.

(10) Abbott, A. P.; Capper, G.; Davies, D. L.; Rasheed, R. K.; Tambyrajah, V. Novel Solvent Properties of Choline Chloride/Urea mixturesElectronic Supplementary Information (ESI) Available: Spectroscopic Data. See Http://Www.Rsc.Org/Suppdata/Cc/B2/B210714g/. *Chem. Commun.* **2003**, No. 1, 70–71. https://doi.org/10.1039/b210714g.

(11) Makoś, P.; Słupek, E.; Gębicki, J. Hydrophobic Deep Eutectic Solvents in Microextraction Techniques–A Review. *Microchem. J.* **2020**, *152*, 104384. https://doi.org/10.1016/j.microc.2019.104384.

(12) Hansen, B. B.; Spittle, S.; Chen, B.; Poe, D.; Zhang, Y.; Klein, J. M.; Horton, A.; Adhikari, L.; Zelovich, T.; Doherty, B. W.; Gurkan, B.; Maginn, E. J.; Ragauskas, A.; Dadmun, M.; Zawodzinski, T. A.; Baker, G. A.; Tuckerman, M. E.; Savinell, R. F.; Sangoro, J. R. Deep Eutectic Solvents: A Review of Fundamentals and Applications. *Chem. Rev.* **2021**, *121* (3), 1232–1285. https://doi.org/10.1021/acs.chemrev.0c00385.

(13) Smith, E. L.; Abbott, A. P.; Ryder, K. S. Deep Eutectic Solvents (DESs) and Their Applications. *Chem. Rev.* **2014**, *114* (21), 11060–11082. https://doi.org/10.1021/cr300162p.

(14) Hayyan, M.; Hashim, M. A.; Hayyan, A.; Al-Saadi, M. A.; AlNashef, I. M.; Mirghani, M. E. S.; Saheed, O. K. Are Deep Eutectic Solvents Benign or Toxic? *Chemosphere* **2013**, *90* (7), 2193–2195. https://doi.org/10.1016/j.chemosphere.2012.11.004.

(15) Van Der Spoel, D.; Lindahl, E.; Hess, B.; Groenhof, G.; Mark, A. E.; Berendsen, H. J. C. GROMACS: Fast, Flexible, and Free. *J. Comput. Chem.* **2005**, *26* (16), 1701–1718. https://doi.org/10.1002/jcc.20291.
(16) Fermi, E.; Pasta, P.; Ulam, S.; Tsingou, M. *STUDIES OF THE NONLINEAR PROBLEMS*; LA-1940, 4376203; 1955; p LA-1940, 4376203. https://doi.org/10.2172/4376203.
(17) Alder, B. J.; Wainwright, T. E. Studies in Molecular Dynamics. I. General Method. *J. Chem. Phys.* **1959**, *31* (2), 459–466. https://doi.org/10.1063/1.1730376.
(18) Rahman, A. Correlations in the Motion of Atoms in Liquid Argon. *Phys. Rev.* **1964**, *136* (2A), A405–A411. https://doi.org/10.1103/PhysRev.136.A405.
(19) Verlet, L. Computer "Experiments" on Classical Fluids. I. Thermodynamical Properties of Lennard-Jones Molecules. *Phys. Rev.* **1967**, *159* (1), 98–103. https://doi.org/10.1103/PhysRev.159.98.
(20) Rahman, A.; Stillinger, F. H. Molecular Dynamics Study of Liquid Water. *J. Chem. Phys.* **1971**, *55* (7), 3336–3359. https://doi.org/10.1063/1.1676585.
(21) McCammon, J. A.; Gelin, B. R.; Karplus, M. Dynamics of Folded Proteins. *Nature* **1977**, *267* (5612), 585–590. https://doi.org/10.1038/267585a0.
(22) Arnittali, M.; Rissanou, A. N.; Harmandaris, V. Structure Of Biomolecules Through Molecular Dynamics Simulations. *Procedia Comput. Sci.* **2019**, *156*, 69–78. https://doi.org/10.1016/j.procs.2019.08.181.
(23) On the Determination of Molecular Fields. —II. From the Equation of State of a Gas. *Proc. R. Soc. Lond. Ser. Contain. Pap. Math. Phys. Character* **1924**, *106* (738), 463–477. https://doi.org/10.1098/rspa.1924.0082.
(24) Haile, J. M. *Molecular Dynamics Simulation: Elementary Methods*, Wiley professional paperb. ed.; A Wiley-Interscience publication; Wiley: New York, NY, 1997.
(25) Damasceno, D. A.; Mesquita, E.; Rajapakse, R. N. K. D. Mechanical Behavior of Nano Structures Using Atomic-Scale Finite Element Method (AFEM). *Lat. Am. J. Solids Struct.* **2017**, *14* (11), 2046–2066. https://doi.org/10.1590/1679-78254050.
(26) Hornak, V.; Abel, R.; Okur, A.; Strockbine, B.; Roitberg, A.; Simmerling, C. Comparison of Multiple Amber Force Fields and Development of Improved Protein Backbone Parameters. *Proteins Struct. Funct. Bioinforma.* **2006**, *65* (3), 712–725. https://doi.org/10.1002/prot.21123.
(27) Ren, P.; Ponder, J. W. Polarizable Atomic Multipole Water Model for Molecular Mechanics Simulation. *J. Phys. Chem. B* **2003**, *107* (24), 5933–5947. https://doi.org/10.1021/jp027815+.
(28) Jorgensen, W. L.; Chandrasekhar, J.; Madura, J. D.; Impey, R. W.; Klein, M. L. Comparison of Simple Potential Functions for Simulating Liquid Water. *J. Chem. Phys.* **1983**, *79* (2), 926–935. https://doi.org/10.1063/1.445869.
(29) Horn, H. W.; Swope, W. C.; Pitera, J. W.; Madura, J. D.; Dick, T. J.; Hura, G. L.; Head-Gordon, T. Development of an Improved Four-Site Water Model for Biomolecular Simulations: TIP4P-Ew. *J. Chem. Phys.* **2004**, *120* (20), 9665–9678. https://doi.org/10.1063/1.1683075.
(30) Dick, T. J.; Madura, J. D. Chapter 5 A Review of the TIP4P, TIP4P-Ew, TIP5P, and TIP5P-E Water Models. In *Annual Reports in Computational Chemistry*; Elsevier, 2005; Vol. 1, pp 59–74. https://doi.org/10.1016/S1574-1400(05)01005-4.
(31) Abraham, M.; Alekseenko, A.; Bergh, C.; Blau, C.; Briand, E.; Doijade, M.; Fleischmann, S.; Gapsys, V.; Gaurav Garg; Gorelov, S.; Gouaillardet, G.; Gray, A.; M. Eric Irrgang; Jalalypour, F.; Jordan, J.; Junghans, C.; Prashanth Kanduri; Keller, S.; Kutzner, C.; Lemkul, J. A.; Lundborg, M.; Merz, P.; Miletić, V.; Morozov, D.; Páll, S.; Schulz, R.; Shirts, M.; Shvetsov, A.; Soproni, B.; Van Der Spoel, D.; Turner, P.; Uphoff, C.; Villa, A.; Wingbermühle, S.; Zhmurov, A.; Bauer, P.; Hess, B.; Lindahl, E. GROMACS 2023.1 Manual. **2023**. https://doi.org/10.5281/ZENODO.7852189.

(32) Essmann, U.; Perera, L.; Berkowitz, M. L.; Darden, T.; Lee, H.; Pedersen, L. G. A Smooth Particle Mesh Ewald Method. *J. Chem. Phys.* **1995**, *103* (19), 8577–8593. https://doi.org/10.1063/1.470117.
(33) Bussi, G.; Donadio, D.; Parrinello, M. Canonical Sampling through Velocity Rescaling. *J. Chem. Phys.* **2007**, *126* (1), 014101. https://doi.org/10.1063/1.2408420.
(34) Berendsen, H. J. C.; Postma, J. P. M.; Van Gunsteren, W. F.; DiNola, A.; Haak, J. R. Molecular Dynamics with Coupling to an External Bath. *J. Chem. Phys.* **1984**, *81* (8), 3684–3690. https://doi.org/10.1063/1.448118.
(35) Andersen, H. C. Molecular Dynamics Simulations at Constant Pressure and/or Temperature. *J. Chem. Phys.* **1980**, *72* (4), 2384–2393. https://doi.org/10.1063/1.439486.
(36) Parrinello, M.; Rahman, A. Polymorphic Transitions in Single Crystals: A New Molecular Dynamics Method. *J. Appl. Phys.* **1981**, *52* (12), 7182–7190. https://doi.org/10.1063/1.328693.
(37) Hess, B.; Bekker, H.; Berendsen, H. J. C.; Fraaije, J. G. E. M. LINCS: A Linear Constraint Solver for Molecular Simulations. *J. Comput. Chem.* **1997**, *18* (12), 1463–1472. https://doi.org/10.1002/(SICI)1096-987X(199709)18:12<1463::AID-JCC4>3.0.CO;2-H.
(38) Vijay-kumar, S.; Bugg, C. E.; Cook, W. J. STRUCTURE OF UBIQUITIN REFINED AT 1.8 ANGSTROMS RESOLUTION, 1987.
(39) Kabsch, W.; Sander, C. Dictionary of Protein Secondary Structure: Pattern Recognition of Hydrogen-Bonded and Geometrical Features. *Biopolymers* **1983**, *22* (12), 2577–2637. https://doi.org/10.1002/bip.360221211.
(40) Sneha, P.; George Priya Doss, C. Molecular Dynamics. In *Advances in Protein Chemistry and Structural Biology*; Elsevier, 2016; Vol. 102, pp 181–224. https://doi.org/10.1016/bs.apcsb.2015.09.004.
(41) Baig, M. H.; Sudhakar, D. R.; Kalaiarasan, P.; Subbarao, N.; Wadhawa, G.; Lohani, M.; Khan, M. K. A.; Khan, A. U. Insight into the Effect of Inhibitor Resistant S130G Mutant on Physico-Chemical Properties of SHV Type Beta-Lactamase: A Molecular Dynamics Study. *PLoS ONE* **2014**, *9* (12), e112456. https://doi.org/10.1371/journal.pone.0112456.
(42) Rudin, A.; Choi, P. Practical Aspects of Molecular Weight Measurements. In *The Elements of Polymer Science & Engineering*; Elsevier, 2013; pp 89–148. https://doi.org/10.1016/B978-0-12-382178-2.00003-1.
(43) Gloss, L. M. Equilibrium and Kinetic Approaches for Studying Oligomeric Protein Folding. In *Methods in Enzymology*; Elsevier, 2009; Vol. 466, pp 325–357. https://doi.org/10.1016/S0076-6879(09)66014-6.
(44) Yamamoto, E.; Akimoto, T.; Mitsutake, A.; Metzler, R. Universal Relation between Instantaneous Diffusivity and Radius of Gyration of Proteins in Aqueous Solution. *Phys. Rev. Lett.* **2021**, *126* (12), 128101. https://doi.org/10.1103/PhysRevLett.126.128101.
(45) Eisenhaber, F.; Lijnzaad, P.; Argos, P.; Sander, C.; Scharf, M. The Double Cubic Lattice Method: Efficient Approaches to Numerical Integration of Surface Area and Volume and to Dot Surface Contouring of Molecular Assemblies. *J. Comput. Chem.* **1995**, *16* (3), 273–284. https://doi.org/10.1002/jcc.540160303.
(46) Shrake, A.; Rupley, J. A. Environment and Exposure to Solvent of Protein Atoms. Lysozyme and Insulin. *J. Mol. Biol.* **1973**, *79* (2), 351–371. https://doi.org/10.1016/0022-2836(73)90011-9.
(47) Lee, B.; Richards, F. M. The Interpretation of Protein Structures: Estimation of Static Accessibility. *J. Mol. Biol.* **1971**, *55* (3), 379-IN4. https://doi.org/10.1016/0022-2836(71)90324-X.
(48) Van Der Spoel, D.; Berendsen, H. J. Molecular Dynamics Simulations of Leu-Enkephalin in Water and DMSO. *Biophys. J.* **1997**, *72* (5), 2032–2041. https://doi.org/10.1016/S0006-3495(97)78847-7.

(49) Lipari, G.; Szabo, A. Model-Free Approach to the Interpretation of Nuclear Magnetic Resonance Relaxation in Macromolecules. 1. Theory and Range of Validity. *J. Am. Chem. Soc.* **1982**, *104* (17), 4546–4559. https://doi.org/10.1021/ja00381a009.

(50) Kumari, P.; Shobhna; Kaur, S.; Kashyap, H. K. Influence of Hydration on the Structure of Reline Deep Eutectic Solvent: A Molecular Dynamics Study. *ACS Omega* **2018**, *3* (11), 15246–15255. https://doi.org/10.1021/acsomega.8b02447.

(51) Monteiro, H.; Paiva, A.; Duarte, A. R. C.; Galamba, N. On the Not so Anomalous Water-Induced Structural Transformations of Choline Chloride–Urea (Reline) Deep Eutectic System. *Phys. Chem. Chem. Phys.* **2023**, *25* (1), 439–454. https://doi.org/10.1039/D2CP04139A.

(52) Sapir, L.; Harries, D. Restructuring a Deep Eutectic Solvent by Water: The Nanostructure of Hydrated Choline Chloride/Urea. *J. Chem. Theory Comput.* **2020**, *16* (5), 3335–3342. https://doi.org/10.1021/acs.jctc.0c00120.

(53) Monteiro, H.; Paiva, A.; Duarte, A. R. C.; Galamba, N. Structure and Dynamic Properties of a Glycerol–Betaine Deep Eutectic Solvent: When Does a DES Become an Aqueous Solution? *ACS Sustain. Chem. Eng.* **2022**, *10* (11), 3501–3512. https://doi.org/10.1021/acssuschemeng.1c07461.

(54) Singh, U. C.; Kollman, P. A. An Approach to Computing Electrostatic Charges for Molecules. *J. Comput. Chem.* **1984**, *5* (2), 129–145. https://doi.org/10.1002/jcc.540050204.

(55) Frisch, M. J.; Trucks, G. W.; Cheeseman, J. R.; Scalmani, G.; Caricato, M.; Hratchian, H. P.; Li, X.; Barone, V.; Bloino, J.; Zheng, G.; Vreven, T.; Montgomery, J. A.; Petersson, G. A.; Scuseria, G. E.; Schlegel, H. B.; Nakatsuji, H.; Izmaylov, A. F.; Martin, R. L.; Sonnenberg, J. L.; Peralta, J. E.; Heyd, J. J.; Brothers, E.; Ogliaro, F.; Bearpark, M.; Robb, M. A.; Mennucci, B.; Kudin, K. N.; Staroverov, V. N.; Kobayashi, R.; Normand, J.; Rendell, A.; Gomperts, R.; Zakrzewski, V. G.; Hada, M.; Ehara, M.; Toyota, K.; Fukuda, R.; Hasegawa, J.; Ishida, M.; Nakajima, T.; Honda, Y.; Kitao, O.; Nakai, H. Gaussian 09.

(56) Cornell, W. D.; Cieplak, P.; Bayly, C. I.; Kollman, P. A. Application of RESP Charges to Calculate Conformational Energies, Hydrogen Bond Energies, and Free Energies of Solvation. *J. Am. Chem. Soc.* **1993**, *115* (21), 9620–9631. https://doi.org/10.1021/ja00074a030.

(57) Wang, J.; Wang, W.; Kollman, P. A.; Case, D. A. Automatic Atom Type and Bond Type Perception in Molecular Mechanical Calculations. *J. Mol. Graph. Model.* **2006**.

(58) Van Der Spoel, D.; Lindahl, E.; Hess, B.; Groenhof, G.; Mark, A. E.; Berendsen, H. J. C. GROMACS: Fast, Flexible, and Free. *J. Comput. Chem.* **2005**, *26* (16), 1701–1718. https://doi.org/10.1002/jcc.20291.

(59) Van Gunsteren, W. F.; Berendsen, H. J. C. A Leap-Frog Algorithm for Stochastic Dynamics. *Mol. Simul.* **1988**, *1* (3), 173–185. https://doi.org/10.1080/08927028808080941.

(60) Gonzalez, C. G.; Choi, Y. H.; Verpoorte, R. Preanalytical Treatments: Extraction With Deep Eutectic Solvents. In *Liquid-Phase Extraction*; Elsevier, 2020; pp 565–590. https://doi.org/10.1016/B978-0-12-816911-7.00019-0.

(61) Choi, Y. H.; Van Spronsen, J.; Dai, Y.; Verberne, M.; Hollmann, F.; Arends, I. W. C. E.; Witkamp, G.-J.; Verpoorte, R. Are Natural Deep Eutectic Solvents the Missing Link in Understanding Cellular Metabolism and Physiology? *Plant Physiol.* **2011**, *156* (4), 1701–1705. https://doi.org/10.1104/pp.111.178426.

(62) Verpoorte, R.; Witkamp, G.-J.; Choi, Y. H. Preface: Natural Deep Eutectic Solvents: A Third Liquid Phase in Living Organisms? Discovery, Theory, Biology, and Applications. In *Advances in Botanical Research*; Elsevier, 2021; Vol. 97, pp xv–xxii. https://doi.org/10.1016/S0065-2296(21)00010-0.

(63) Fraige, K.; Arrua, R. D.; Sutton, A. T.; Funari, C. S.; Cavalheiro, A. J.; Hilder, E. F.; Bolzani, V. D. S. Using Natural Deep Eutectic Solvents for the Extraction of Metabolites in *Byrsonima Intermedia* Leaves. *J. Sep. Sci.* **2019**, *42* (2), 591–597. https://doi.org/10.1002/jssc.201800905.

(64) Dai, Y.; Witkamp, G.-J.; Verpoorte, R.; Choi, Y. H. Natural Deep Eutectic Solvents as a New Extraction Media for Phenolic Metabolites in Carthamus Tinctorius L. *Anal. Chem.* **2013**, *85* (13), 6272–6278. https://doi.org/10.1021/ac400432p.

(65) Bajkacz, S.; Adamek, J. Development of a Method Based on Natural Deep Eutectic Solvents for Extraction of Flavonoids from Food Samples. *Food Anal. Methods* **2018**, *11* (5), 1330–1344. https://doi.org/10.1007/s12161-017-1118-5.

(66) Wei, Z.; Qi, X.; Li, T.; Luo, M.; Wang, W.; Zu, Y.; Fu, Y. Application of Natural Deep Eutectic Solvents for Extraction and Determination of Phenolics in Cajanus Cajan Leaves by Ultra Performance Liquid Chromatography. *Sep. Purif. Technol.* **2015**, *149*, 237–244. https://doi.org/10.1016/j.seppur.2015.05.015.

(67) Ghenim, L.; Allier, C.; Obeid, P.; Hervé, L.; Fortin, J.-Y.; Balakirev, M.; Gidrol, X. A New Ultradian Rhythm in Mammalian Cell Dry Mass Observed by Holography. *Sci. Rep.* **2021**, *11* (1), 1290. https://doi.org/10.1038/s41598-020-79661-9.

(68) O'Brien, E. P.; Brooks, B. R.; Thirumalai, D. Effects of pH on Proteins: Predictions for Ensemble and Single-Molecule Pulling Experiments. *J. Am. Chem. Soc.* **2012**, *134* (2), 979–987. https://doi.org/10.1021/ja206557y.

(69) Yancey, P. H.; Clark, M. E.; Hand, S. C.; Bowlus, R. D.; Somero, G. N. Living with Water Stress: Evolution of Osmolyte Systems. *Science* **1982**, *217* (4566), 1214–1222. https://doi.org/10.1126/science.7112124.

(70) Arakawa, T.; Timasheff, S. N. The Stabilization of Proteins by Osmolytes. *Biophys. J.* **1985**, *47* (3), 411–414. https://doi.org/10.1016/S0006-3495(85)83932-1.

(71) Yancey, P. H. Organic Osmolytes as Compatible, Metabolic and Counteracting Cytoprotectants in High Osmolarity and Other Stresses. *J. Exp. Biol.* **2005**, *208* (15), 2819–2830. https://doi.org/10.1242/jeb.01730.

(72) Altinisik, S.; Zeidan, H.; Yilmaz, M. D.; Marti, M. E. Reactive Extraction of Betaine from Sugarbeet Processing Byproducts. *ACS Omega* **2023**, *8* (12), 11029–11038. https://doi.org/10.1021/acsomega.2c07845.

(73) Yang, J.; Cai, N.; Zhai, H.; Zhang, J.; Zhu, Y.; Zhang, L. Natural Zwitterionic Betaine Enables Cells to Survive Ultrarapid Cryopreservation. *Sci. Rep.* **2016**, *6* (1), 37458. https://doi.org/10.1038/srep37458.

(74) Abranches, D. O.; Silva, L. P.; Martins, M. A. R.; Pinho, S. P.; Coutinho, J. A. P. Understanding the Formation of Deep Eutectic Solvents: Betaine as a Universal Hydrogen Bond Acceptor. *ChemSusChem* **2020**, *13* (18), 4916–4921. https://doi.org/10.1002/cssc.202001331.

(75) Wang, S.; Qin, L.; Zhou, Z.; Wang, J. Solubility and Solution Thermodynamics of Betaine in Different Pure Solvents and Binary Mixtures. *J. Chem. Eng. Data* **2012**, *57* (8), 2128–2135. https://doi.org/10.1021/je2011659.

(76) Craig, S. A. Betaine in Human Nutrition. *Am. J. Clin. Nutr.* **2004**, *80* (3), 539–549. https://doi.org/10.1093/ajcn/80.3.539.

(77) Mustafa, S. M.; Barzinjy, A. A.; Hamad, A. H.; Hamad, S. M. Betaine-Based Deep Eutectic Solvents Mediated Synthesis of Zinc Oxide Nanoparticles at Low Temperature. *Ceram. Int.* **2022**, *48* (19), 28951–28960. https://doi.org/10.1016/j.ceramint.2022.04.131.

(78) Govrin, R.; Tcherner, S.; Obstbaum, T.; Sivan, U. Zwitterionic Osmolytes Resurrect Electrostatic Interactions Screened by Salt. *J. Am. Chem. Soc.* **2018**, *140* (43), 14206–14210. https://doi.org/10.1021/jacs.8b07771.

(79) Zhao, G.; He, F.; Wu, C.; Li, P.; Li, N.; Deng, J.; Zhu, G.; Ren, W.; Peng, Y. Betaine in Inflammation: Mechanistic Aspects and Applications. *Front. Immunol.* **2018**, *9*, 1070. https://doi.org/10.3389/fimmu.2018.01070.

(80) Graham, J. E.; Wilkinson, B. J. Staphylococcus Aureus Osmoregulation: Roles for Choline, Glycine Betaine, Proline, and Taurine. *J. Bacteriol.* **1992**, *174* (8), 2711–2716. https://doi.org/10.1128/jb.174.8.2711-2716.1992.
(81) Kidd, M. T.; Ferket, P. R.; Garlich, J. D. Nutritional and Osmoregulatory Functions of Betaine. *Worlds Poult. Sci. J.* **1997**, *53* (2), 125–139. https://doi.org/10.1079/WPS19970013.
(82) Kumar, N.; Kishore, N. Protein Stabilization and Counteraction of Denaturing Effect of Urea by Glycine Betaine. *Biophys. Chem.* **2014**, *189*, 16–24. https://doi.org/10.1016/j.bpc.2014.03.001.
(83) Papageorgiou, G. C.; Murata, N. The Unusually Strong Stabilizing Effects of Glycine Betaine on the Structure and Function of the Oxygen-Evolving Photosystem II Complex. *Photosynth. Res.* **1995**, *44* (3), 243–252. https://doi.org/10.1007/BF00048597.
(84) Knapp, S.; Ladenstein, R.; Galinski, E. A. Extrinsic Protein Stabilization by the Naturally Occurring Osmolytes β-Hydroxyectoine and Betaine. *Extremophiles* **1999**, *3* (3), 191–198. https://doi.org/10.1007/s007920050116.
(85) Gajardo-Parra, N. F.; Meneses, L.; Duarte, A. R. C.; Paiva, A.; Held, C. Assessing the Influence of Betaine-Based Natural Deep Eutectic Systems on Horseradish Peroxidase. *ACS Sustain. Chem. Eng.* **2022**, *10* (38), 12873–12881. https://doi.org/10.1021/acssuschemeng.2c04045.
(86) Jolivet, Y.; Larher, F.; Hamelin, J. Osmoregulation in Halophytic Higher Plants: The Protective Effect of Glycine Betaine against the Heat Destabilization of Membranes. *Plant Sci. Lett.* **1982**, *25* (2), 193–201. https://doi.org/10.1016/0304-4211(82)90177-8.
(87) Garrett, Q.; Khandekar, N.; Shih, S.; Flanagan, J. L.; Simmons, P.; Vehige, J.; Willcox, M. D. P. Betaine Stabilizes Cell Volume and Protects against Apoptosis in Human Corneal Epithelial Cells under Hyperosmotic Stress. *Exp. Eye Res.* **2013**, *108*, 33–41. https://doi.org/10.1016/j.exer.2012.12.001.
(88) Bourot, S.; Sire, O.; Trautwetter, A.; Touzé, T.; Wu, L. F.; Blanco, C.; Bernard, T. Glycine Betaine-Assisted Protein Folding in a lysAMutant of Escherichia Coli. *J. Biol. Chem.* **2000**, *275* (2), 1050–1056. https://doi.org/10.1074/jbc.275.2.1050.
(89) Incharoensakdi, A.; Takabe, T.; Akazawa, T. Effect of Betaine on Enzyme Activity and Subunit Interaction of Ribulose-1,5-Bisphosphate Carboxylase/Oxygenase from *Aphanothece Halophytica*. *Plant Physiol.* **1986**, *81* (4), 1044–1049. https://doi.org/10.1104/pp.81.4.1044.
(90) Di Gioacchino, M.; Bruni, F.; Ricci, M. A. Aqueous Solution of Betaine: Hydration and Aggregation. *J. Mol. Liq.* **2020**, *318*, 114253. https://doi.org/10.1016/j.molliq.2020.114253.
(91) Natalello, A.; Liu, J.; Ami, D.; Doglia, S. M.; De Marco, A. The Osmolyte Betaine Promotes Protein Misfolding and Disruption of Protein Aggregates. *Proteins Struct. Funct. Bioinforma.* **2009**, *75* (2), 509–517. https://doi.org/10.1002/prot.22266.
(92) Christoph, R.; Schmidt, B.; Steinberner, U.; Dilla, W.; Karinen, R. Glycerol. In *Ullmann's Encyclopedia of Industrial Chemistry*; Wiley-VCH Verlag GmbH & Co. KGaA, Ed.; Wiley-VCH Verlag GmbH & Co. KGaA: Weinheim, Germany, 2006; p a12_477.pub2. https://doi.org/10.1002/14356007.a12_477.pub2.
(93) Pagliaro, M.; Ciriminna, R.; Kimura, H.; Rossi, M.; Della Pina, C. From Glycerol to Value-Added Products. *Angew. Chem. Int. Ed.* **2007**, *46* (24), 4434–4440. https://doi.org/10.1002/anie.200604694.
(94) Kayingo, G.; Kilian, S.; Prior, B. Conservation and Release of Osmolytes by Yeasts during Hypo-Osmotic Stress. *Arch. Microbiol.* **2001**, *177* (1), 29–35. https://doi.org/10.1007/s00203-001-0358-2.
(95) Chen, X.; Bhandari, B.; Zhou, P. Insight into the Effect of Glycerol on Stability of Globular Proteins in High Protein Model System. *Food Chem.* **2019**, *278*, 780–785. https://doi.org/10.1016/j.foodchem.2018.11.117.

(96) Vagenende, V.; Yap, M. G. S.; Trout, B. L. Mechanisms of Protein Stabilization and Prevention of Protein Aggregation by Glycerol. *Biochemistry* **2009**, *48* (46), 11084–11096. https://doi.org/10.1021/bi900649t.
(97) Frauenfelder, H.; Fenimore, P. W.; Chen, G.; McMahon, B. H. Protein Folding Is Slaved to Solvent Motions. *Proc. Natl. Acad. Sci.* **2006**, *103* (42), 15469–15472. https://doi.org/10.1073/pnas.0607168103.
(98) Fenimore, P. W.; Frauenfelder, H.; McMahon, B. H.; Parak, F. G. Slaving: Solvent Fluctuations Dominate Protein Dynamics and Functions. *Proc. Natl. Acad. Sci.* **2002**, *99* (25), 16047–16051. https://doi.org/10.1073/pnas.212637899.
(99) Austin, R. H.; Beeson, K. W.; Eisenstein, L.; Frauenfelder, H.; Gunsalus, I. C. Dynamics of Ligand Binding to Myoglobin. *Biochemistry* **1975**, *14* (24), 5355–5373. https://doi.org/10.1021/bi00695a021.
(100) Ansari, A.; Jones, C. M.; Henry, E. R.; Hofrichter, J.; Eaton, W. A. The Role of Solvent Viscosity in the Dynamics of Protein Conformational Changes. *Science* **1992**, *256* (5065), 1796–1798. https://doi.org/10.1126/science.1615323.
(101) Kramers, H. A. Brownian Motion in a Field of Force and the Diffusion Model of Chemical Reactions. *Physica* **1940**, *7* (4), 284–304. https://doi.org/10.1016/S0031-8914(40)90098-2.
(102) Jas, G. S.; Eaton, W. A.; Hofrichter, J. Effect of Viscosity on the Kinetics of α-Helix and β-Hairpin Formation. *J. Phys. Chem. B* **2001**, *105* (1), 261–272. https://doi.org/10.1021/jp0022048.
(103) Sun, H.; Xin, R.; Qu, D.; Yao, F. Mechanism of Deep Eutectic Solvents Enhancing Catalytic Function of Cytochrome P450 Enzymes in Biosynthesis and Organic Synthesis. *J. Biotechnol.* **2020**, *323*, 264–273. https://doi.org/10.1016/j.jbiotec.2020.07.004.
(104) Gorke, J. T.; Srienc, F.; Kazlauskas, R. J. Hydrolase-Catalyzed Biotransformations in Deep Eutectic Solvents. *Chem. Commun.* **2008**, No. 10, 1235. https://doi.org/10.1039/b716317g.
(105) Monhemi, H.; Housaindokht, M. R.; Moosavi-Movahedi, A. A.; Bozorgmehr, M. R. How a Protein Can Remain Stable in a Solvent with High Content of Urea: Insights from Molecular Dynamics Simulation of Candida Antarctica Lipase B in Urea : Choline Chloride Deep Eutectic Solvent. *Phys. Chem. Chem. Phys.* **2014**, *16* (28), 14882. https://doi.org/10.1039/c4cp00503a.
(106) Esquembre, R.; Sanz, J. M.; Wall, J. G.; Del Monte, F.; Mateo, C. R.; Ferrer, M. L. Thermal Unfolding and Refolding of Lysozyme in Deep Eutectic Solvents and Their Aqueous Dilutions. *Phys. Chem. Chem. Phys.* **2013**, *15* (27), 11248. https://doi.org/10.1039/c3cp44299c.
(107) Das, N.; Khan, T.; Subba, N.; Sen, P. Correlating Bromelain's Activity with Its Structure and Active-Site Dynamics and the Medium's Physical Properties in a Hydrated Deep Eutectic Solvent. *Phys. Chem. Chem. Phys.* **2021**, *23* (15), 9337–9346. https://doi.org/10.1039/D1CP00046B.
(108) Pal, S.; Roy, R.; Paul, S. Potential of a Natural Deep Eutectic Solvent, Glyceline, in the Thermal Stability of the Trp-Cage Mini-Protein. *J. Phys. Chem. B* **2020**, *124* (35), 7598–7610. https://doi.org/10.1021/acs.jpcb.0c03501.
(109) Kist, J. A.; Henzl, M. T.; Bañuelos, J. L.; Baker, G. A. Calorimetric Evaluation of the Operational Thermal Stability of Ribonuclease A in Hydrated Deep Eutectic Solvents. *ACS Sustain. Chem. Eng.* **2019**, *7* (15), 12682–12687. https://doi.org/10.1021/acssuschemeng.9b02585.
(110) Sanchez-Fernandez, A.; Prevost, S.; Wahlgren, M. Deep Eutectic Solvents for the Preservation of Concentrated Proteins: The Case of Lysozyme in 1 : 2 Choline Chloride : Glycerol. *Green Chem.* **2022**, *24* (11), 4437–4442. https://doi.org/10.1039/D1GC04378A.
(111) Durand, E.; Lecomte, J.; Baréa, B.; Dubreucq, E.; Lortie, R.; Villeneuve, P. Evaluation of Deep Eutectic Solvent–Water Binary Mixtures for Lipase-Catalyzed Lipophilization of Phenolic Acids. *Green Chem.* **2013**, *15* (8), 2275. https://doi.org/10.1039/c3gc40899j.

(112) Xu, W.-J.; Huang, Y.-K.; Li, F.; Wang, D.-D.; Yin, M.-N.; Wang, M.; Xia, Z.-N. Improving β-Glucosidase Biocatalysis with Deep Eutectic Solvents Based on Choline Chloride. *Biochem. Eng. J.* **2018**, *138*, 37–46. https://doi.org/10.1016/j.bej.2018.07.002.

(113) Sanchez-Fernandez, A.; Basic, M.; Xiang, J.; Prevost, S.; Jackson, A. J.; Dicko, C. Hydration in Deep Eutectic Solvents Induces Non-Monotonic Changes in the Conformation and Stability of Proteins. *J. Am. Chem. Soc.* **2022**, *144* (51), 23657–23667. https://doi.org/10.1021/jacs.2c11190.

(114) Nian, B.; Cao, C.; Liu, Y. How *Candida Antarctica* Lipase B Can Be Activated in Natural Deep Eutectic Solvents: Experimental and Molecular Dynamics Studies. *J. Chem. Technol. Biotechnol.* **2020**, *95* (1), 86–93. https://doi.org/10.1002/jctb.6209.

(115) Khodaverdian, S.; Dabirmanesh, B.; Heydari, A.; Dashtban-moghadam, E.; Khajeh, K.; Ghazi, F. Activity, Stability and Structure of Laccase in Betaine Based Natural Deep Eutectic Solvents. *Int. J. Biol. Macromol.* **2018**, *107*, 2574–2579. https://doi.org/10.1016/j.ijbiomac.2017.10.144.

(116) Daneshjou, S.; Khodaverdian, S.; Dabirmanesh, B.; Rahimi, F.; Daneshjoo, S.; Ghazi, F.; Khajeh, K. Improvement of Chondroitinases ABCI Stability in Natural Deep Eutectic Solvents. *J. Mol. Liq.* **2017**, *227*, 21–25. https://doi.org/10.1016/j.molliq.2016.11.130.

(117) Vijay-kumar, S.; Bugg, C. E.; Cook, W. J. Structure of Ubiquitin Refined at 1.8 Å Resolution. *J. Mol. Biol.* **1987**, *194* (3), 531–544. https://doi.org/10.1016/0022-2836(87)90679-6.

(118) Xie, G.; Timasheff, S. N. The Thermodynamic Mechanism of Protein Stabilization by Trehalose. *Biophys. Chem.* **1997**, *64* (1–3), 25–43. https://doi.org/10.1016/S0301-4622(96)02222-3.

(119) Lee, J. C.; Timasheff, S. N. The Stabilization of Proteins by Sucrose. *J. Biol. Chem.* **1981**, *256* (14), 7193–7201. https://doi.org/10.1016/S0021-9258(19)68947-7.

(120) Weng, L.; Stott, S. L.; Toner, M. Exploring Dynamics and Structure of Biomolecules, Cryoprotectants, and Water Using Molecular Dynamics Simulations: Implications for Biostabilization and Biopreservation. *Annu. Rev. Biomed. Eng.* **2019**, *21* (1), 1–31. https://doi.org/10.1146/annurev-bioeng-060418-052130.

(121) Piana, S.; Lindorff-Larsen, K.; Shaw, D. E. Atomic-Level Description of Ubiquitin Folding. *Proc. Natl. Acad. Sci.* **2013**, *110* (15), 5915–5920. https://doi.org/10.1073/pnas.1218321110.

(122) Wintrode, P. L.; Makhatadze, G. I.; Privalov, P. L. Thermodynamics of Ubiquitin Unfolding. *Proteins Struct. Funct. Genet.* **1994**, *18* (3), 246–253. https://doi.org/10.1002/prot.340180305.

(123) Hezavehei, M.; Sharafi, M.; Kouchesfahani, H. M.; Henkel, R.; Agarwal, A.; Esmaeili, V.; Shahverdi, A. Sperm Cryopreservation: A Review on Current Molecular Cryobiology and Advanced Approaches. *Reprod. Biomed. Online* **2018**, *37* (3), 327–339. https://doi.org/10.1016/j.rbmo.2018.05.012.

(124) Larman, M. G.; Hashimoto, S.; Morimoto, Y.; Gardner, D. K. Cryopreservation in ART and Concerns with Contamination during Cryobanking. *Reprod. Med. Biol.* **2014**, *13* (3), 107–117. https://doi.org/10.1007/s12522-014-0176-2.

(125) Bunge, R. G.; Keettel, W. C.; Sherman, J. K. Report of Four Cases. *Fertil. Steril.* **1954**, *5* (6), 520–529. https://doi.org/10.1016/S0015-0282(16)31802-7.

(126) Pegg, D. E. The History and Principles of Cryopreservation. *Semin. Reprod. Med.* **2002**, *20* (1), 005–014. https://doi.org/10.1055/s-2002-23515.

(127) Arsiccio, A.; Pisano, R. Water Entrapment and Structure Ordering as Protection Mechanisms for Protein Structural Preservation. *J. Chem. Phys.* **2018**, *148* (5), 055102. https://doi.org/10.1063/1.5012884.

(128) Camisasca, G.; De Marzio, M.; Gallo, P. Effect of Trehalose on Protein Cryoprotection: Insights into the Mechanism of Slowing down of Hydration Water. *J. Chem. Phys.* **2020**, *153* (22), 224503. https://doi.org/10.1063/5.0033526.

(129) Sieme, H.; Oldenhof, H.; Wolkers, W. F. Mode of Action of Cryoprotectants for Sperm Preservation. *Anim. Reprod. Sci.* **2016**, *169*, 2–5. https://doi.org/10.1016/j.anireprosci.2016.02.004.
(130) Kar, M.; Chourasiya, Y.; Maheshwari, R.; Tekade, R. K. Current Developments in Excipient Science. In *Basic Fundamentals of Drug Delivery*; Elsevier, 2019; pp 29–83. https://doi.org/10.1016/B978-0-12-817909-3.00002-9.
(131) Chen, S.; Ren, J.; Chen, R. Cryopreservation and Desiccation Preservation of Cells. In *Comprehensive Biotechnology*; Elsevier, 2019; pp 157–166. https://doi.org/10.1016/B978-0-444-64046-8.00451-1.
(132) Swain, J. E.; Smith, G. D. Cryoprotectants. In *Fertility Cryopreservation*; Chian, R.-C., Quinn, P., Eds.; Cambridge University Press, 2010; pp 24–38. https://doi.org/10.1017/CBO9780511730207.005.
(133) Zhang, T.-Y.; Tan, P.-C.; Xie, Y.; Zhang, X.-J.; Zhang, P.-Q.; Gao, Y.-M.; Zhou, S.-B.; Li, Q.-F. The Combination of Trehalose and Glycerol: An Effective and Non-Toxic Recipe for Cryopreservation of Human Adipose-Derived Stem Cells. *Stem Cell Res. Ther.* **2020**, *11* (1), 460. https://doi.org/10.1186/s13287-020-01969-0.
(134) Whaley, D.; Damyar, K.; Witek, R. P.; Mendoza, A.; Alexander, M.; Lakey, J. R. Cryopreservation: An Overview of Principles and Cell-Specific Considerations. *Cell Transplant.* **2021**, *30*, 096368972199961. https://doi.org/10.1177/0963689721999617.
(135) Eroglu, A.; Russo, M. J.; Bieganski, R.; Fowler, A.; Cheley, S.; Bayley, H.; Toner, M. Intracellular Trehalose Improves the Survival of Cryopreserved Mammalian Cells. *Nat. Biotechnol.* **2000**, *18* (2), 163–167. https://doi.org/10.1038/72608.
(136) Jain, N. K.; Roy, I. Effect of Trehalose on Protein Structure. *Protein Sci.* **2008**, NA-NA. https://doi.org/10.1002/pro.3.
(137) Nakamura, T.; Sekiyama, E.; Takaoka, M.; Bentley, A. J.; Yokoi, N.; Fullwood, N. J.; Kinoshita, S. The Use of Trehalose-Treated Freeze-Dried Amniotic Membrane for Ocular Surface Reconstruction. *Biomaterials* **2008**, *29* (27), 3729–3737. https://doi.org/10.1016/j.biomaterials.2008.05.023.
(138) Olsson, C.; Jansson, H.; Swenson, J. The Role of Trehalose for the Stabilization of Proteins. *J. Phys. Chem. B* **2016**, *120* (20), 4723–4731. https://doi.org/10.1021/acs.jpcb.6b02517.
(139) Sui, X.; Wen, C.; Yang, J.; Guo, H.; Zhao, W.; Li, Q.; Zhang, J.; Zhu, Y.; Zhang, L. Betaine Combined with Membrane Stabilizers Enables Solvent-Free Whole Blood Cryopreservation and One-Step Cryoprotectant Removal. *ACS Biomater. Sci. Eng.* **2019**, *5* (2), 1083–1091. https://doi.org/10.1021/acsbiomaterials.8b01286.
(140) Gao, L.; Zhou, Q.; Zhang, Y.; Sun, S.; Lv, L.; Ma, P.; Yang, J.; Liu, M.; Zhang, L.; Wang, X.; Zhan, L. Dimethyl Sulfoxide-Free Cryopreservation of Human Umbilical Cord Mesenchymal Stem Cells Based on Zwitterionic Betaine and Electroporation. *Int. J. Mol. Sci.* **2021**, *22* (14), 7445. https://doi.org/10.3390/ijms22147445.
(141) Mori, N.; Ishihara, M.; Tasaki, H.; Sankai, T.; Otsuki, J. The Effect of Betaine for Mouse Sperm Cryopreservation. *Cryobiology* **2022**, *106*, 157–159. https://doi.org/10.1016/j.cryobiol.2022.03.006.
(142) Balusa, P.; Bommu, S.; Murugesan, S. Effect of Betaine and Raffinose in Cryopreservation Medium on Fertility in Kadaknath Chicken. *Cryoletters* **2022**, *43* (5), 283–288. https://doi.org/10.54680/fr22510110212.
(143) De Los Reyes, M.; Saenz, L.; Lapierre, L.; Crosby, J.; Barros, C. Evaluation of Glucose as a Cryoprotectant for Boar Semen. *Vet. Rec.* **2002**, *151* (16), 477–480. https://doi.org/10.1136/vr.151.16.477.

(144) Herdis; Surachman, M.; Darmawan, I. W. A.; Afifah. The Role of Sucrose as Extracellular Cryoprotectant in Maintaining the Garut Rams' Frozen Semen Quality; Malang, Indonesia, 2019; p 080019. https://doi.org/10.1063/1.5115757.
(145) Raju, R.; Bryant, S. J.; Wilkinson, B. L.; Bryant, G. The Need for Novel Cryoprotectants and Cryopreservation Protocols: Insights into the Importance of Biophysical Investigation and Cell Permeability. *Biochim. Biophys. Acta BBA - Gen. Subj.* **2021**, *1865* (1), 129749. https://doi.org/10.1016/j.bbagen.2020.129749.
(146) Bosch, E.; De Vos, M.; Humaidan, P. The Future of Cryopreservation in Assisted Reproductive Technologies. *Front. Endocrinol.* **2020**, *11*, 67. https://doi.org/10.3389/fendo.2020.00067.
(147) Testart, J.; Volante, M.; Lassalle, B.; Gazengel, A.; Belaisch-Allart, J.; Hazout, A.; De Ziegler, D.; Frydman, R. Comparison of Cryoprotectants and Stages of Human Embryo. In *Advances in Assisted Reproductive Technologies*; Mashiach, S., Ben-Rafael, Z., Laufer, N., Schenker, J. G., Eds.; Springer US: Boston, MA, 1990; pp 573–587. https://doi.org/10.1007/978-1-4613-0645-0_62.
(148) Hungerford, A.; Bakos, H. W.; Aitken, R. J. Sperm Cryopreservation: Current Status and Future Developments. *Reprod. Fertil. Dev.* **2022**, *35* (3), 265–281. https://doi.org/10.1071/RD22219.
(149) Sciorio, R.; Manna, C.; Fauque, P.; Rinaudo, P. Can Cryopreservation in Assisted Reproductive Technology (ART) Induce Epigenetic Changes to Gametes and Embryos? *J. Clin. Med.* **2023**, *12* (13), 4444. https://doi.org/10.3390/jcm12134444.
(150) Reyes Palomares, A.; Rodriguez-Wallberg, K. A. Update on the Epigenomic Implication of Embryo Cryopreservation Methods Applied in Assisted Reproductive Technologies With Potential Long-Term Health Effects. *Front. Cell Dev. Biol.* **2022**, *10*, 881550. https://doi.org/10.3389/fcell.2022.881550.
(151) Chen, H.; Zhang, L.; Meng, L.; Liang, L.; Zhang, C. Advantages of Vitrification Preservation in Assisted Reproduction and Potential Influences on Imprinted Genes. *Clin. Epigenetics* **2022**, *14* (1), 141. https://doi.org/10.1186/s13148-022-01355-y.
(152) Faria, A. D.; Luz, P. B. D.; Sobrino, S. D. P.; Medeiros, C. M. D.; Tavares, A. R.; Soares, F. S. Efficacy of Passion Fruit Cryopreservation Using Cryopotectant Agents. *Int. J. Fruit Sci.* **2020**, *20* (sup2), S627–S635. https://doi.org/10.1080/15538362.2020.1753139.
(153) Popova, E.; Kulichenko, I.; Kim, H.-H. Critical Role of Regrowth Conditions in Post-Cryopreservation of In Vitro Plant Germplasm. *Biology* **2023**, *12* (4), 542. https://doi.org/10.3390/biology12040542.
(154) Xie, J.; Ekpo, M. D.; Xiao, J.; Zhao, H.; Bai, X.; Liang, Y.; Zhao, G.; Liu, D.; Tan, S. Principles and Protocols For Post-Cryopreservation Quality Evaluation of Stem Cells in Novel Biomedicine. *Front. Pharmacol.* **2022**, *13*, 907943. https://doi.org/10.3389/fphar.2022.907943.
(155) Hornberger, K.; Yu, G.; McKenna, D.; Hubel, A. Cryopreservation of Hematopoietic Stem Cells: Emerging Assays, Cryoprotectant Agents, and Technology to Improve Outcomes. *Transfus. Med. Hemotherapy* **2019**, *46* (3), 188–196. https://doi.org/10.1159/000496068.
(156) Yuan, Y.; Yang, Y.; Tian, Y.; Park, J.; Dai, A.; Roberts, R. M.; Liu, Y.; Han, X. Efficient Long-Term Cryopreservation of Pluripotent Stem Cells at −80 °C. *Sci. Rep.* **2016**, *6* (1), 34476. https://doi.org/10.1038/srep34476.
(157) Berz, D.; McCormack, E. M.; Winer, E. S.; Colvin, G. A.; Quesenberry, P. J. Cryopreservation of Hematopoietic Stem Cells. *Am. J. Hematol.* **2007**, *82* (6), 463–472. https://doi.org/10.1002/ajh.20707.
(158) Erol, O. D.; Pervin, B.; Seker, M. E.; Aerts-Kaya, F. Effects of Storage Media, Supplements and Cryopreservation Methods on Quality of Stem Cells. *World J. Stem Cells* **2021**, *13* (9), 1197–1214. https://doi.org/10.4252/wjsc.v13.i9.1197.

(159) Capicciotti, C. J.; Mancini, R. S.; Turner, T. R.; Koyama, T.; Alteen, M. G.; Doshi, M.; Inada, T.; Acker, J. P.; Ben, R. N. *O* -Aryl-Glycoside Ice Recrystallization Inhibitors as Novel Cryoprotectants: A Structure–Function Study. *ACS Omega* **2016**, *1* (4), 656–662. https://doi.org/10.1021/acsomega.6b00163.

(160) Chaudhari, C. Frozen Red Blood Cells in Transfusion. *Med. J. Armed Forces India* **2009**, *65* (1), 55–58. https://doi.org/10.1016/S0377-1237(09)80057-9.

(161) Lewis, J. K.; Bischof, J. C.; Braslavsky, I.; Brockbank, K. G. M.; Fahy, G. M.; Fuller, B. J.; Rabin, Y.; Tocchio, A.; Woods, E. J.; Wowk, B. G.; Acker, J. P.; Giwa, S. The Grand Challenges of Organ Banking: Proceedings from the First Global Summit on Complex Tissue Cryopreservation. *Cryobiology* **2016**, *72* (2), 169–182. https://doi.org/10.1016/j.cryobiol.2015.12.001.

(162) Manuchehrabadi, N.; Gao, Z.; Zhang, J.; Ring, H. L.; Shao, Q.; Liu, F.; McDermott, M.; Fok, A.; Rabin, Y.; Brockbank, K. G. M.; Garwood, M.; Haynes, C. L.; Bischof, J. C. Improved Tissue Cryopreservation Using Inductive Heating of Magnetic Nanoparticles. *Sci. Transl. Med.* **2017**, *9* (379), eaah4586. https://doi.org/10.1126/scitranslmed.aah4586.

(163) Wang, G.; Yu, X.; Lu, Z.; Yang, Y.; Xia, Y.; Lai, P. F.-H.; Ai, L. Optimal Combination of Multiple Cryoprotectants and Freezing-Thawing Conditions for High Lactobacilli Survival Rate during Freezing and Frozen Storage. *LWT* **2019**, *99*, 217–223. https://doi.org/10.1016/j.lwt.2018.09.065.

(164) Da Silva, A. M.; Bezerra, L. G. P.; Praxedes, E. C. G.; Moreira, S. S. J.; De Souza, C. M. P.; De Oliveira, M. F.; Pereira, A. F.; Comizzoli, P.; Silva, A. R. Combination of Intracellular Cryoprotectants Preserves the Structure and the Cells Proliferative Capacity Potential of Adult Collared Peccary Testicular Tissue Subjected to Solid Surface Vitrification. *Cryobiology* **2019**, *91*, 53–60. https://doi.org/10.1016/j.cryobiol.2019.10.199.

(165) Kresna, A.; Widjiati, W.; Damayanti, T. Cryoprotectant Combination Ethylene Glycol and Propanediol on Mice Blastocyst Viability Post Vitrification. *J. Phys. Conf. Ser.* **2019**, *1146*, 012028. https://doi.org/10.1088/1742-6596/1146/1/012028.

(166) Finkle, B. J.; Ulrich, J. M. Effects of Cryoprotectants in Combination on the Survival of Frozen Sugarcane Cells. *Plant Physiol.* **1979**, *63* (4), 598–604.

(167) Castro, V. I. B.; Craveiro, R.; Silva, J. M.; Reis, R. L.; Paiva, A.; C. Duarte, A. R. Natural Deep Eutectic Systems as Alternative Nontoxic Cryoprotective Agents. *Cryobiology* **2018**, *83*, 15–26. https://doi.org/10.1016/j.cryobiol.2018.06.010.

(168) Tian, Y.; Sun, D.-W.; Xu, L.; Fan, T.-H.; Zhang, S.-T.; Zhu, Z. Bioinspired Cryoprotectants Enabled by Binary Natural Deep Eutectic Solvents for Sustainable and Green Cryopreservation. *ACS Sustain. Chem. Eng.* **2022**, *10* (23), 7677–7691. https://doi.org/10.1021/acssuschemeng.2c01578.

(169) Hornberger, K.; Li, R.; Duarte, A. R. C.; Hubel, A. Natural Deep Eutectic Systems for NATURE-INSPIRED Cryopreservation of Cells. *AIChE J.* **2021**, *67* (2). https://doi.org/10.1002/aic.17085.

(170) Qiao, Y.; Cai, H.-L.; Yang, X.; Zang, Y.-Y.; Chen, Z.-G. Effects of Natural Deep Eutectic Solvents on Lactic Acid Bacteria Viability during Cryopreservation. *Appl. Microbiol. Biotechnol.* **2018**, *102* (13), 5695–5705. https://doi.org/10.1007/s00253-018-8996-3.

(171) Craveiro, R.; Castro, V. I. B.; Viciosa, M. T.; Dionísio, M.; Reis, R. L.; Duarte, A. R. C.; Paiva, A. Influence of Natural Deep Eutectic Systems in Water Thermal Behavior and Their Applications in Cryopreservation. *J. Mol. Liq.* **2021**, *329*, 115533. https://doi.org/10.1016/j.molliq.2021.115533.

(172) Saadat Maryan, H.; Ghasemian, F.; Bahadori, M. H. Effects of Cryopreservation in the Presence of Natural Deep Eutectic Solvents (NADESs) on Sperm Parameters. *Cryobiology* **2023**, *112*, 104550. https://doi.org/10.1016/j.cryobiol.2023.05.007.

(173) Boukamp, P.; Petrussevska, R. T.; Breitkreutz, D.; Hornung, J.; Markham, A.; Fusenig, N. E. Normal Keratinization in a Spontaneously Immortalized Aneuploid Human Keratinocyte Cell Line. *J. Cell Biol.* **1988**, *106* (3), 761–771. https://doi.org/10.1083/jcb.106.3.761.

(174) Ali, S. H.; DeCaprio, J. A. Cellular Transformation by SV40 Large T Antigen: Interaction with Host Proteins. *Semin. Cancer Biol.* **2001**, *11* (1), 15–23. https://doi.org/10.1006/scbi.2000.0342.

(175) Schoop, V. M.; Fusenig, N. E.; Mirancea, N. Epidermal Organization and Differentiation of HaCaT Keratinocytes in Organotypic Coculture with Human Dermal Fibroblasts. *J. Invest. Dermatol.* **1999**, *112* (3), 343–353. https://doi.org/10.1046/j.1523-1747.1999.00524.x.

(176) Warskulat, U.; Reinen, A.; Grether-Beck, S.; Krutmann, J.; Häussinger, D. The Osmolyte Strategy of Normal Human Keratinocytes in Maintaining Cell Homeostasis. *J. Invest. Dermatol.* **2004**, *123* (3), 516–521. https://doi.org/10.1111/j.0022-202X.2004.23313.x.

(177) Warskulat, U.; Brookmann, S.; Reinen, A.; Häussinger, D. Ultraviolet B Radiation Induces Cell Shrinkage and Increases Osmolyte Transporter mRNA Expression and Osmolyte Uptake in HaCaT Keratinocytes. *bchm* **2007**, *388* (12), 1345–1352. https://doi.org/10.1515/BC.2007.140.

(178) Bryant, S. J.; Awad, M. N.; Elbourne, A.; Christofferson, A. J.; Martin, A. V.; Meftahi, N.; Drummond, C. J.; Greaves, T. L.; Bryant, G. Deep Eutectic Solvents as Cryoprotective Agents for Mammalian Cells. *J. Mater. Chem. B* **2022**, *10* (24), 4546–4560. https://doi.org/10.1039/D2TB00573E.

(179) Bachman, J. Preparation of Slides for Microscopy from Frozen Tissue Sections. In *Methods in Enzymology*; Elsevier, 2013; Vol. 533, pp 217–224. https://doi.org/10.1016/B978-0-12-420067-8.00014-3.

(180) Hossain, A. M.; Osuamkpe, C. O. Sole Use of Sucrose in Human Sperm Cryopreservation. *Arch. Androl.* **2007**, *53* (2), 99–103. https://doi.org/10.1080/01485010701225675.

(181) Oluwatosin, S. O.; Tai, S. L.; Fagan-Endres, M. A. Sucrose, Maltodextrin and Inulin Efficacy as Cryoprotectant, Preservative and Prebiotic – towards a Freeze Dried Lactobacillus Plantarum Topical Probiotic. *Biotechnol. Rep.* **2022**, *33*, e00696. https://doi.org/10.1016/j.btre.2021.e00696.

(182) Lee, K.; Moon, D.; Kang, S. Trehalose Improves Cell Proliferation and Dehydration Tolerance of Human HaCaT Cells. *Arch. Biol. Sci.* **2015**, *67* (3), 849–860. https://doi.org/10.2298/ABS140221044L.

APPENDIX A

Table A.1. Variation of the density (ρ) and viscosity (η) in Betaine:Glycerol (1:2) with charge scaling (λQ) alongside experimental data.

Exp./MD λ_Q	ρ (g·cm^{-3})	η (mPa·s)
Experimental	1.216	1528
1.0	1.316	> 40000
0.975	1.309	-
0.95	1.303	-
0.925	1.296	-
0.92[a]	1.295	2731 ± 151
0.9	1.290	1756±40
0.85	1.273	284±12
0.8	1.257	70±3

[a] λ_Q chosen to scan λ_σ

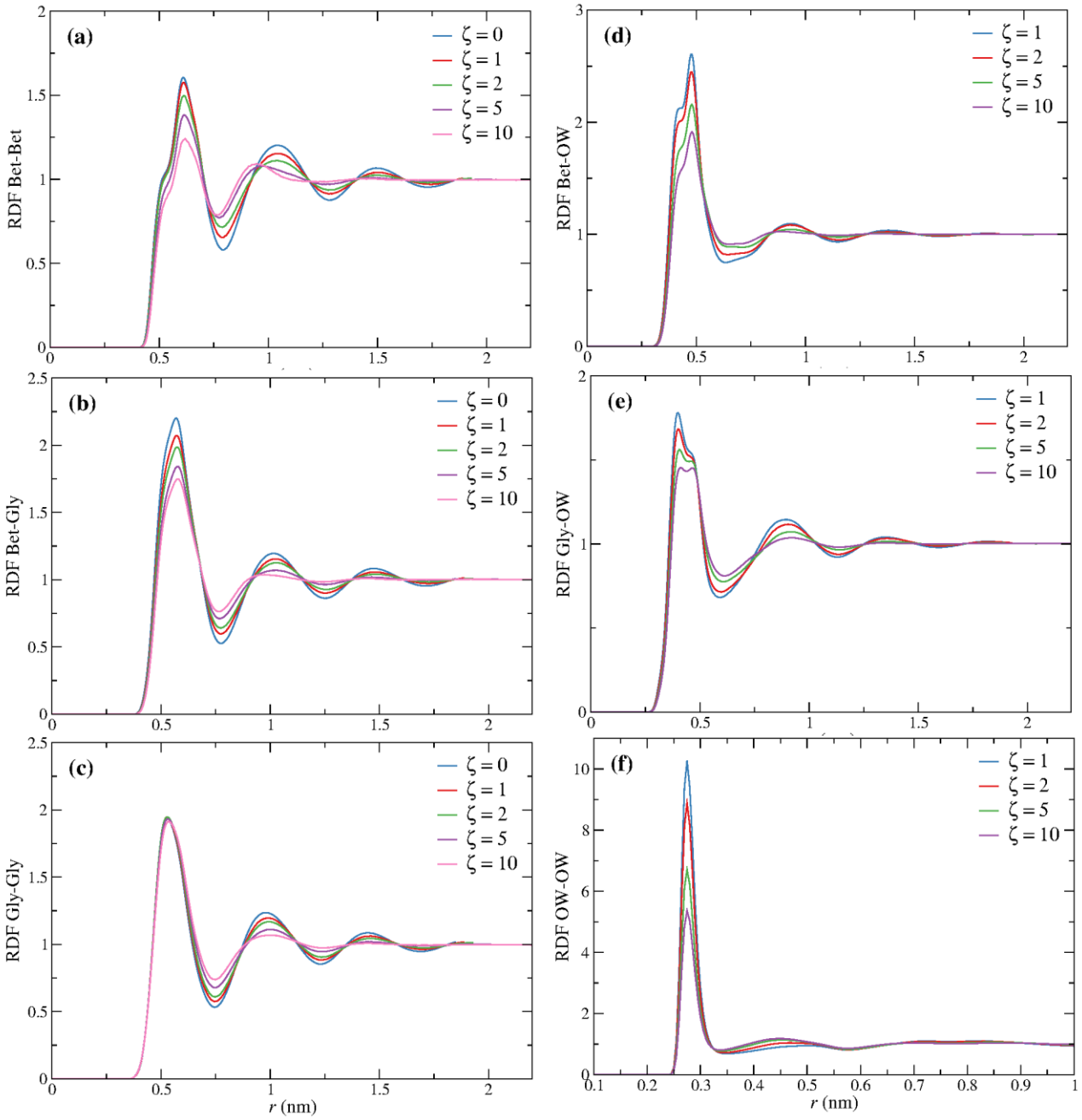

Figure A.1. Panels (a) through (f) display RDFs for Betaine-Betaine, Betaine-Glycerol, Glycerol-Glycerol, Betaine-water (OW), Glycerol-water (OW), and water-water (OW-OW), respectively.

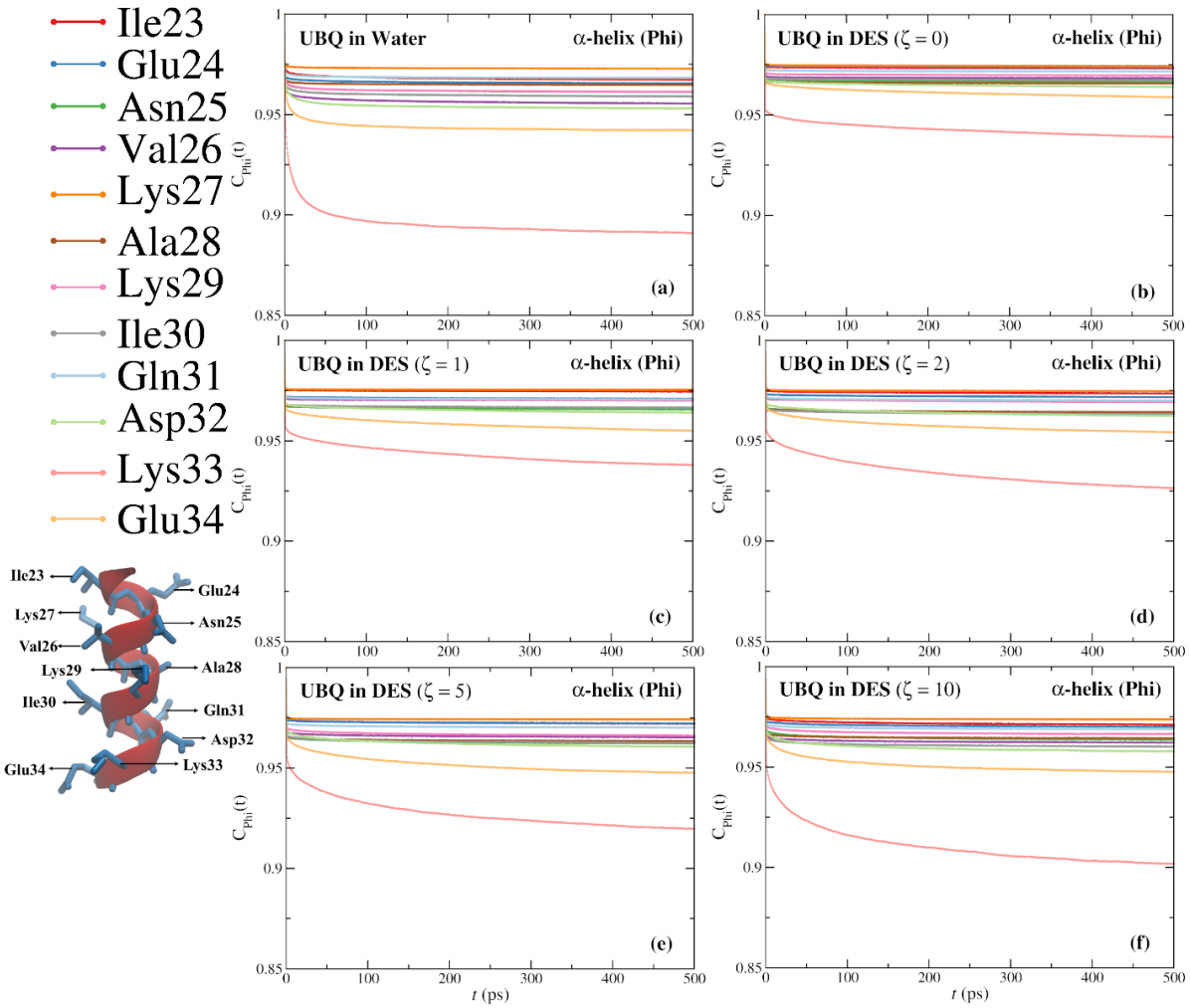

Figure A.2. Torsional dynamics of UBQ α-helix in water and (Bet:Gly:Wat). *Torsional dynamics time correlation functions for the phi angles of the α-helix (amino acids 23-34) in UBQ in pure water and UBQ in (Bet:Gly) with varying water contents. The simulations were conducted at 298 K and 0.1 MPa.*